Uncovering the role of biomineralisation in otolith trace element uptake by microstructural and microchemical analysis

Thesis submitted in fulfilment of Masters of Philosophy (Chemistry)

Aoife McFadden

Department of Chemistry,

School of Physical Sciences

The University of Adelaide

November 2016

Table of Contents

List of Abbreviations

SEM	Scanning Electron Microscopy
LA-ICP-MS	Laser Ablation Inductively Coupled Plasma Mass Spectrometry
EPMA	Electron Probe Microanalysis
EBSD	Electron Backscatter Diffraction
XRD	X-Ray Diffraction
BSE	Backscatter Electrons
SE	Secondary Electrons
WDS	Wavelength Dispersive Spectrometer
PET	Pentaerythritol spectrometer crystal
TAP	Thallium Acid Phthalate spectrometer crystal
LPET	Large Pentaerythritol spectrometer crystal
LTAP	Large Thallium Acid Phthalate spectrometer crystal
CCD	Charge-coupled Device

Abstract

Otolith biomineralisation was examined in order to uncover its role in trace element uptake within otolith structures by microstructural and chemical analysis. The mechanism of otolith elemental incorporation, the orientation of aragonite and the organic matrix in otoliths of four marine species were investigated in conjunction with the otolith growth patterns and the distribution of trace and minor elemental composition. Results for otoliths of *Platycephalus bassensis, Chrysophrys auratus, Trachurus novaezelandiae and Lates calcarifer* suggest a common biomineralisation mechanism for marine species, with consistent results across all species.

The aragonite orientation, as mapped by electron backscatter diffraction (EBSD), revealed the aragonite c-axis was preferentially aligned parallel with the otolith growth axis and perpendicular to the insoluble organic matrices orientation, as determined by Raman microspectroscopy, in the otoliths of *Platycephalus bassensis, Chrysophrys auratus, Trachurus novaezelandiae and Lates calcarifer.* The orientation results indicate that otolith mineral growth is directed and controlled by the organic matrix, which acts as a template for the mineral growth, constraining the aragonite orientation and alignment. The organic rich zones (D-zone bands) within the otolith were composed of both insoluble and soluble organic matrices in all four species, with the insoluble matrices bridging the gap between mineral rich zones (L- zone bands) so as to retain crystal orientation across the otolith.

Optimisation of electron probe microanalysis (EPMA) quantitative mapping achieved both high spatial resolution (<3 μm) and two dimensional visualisation of the fine scale Sr and S distributions in the otoliths with minimal otolith damage. The otolith growth patterns showed a clear association with the distribution of Sr and S, with D-zone bands exhibiting elevated concentrations of both elements as compared to the L-zone bands. Further examination by laser ablation inductively coupled plasma mass spectrometry (LA-ICP-MS) showed that incorporation of Mg and Ba appears independent of both the S distribution and the growth patterns in all four species. The results suggest that element incorporation into the otolith is linked to the organic composition in the

endolymph during mineralisation, and the organic matrices may in part assist the uptake of Sr.

The study revealed that whilst the otolith biomineralisation is directed and templated, with aragonite orientation constrained by the insoluble organic matrices, this process has no direct influence over trace element uptake. The association between the distribution of Sr, S and the organic matrices within the otoliths suggests however that the soluble organic matrices may play a role in trace element incorporation, particularly Sr incorporation. These findings may therefore have significant implications for the interpretation of otolith Sr chemistry.

Declaration

I certify that this work contains no material which has been accepted for the award of any other degree or diploma in my name in any university or other tertiary institution and, to the best of my knowledge and belief contains no material previously published or written by another person, except where due reference has been made in the text. In addition I certify that no part of this work will, in the future, be used in a submission in my name for any other degree or diploma in any university or tertiary institution without the prior approval of the University of Adelaide and where applicable, any partner institution responsible for the joint award of this degree.

I give consent to this copy of my thesis when deposited in the University Library, being made available for loan and photocopying, subject to the Copyright Act 1968.

The author acknowledges that copyright of published works contained within this thesis resides with the copyright holder(s) of those works.

I acknowledge the support I have received for my research through the provision of an Australian Government Research Training Program Scholarship.

I also give permission for the digital version of my thesis to be made available on the web, via the University's digital research repository, the Library Search and also through web search engines, unless permission has been granted by the University to restrict access for a period of time.

Acknowledgments

I would like to acknowledge everyone who has had a hand in helping me to complete this thesis.

Firstly thanks to my supervisors, Allan Pring, Bronwyn Gillanders and Claire Lenehan for taking me on as a student and helping me along the way. I've much appreciated all your efforts and input. And a particular thank you to Hugh Harris for agreeing to supervise me.

Thanks to all the staff at Adelaide Microscopy for your willingness to assist in everything from sample prep to method development and for being so understanding of my spending time hiding away while writing. Thanks especially to Ben Wade for his assistance in developing methods and to Lyn Waterhouse for her efforts in helping with sample preparation. Your efforts were greatly appreciated. A special thanks also goes to John Terlet for his enthusiasm in letting me take on study part time while working.

For all the assistance and support with everything and anything I asked, thanks to Chris Izzo for making this whole undertaking so much easier.

There are also a number of people who I need to say thank you to, because they listened to all my complaints and worries during this process and reassured me the whole way through. Thanks first to Ben Thorpe for always being cool, calm and collected and passing that onto me when I need it most. Lastly, thanks to my family who are always so supportive of everything I do.

Chapter 1

Introduction to otolith biomineralisation and trace element uptake

Biomineralisation

Biomineralisation refers to the process by which organisms form minerals for their own functional requirements (Lowenstam and Weiner 1989). Organisms from many different phyla evolved the ability to form biominerals some 540Myr ago, with at least 60 unique minerals known to be formed biologically today (Dove *et al.* 1996; Lowenstam and Weiner 1989). Biominerals are immensely diverse in type and function, and often exhibit properties such as size, shape, crystallinity and composition which differ significantly from their abiotic counterparts. Biomineralisation differs from inorganic mineralisation as it encompasses both organic and inorganic contributions, often in a strictly controlled manner. The resultant biominerals have been refined over the course of evolution to perform specific functions including internal support and mobility (endoskeletons), protection (exoskeletons), cutting and grinding (teeth), sight, orientation (magnetic receptors) and balance (otoliths and otoconia) (Lowenstam and Weiner 1989). The remarkable properties of biominerals achieved by uniting the flexibility and fracture resistance of organic materials with the hardness of inorganic minerals are of interest in their own right and have provided inspiration for the design of many advanced materials (Weiner and Addadi 1997).

Biomineralisation can be largely understood from physical principles as biominerals are derived from an initial solution and are either completely crystalline or include crystalline components (Lowenstam and Weiner 1989; Weiner and Addadi 1997). As with inorganic systems, crystallisation of a biomineral is a phase transition through which matter is transferred from a state of high free energy in solution to a state of low free energy in a crystal lattice. The energy of transformation determines the resulting phase, texture, orientation and growth rate of a crystal. De Yoreo and Vekilov (2003) postulate that organisms can orchestrate highly specific crystal growth by manipulation of the energy barrier, which in turn controls growth kinetics and the final phase formed

(De Yoreo and Vekilov 2003). The ways in which organisms achieve such control is varied between both species and biominerals, though can be understood from the principles of crystal nucleation and growth (Lowenstam and Weiner 1989; Weiner and Addadi 1997).

Otolith Biomineralisation

An otolith is a calcified structure found in the inner ear of teleost fish, which enables the perception of gravity and sound. The three pairs of otolith bones, the sagittae, asteriscus and lapillus are composed of $CaCO_3$ which also incorporates an organic matrix. Otolith growth is continuous, and it advances incrementally, following a circadian rhythm which falls under both physiological and environmental regulation (Carlstrom 1963; Degens *et al.* 1969; Pannella 1971). The otolith is understood to be an inert structure which permanently incorporates trace elements from the environment, without reabsorption or remodelling of the bone. Consequently the otolith microstructure and otolith chemistry are used as a biological archive, allowing for the identification of stock, age validations, reconstruction of migration pathways and elucidation of environmental histories (Campana 1999). Whilst some applications are well established and validated, the reconstruction of migration pathways and environmental histories requires a deeper understanding of the otolith chemistry, genetic influences and the environmental conditions. Understanding the response of otolith chemistry to environmental changes and the effect of genetic differences is beginning to be addressed (Barnes and Gillanders 2013; Reis-Santos *et al.* 2013), however it is also crucial to understand the physiological regulation of trace elements as a result of the biomineralisation process.

Otolith biomineralisation is acellular and takes place within a medium, the endolymph, containing all the precursors necessary for otolith formation (Payan *et al.* 2002). Precipitation of calcium carbonate in the otolith can be explained by the endolymph conditions, including pH, composition and temperature (Campana 1999; Falini *et al.* 2005), however the regulation of otolith size, shape, polymorph selection and the correct anchoring of the otolith to the sensory epithelium are under control of an organic matrix (Falini *et al.* 2005; Murayama *et al.* 2005; Sollner *et al.* 2003).

Inorganically, calcium carbonate can precipitate as calcite, aragonite or vaterite but the predominant polymorph formed by the sagittal and lapilli otoliths is aragonite, whilst most asteriscii otoliths form as vaterite (Campana 1999; Carlstrom 1963). Selective formation of specific calcium carbonate polymorphs is a common trait in biomineralisation and has been demonstrated to be controlled by the organic matrix in a variety of cases (Addadi *et al.* 1987; Falini *et al.* 1996; Falini *et al.* 2005; Weiner and Addadi 1991).

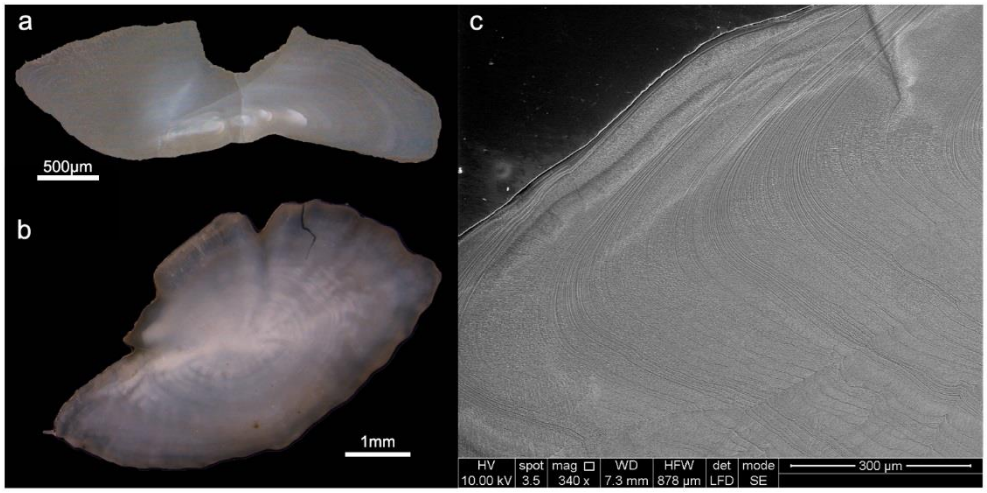

Figure 1: Otolith images a) optical image of otolith cross section, b) optical image of whole otolith and c) SEM secondary electron image of otolith cross section showing the growth bands.

The highly controlled growth of biominerals is regulated by organic macromolecules, but organic components also exhibit control over nucleation (Weiner and Dove 2003). The growth of biominerals in precise locations within an organism and the formation of specific shapes and crystallographic orientations point towards active control of nucleation. Organic compounds serve as a template for growth, providing preferential sites for nucleation and controlling the orientation of the resulting crystals (De Yoreo and Vekilov 2003). X-ray and electron diffraction studies of mollusc shells reveal that collagen-like proteins form a structural framework which is aligned with the mineral crystallographic axes, indicating that crystal growth occurs upon, and is constrained by, an organic matrix framework (Weiner *et al.* 1983; Weiner and Traub 1980). In the organic matrices of otoliths, a variety of proteins, collagens, amino acids, proteoglycans

and organic macromolecules have been detected but the specific role of each in the biomineralisation process remains unclear (Borelli *et al.* 2003; Borelli *et al.* 2001; Tohse *et al.* 2008).

Calcium Carbonate

Aragonite is a naturally occurring form of calcium carbonate exhibiting orthorhombic crystal symmetry. Under standard temperatures and pressures aragonite is thermodynamically unstable and will eventually alter to calcite (Wray and Daniels 1957). Aragonite can precipitate in a variety of crystal textures, which form both naturally and biologically. The aragonite structure consists of paired, superimposed triangular CO_3 groups, which are rotated by 60°, lie in the (001) plane and are linked by 9 cations, giving aragonite 9-fold coordination (Figure 2) (Strunz and Nickel 2001). Studies of otolith aragonite show a predominance of the acicular and prismatic habits, with twinning present in the grains (Gauldie and Nelson 1988; Parmentier *et al.* 2007; Zhuo *et al.* 2009). Vaterite is a less common polymorph of calcium carbonate; it has hexagonal crystal symmetry and being the least stable of the calcium carbonates, is formed predominantly as a biomineral. The vaterite structure is made up of layers of close packed CO_3 groups alternating with layers of 8 coordinate Ca atoms, where the CO_3 planes are perpendicular to (0001). The crystal textures of vaterite present in the asteriscii otolith are not well characterised for many species (Ren *et al.* 2011). For comparison, the calcite polymorph has sheets of planar CO_3 groups and sheets of corner sharing Ca octahedral which alternate along [0001]. Each oxygen of the CO_3 group connects a Ca atom of the underlying sheet to a Ca atom of the overlying sheet forming a 3D framework (Strunz and Nickel 2001).

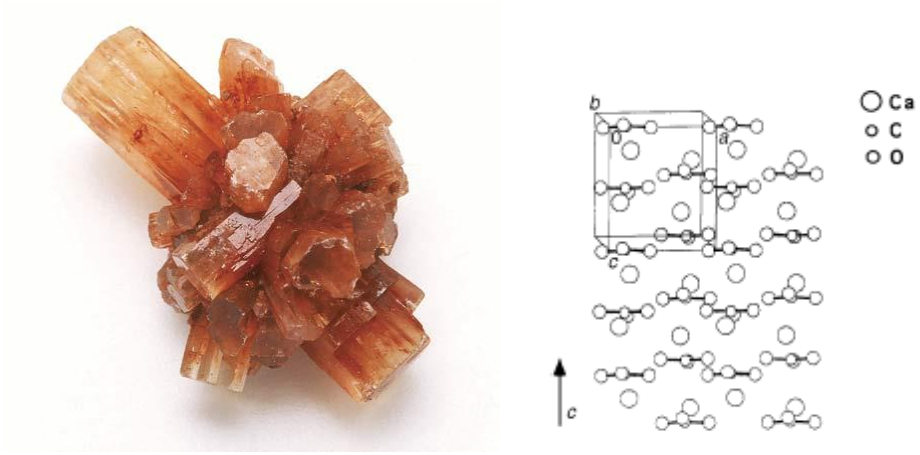

Figure 2: a) Mineral aragonite (Britannnica 2016) and b) aragonite crystal structure, tilted out of plane on the c-axes by 5° to improve perspective (Weiner and Addadi 1997).

Otolith Trace Element Chemistry

Both inorganic and biological calcium carbonates are known to incorporate impurities in levels which are dependent on the polymorph. Otolith composition is often broadly cited as containing less than 1 wt% of inorganic minor and trace elements, though this value is derived from aragonitic otoliths (Campana 1997; Campana 1999). The uptake of minor and trace elements in aragonitic otoliths differs from that of vateritic otoliths. Irregular sagittae and lapilli are known to be formed on occasion, with discrete sections of vaterite in the predominantly aragonitic otoliths. There is no accepted explanation for the formation of vateritic regions, though a heightened incidence in farmed fish otoliths has led to the supposition of stress induced changes to the expression of the organic macromolecules regulating polymorph selection (Kalish 1992). Studies of aberrant otoliths have found a significant difference in trace element concentrations in vateritic regions as compared to the aragonitic regions (Brown and Severin 1999; Melancon *et al.* 2005). Small cations such as Mg and Mn were present in elevated levels in vateritic regions, whereas larger cations such as Sr and Ba were depleted (Melancon *et al.* 2005). Melancon et al. (2005) postulated that the hexagonal crystal structure of vaterite reduces its ability to incorporate larger cations, with an average metal-carbonate bond length of 2.46 Å compared to 2.53 Å for aragonite (Hasse *et al.* 2000).

Whilst the influence of crystal phase on trace element incorporation is well established, the effect of crystal texture remains unknown in otoliths. Inorganic systems reveal that solution chemistry has a major influence on crystal texture of calcite (Kavanagh *et al.* 1990) and recent studies of the shells of the bivalve *Arctica Islandica* revealed an association between the Sr/Ca, Ba/Ca and Mg/Ca ratios and crystal fabric. In particular, the heterogenous variation of Sr in the aragonitic shells did not reflect environmental changes but rather showed an association to the crystal size and shape (Foster *et al.* 2009; Schöne *et al.* 2013). The existence of such a relationship in otoliths has not been evaluated for any species, despite the common use of Sr as an environmental proxy.

The precise occlusion of trace elements within the otolith structure is not well studied but is expected to be analogous to that observed for inorganic aragonite. The binding of trace elements is predicted to occur by one of four possible mechanisms; 1) as a random substitution for Ca within the crystal lattice; 2) as a non-random substitution for Ca within the lattice; 3) within the interstitial sites of the crystal lattice; or 4) in association with the organic matrix (Campana 1999). To date, EXAFS studies of otolith trace elements have determined only the preferential binding of Sr, which is shown to occur as a random substitution for Ca within the lattice (Doubleday *et al.* 2014). Applications of otolith chemistry rely on the permanent incorporation of trace elements within the crystal lattice, meaning it is important to understand the mode of bonding for the trace elements.

Inorganic systems reveal that trace element uptake within a crystal occurs preferentially at grain boundaries where most dislocations occur and provide low energy binding sites. The concentration of trace elements are therefore expected to be greater at the grain boundaries than within the bulk volume of a crystal grain (De Yoreo and Vekilov 2003; Weiner and Dove 2003). Within the otolith structure, if preferential trace element binding occurs at grain boundaries it may permit ion migration, which would cause complications for the interpretation of otolith chemistry. In biominerals however the crystals are often enveloped within an organic layer, which may interfere with the adsorption of trace elements at the grain boundaries and enable incorporation into the bulk volume, though no evidence exists to support this hypothesis.

The interactions between the crystal lattice and the organic matrix, in terms of both geometry and stereochemistry, influence the growth of biominerals by altering the energy barrier to formation (Addadi and Weiner 1985; Weiner and Dove 2003). Inter-species differences in the otolith organic matrix are difficult to study directly but the wide variety of sizes and shapes of otoliths suggest there are differences (Carlstrom 1963). Whether the interaction of the organic matrix with the calcium carbonate crystal lattice differs from species to species remains unknown due to the difficulty of direct observation. Study of the preferred crystallographic orientations in otoliths from different species may however act as a proxy for understanding differences in the control exerted by the organic matrix and allow insight into the biomineralisation process and its influence over trace element uptake.

Otolith crystal orientation has been investigated for only two species to date. *Poecilia mexicana* otolith aragonite orientation was evaluated for the purpose of distinguishing between cave and surface dwelling fish, whilst the orientation of aragonite in *Carapus boraborensis* otoliths was studied to gain an understanding of the formation process in that particular species (Parmentier *et al.* 2007; Schulz-Mirbach *et al.* 2013). Crystallographic studies of many mollusc shells have revealed that there is much variation between species in the level of preferred alignment of the crystallographic axes (Lowenstam and Weiner 1989), which may in turn influence trace element incorporation and ultimately the usefulness as environmental proxies (Schöne *et al.* 2013). In otoliths, the variation of preferred crystallographic alignment between species and the influence of crystal and matrix orientation on the biomineralisation and trace element uptake remains unknown.

Implications

Much research is beginning to delve into the use of biominerals such as mollusc shells and otoliths for the reconstruction of environmental histories and more specifically temperature histories (Martin *et al.* 2004; Radtke *et al.* 1996; Townsend *et al.* 1992). Calcium carbonate biominerals incorporate trace elements in quantities which reflect the environmental conditions, although the more complex the organism the greater the biological regulation of uptake (Campana 1999). The use of otoliths in temperature

reconstructions, can produce positive (Kalish 1991; Limburg and E. 1995), negative (Radtke *et al.* 1990; Townsend *et al.* 1992) and no correlations at all (Gallahar and Kingsford 1996; Tzeng *et al.* 2002) between otolith and environmental chemistries. Inter-species differences, genetic and metabolic influences are postulated as reasons for the variation, and remain under investigation.

The uptake and incorporation of trace elements into the otolith structure is influenced by the complex interaction of biological and environmental factors, which in time need to be unravelled in order to reduce some of the assumptions currently facing otolith chemistry applications. The influence of the otolith biomineralisation process and more specifically the effect of it upon the crystal texture and orientation of the resulting otolith, are factors in need of investigation.

Analytical Approach

The inaccessibility of otoliths hinders the direct analysis of an otoliths growth and trace element uptake. Analysis of extracted otoliths is common practice in the field of fish ecology and one which we will also employ in this study. Once formed the otolith is inert, with no physiological reabsorption of the otolith as is seen with bone. Extracted from the fish, an otolith will remain inert allowing for the direct analysis of trace elements within the otolith structure, although it is expected there will be a degradation of organic material over time. Our analytical approach to the structural and chemical analysis of whole otoliths is expected to provide valuable insights into the biomineralisation mechanism.

Our study primarily employs electron microscopy and inductively coupled plasma mass spectrometry for the analysis of orientation and trace element chemistry in otoliths. The electron beam techniques, scanning electron microscopy (SEM), electron probe microanalysis (EPMA) and electron backscatter diffraction (EBSD) were employed to visualise the otolith growth patterns, quantitatively analyse the major and minor elements and to assess the aragonite orientation in otoliths respectively. Laser ablation inductively coupled plasma mass spectrometry (LA-ICP-MS) was used to quantify the trace elements in the otoliths. Raman microspectroscopy was employed to investigate

the orientation of the otolith organic matrix with respect to the aragonite. Powder X-ray diffraction was also used in order to assess the calcium carbonate phase of the otoliths, to confirm otoliths analysed were aragonitic. Further information on each analytical technique is provided below.

Scanning Electron Microscopy (SEM)

Scanning Electron Microscopy is a high resolution imaging technique, which has the potential to provide insight into the biomineralisation of otoliths. It is an electron beam based technique, in which a sample is bombarded with an electron beam and the resulting electron-matter interactions detected. SEM can provide detailed, high resolution morphological information using secondary electrons, which are electrons ejected from the top surface layers of the sample itself. In contrast backscattered electrons, which come from the incident beam and are elastically scattered through the sample, provide average compositional information about the sample. This is particularly beneficial in elucidating the difference between organic rich (D-band zones) and mineral rich zones (L-zone bands) within biominerals such as otoliths. SEM resolution is typically below 10nm, allowing visualisation with much greater detail than can be achieved optically.

Laser Ablation Inductively Coupled Plasma Mass Spectrometry (LA-ICP-MS)

Laser Ablation Inductively Coupled Plasma Mass Spectrometry is a highly sensitive technique for the detection of trace elements and isotopes in solid samples. It is routinely utilised in otolith research as a tool for monitoring chemical changes across the otolith growth bands.

LA-ICP-MS employs a laser as a sampling device in order to analyse solid materials such as otoliths. LA-ICP-MS employs a focused laser beam targeted on the sample surface to generate fine particles, a process known as ablation. The ablated particles are immediately transported on a stream of helium (He) gas, mixed in with argon (Ar) gas into the ICP-MS. Once sampled the material is introduced to an inductively coupled

plasma (ICP) which converts the atoms of the sample into positively charged ions (Figure 3).

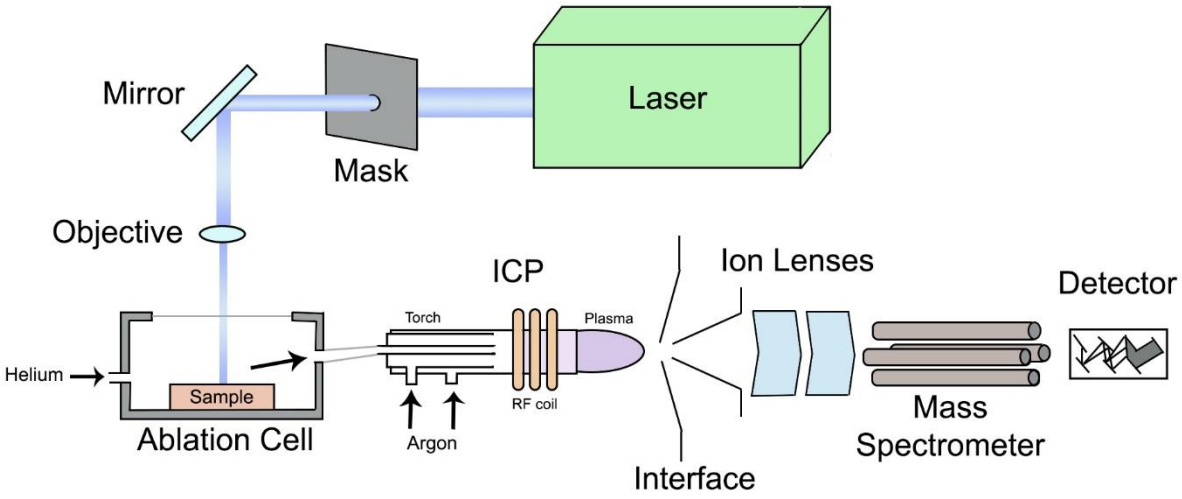

Figure 3: Schematic diagram of LA-ICP-MS showing the components of each system.

The plasma itself is generated in a stream of Ar gas contained within a quartz tube, known as a torch. The torch is surrounded by a cooled copper coil, through which a high frequency and high power electric current is passed. This generates a magnetic field, which causes collisions between free electrons and Ar atoms, producing Ar ions and more electrons in a cascade of Ar ionisation and hence the formation of a stable plasma. Stable plasmas reach temperatures up to 10,000K and are responsible for the conversion of sample atoms into positively charged ions.

The positively charged ions produced in the plasma are extracted into a vacuum system and focused by a set of electrostatic lenses into the mass spectrometer. The ion lenses are also responsible for the separation of the ions from photons and neutral particles to reduce background noise. The ions then pass into a quadrupole mass spectrometer which uses a combination of direct and alternating current electric fields to separate ions based on their mass to charge ratio (m/z). In ICP-MS singly-charged ions are produced almost exclusively meaning the mass to charge ratio is equal to the mass of the ion and isotopes can be measured directly. Detection in a quadrupole mass spectrometer occurs sequentially, with only one m/z being stable within the quadrupole at one time, however the quadrupole scans rapidly across the entire mass range.

Using a laser to introduce the sample allows for the introduction of solid samples, as well as the ability to resolve elemental and isotopic information spatially within a sample by moving the sample beneath the laser beam during analysis. LA-ICPMS is a highly sensitive technique with detection limits typically in the high ppb range however it is limited in spatial resolution by the laser beam diameter. The spatial resolution achieved by LA-ICPMS can range between 5 and 40µm depending on the sample type and the levels of trace elements present. The use of standard materials also allows for element composition to be quantified. LA-ICPMS can therefore be used to obtain highly accurate quantification at single spot locations within a sample or can be recorded in two-dimensional maps, which usually achieve greater spatial resolution, however with higher detection limits.

Electron Probe Microanalysis (EPMA)

Electron Probe Microanalysis (EPMA) is an electron beam based technique which allows quantification of major and minor elements in small selected areas in solid samples. A focused electron beam is used to excite X-rays from the sample. X-rays are generated by the bombardment of a sample with an electron beam. X-rays of characteristic wavelength are generated when a bombarding electron dislodges an inner shell electron from an atom in the sample. The vacancy in the inner shell causes an outer shell electron to fall into the vacancy, releasing the excess energy as an X-ray photon with a wavelength equal to the energy gap between the inner and outer shells of the atom from whence it came (Figure 4). X-Rays are produced by electronic transitions within the sample atoms and consequently X-ray lines characteristic of the elements present in the sample are produced and can be identified by their wavelengths.

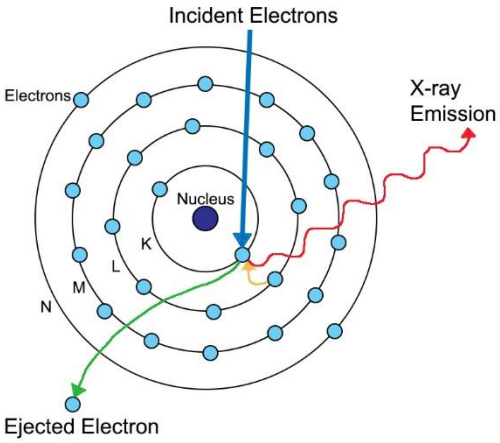

Figure 4: X-ray emission as a result of electron bombardment.

EPMA employs wavelength dispersive spectrometers (WDS) to detect the X-rays of interest in order to achieve quantitative analysis. X-rays generated from the sample, encounter a crystal with specific lattice spacing known as spectrometer crystal. X-rays encounter the spectrometer crystal at a specific angle and only X-rays that satisfy Bragg's Law, usually a single wavelength, are reflected to the detector. The wavelength which is reflected to the detector can be selected by varying the position of the spectrometer crystal relative to the sample because the X-ray source-crystal distance is a linear function of the X-ray wavelength. As a result wavelength dispersive spectrometry is limited to the analysis of X-rays from one element at a time, and the spectrometer position must be adjusted for each element. EPMA instruments are usually equipped with multiple WDS spectrometers in order to analyse multiple elements simultaneously (Figure 5).

EPMA achieves elemental quantification by comparison of the X-ray intensities emitted from standard materials and samples. Accuracy approaching ± 1% is obtainable and detection limits are typically in the region of 50ppm although new methods are beginning to achieve lower values. Spatial resolution is limited to around 1µm due to the spreading of the electron beam as it enters the sample, however this is sample dependent and can often be greater than 1µm. EPMA can be used to obtain highly accurate quantification at single spot locations within a sample or can be recorded in

two-dimensional maps, which usually achieve greater spatial resolution, however with higher detection limits.

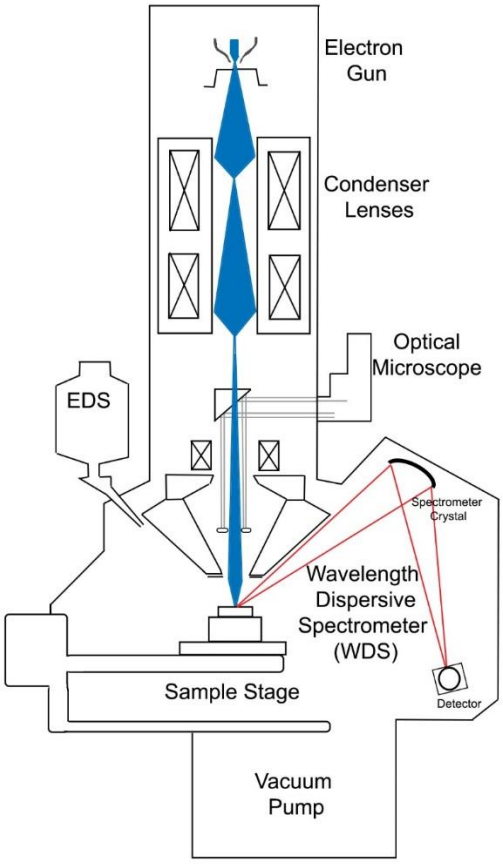

Figure 5: EPMA Schematic showing the design of a wavelength dispersive spectrometer, with the electron beam given in blue and the X-ray path given in red.

Electron Backscatter Diffraction (EBSD)

Electron Backscatter Diffraction (EBSD) is an electron beam based technique, conducted in a scanning electron microscope (SEM), and utilised to map crystal orientation. Since the introduction of electron backscatter diffraction patterns by Nishikawa and Kukuchi (Engler and Randle 2009), the technique has been steadily refined, resulting in the automated, in situ systems used today. EBSD began as a technique predominantly used in the field of metallurgy however has expanded into the fields of materials science, geology and more recently to investigations of biominerals (Engler and Randle 2009).

The EBSD system comprises a camera integrated with a phosphor screen detector. A polished crystalline sample is tilted to an angle of 70° relative to the electron beam, facing the detector. When an electron beam interacts with crystalline material at a low angle of incidence the electrons are diffracted through the lattice planes of the crystalline material before being backscattered. These diffracted electrons are detected on the EBSD phosphor screen as distinct bands, termed Kikuchi bands (Figure 6). These bands represent the unique crystallographic orientation of the crystal lattice through which the electrons have diffracted. The Kikuchi bands, or EBSD patterns, are interpreted and matched to a crystal phase and orientation. By scanning the electron beam across the sample surface, EBSD patterns can be collected at each point to construct a map of crystallographic orientation (Engler and Randle 2009).

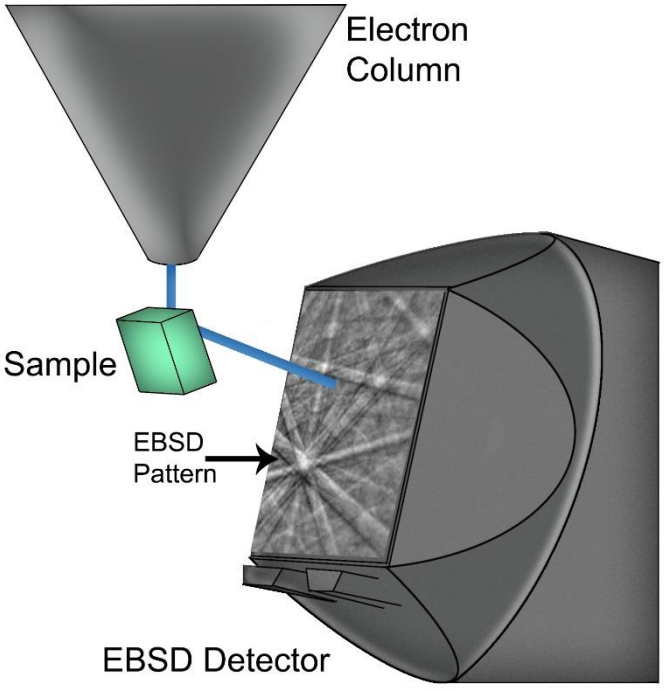

Figure 6: Schematic diagram of the EBSD detector and sample orientation within the SEM chamber.

Raman Microspectroscopy

Raman microspectroscopy is a spectroscopic technique which enables investigation of the molecular and mineral structures, including orientation, in sectioned otoliths by the collection of spectra using incident and scattered laser light (Bower 1972). Raman spectroscopy is a form of inelastic scattering of light in which an exciting laser photon interacts with a sample resulting in light to be scattered at a lower frequency. Provided there is a change in a molecules polarizability during vibration it will result in Raman scatter, and the frequency of the resulting scatter is determined by the energy of a samples characteristic molecular vibrations. Raman spectroscopy can therefore provide a fingerprint by which molecules can be identified by observing the vibrational, rotational and low-frequency modes in a system. Polarisation of Raman scattering has the additional ability to provide information on the orientation of both mineral and molecular structures, such as the organic matrices present in otoliths (Bower 1972; Lefevre *et al.* 2007; Rousseau *et al.* 2004). The orientation of organic matrices in biominerals has been investigated for bone using Raman microspectroscopy because it has the advantage of being a fast and simple method of characterisation which can be performed in-situ, preventing the loss of orientation information during organic matrix extractions (Raghavan 2011).

Raman microspectroscopy utilises a microscope to focus the laser beam onto the sample and collect the scattered light, which allows for in-situ collection of spectra from small areas on the otolith, approximately 10 µm in diameter. Raman spectra are acquired by the excitation of the sample by a laser of specific wavelength, 532nm, and the inelastically scattered Raman light is dispersed by single monochromators (1200 grating mm^{-1}) coupled to a CCD detector. The elastically scattered light, Rayleigh scatter, has the same energy as the incident light and is blocked by a holographic notch filter to prevent its interference. By polarising the incident laser light and the scattered light, the Raman spectra can be used to evaluate the orientation distribution of molecules, either qualitatively or quantitatively (Bower 1972; Lefevre *et al.* 2007; Rousseau *et al.* 2004).

Orientation can be defined by an orientation distribution coefficient $N(\vartheta)$ which can be expanded in a series of even Legendre polynomials. The order parameters of the series,

$\langle P_i \rangle$, can be determined experimentally though the number of order parameters accessible depends on the analytical technique applied (Bower 1972; Rousseau *et al.* 2004). X-ray diffraction is a powerful technique in the determination of crystalline orientation distributions, as all of the order parameters of the Legendre series can be obtained. X-ray diffraction is restricted to the analysis of crystalline materials though, so it does not allow for assessment of molecular orientations. Other techniques such as nuclear magnetic resonance (NMR) and electron diffraction can provide orientation information in molecular samples though the sample preparation in both cases is difficult. Raman microspectroscopy however allows for the characterisation of molecular and mineral orientation in whole or sectioned otoliths, from which the order parameter $\langle P_2 \rangle$ can be calculated (Lefevre *et al.* 2007; Raghavan 2011; Rousseau *et al.* 2004). The order parameter $\langle P_2 \rangle$, referred to as Herman's orientation function, qualitatively describes the extent of orientation of a polymer axis relative to another axis of interest, where a value of -0.5 defines perfect perpendicular orientation, a value of +1 defines perfect parallel orientation and a value of 0 defines random orientation with respect to the reference axis (Raghavan 2011).

Powder X-ray Diffraction (XRD)

Powder X-ray diffraction (XRD) is a technique commonly employed in the analysis of crystalline materials, in their identification, and in structure and purity determinations. X-rays are diffracted through a powdered sample to produce a diffraction pattern characteristic of the structure of that particular crystalline compound. The X-rays striking the sample at an angle of θ are reflected by the atomic planes in the crystal. The reflected rays will either be out of phase and interfere destructively or be in phase and interfere constructively. Successful reflection is given by Braggs Law, $n\lambda = 2d\sin\vartheta$, where n is any whole number, λ is the wavelength of the X-rays, d is the interplanar spacing and ϑ is the angle of incidence. Braggs Law can therefore be used in the determination of the interplanar spacing of a crystal and with the reflection intensity the crystal structure can be determined. Diffraction patterns are therefore essential as a means of mineral identification, because a mineral is defined by its structure and composition and no two minerals can have absolutely identical diffraction patterns.

Objective/Aims

This project aims to uncover the physical regulation of the otolith biomineralisation process in order to begin reducing the assumptions inherent in the current interpretation of otolith chemistry. Trace elements incorporated into the growing otolith structure provide a biological archive which allows for the reconstruction of fish migration pathways, stock identification, age validations and elucidation of environmental histories, however accurate interpretation of otolith data is hindered by the physiological regulation of the otolith biomineralisation process. This project will characterise the microstructure, chemistry and crystallography of otoliths of four marine fish species in order to address two inter-dependent aims, centred around gaining insight into the otolith biomineralisation mechanism and its influence on elemental uptake.

Chapter two will examine the otolith structure and explore the relationship between the crystalline aragonite structure and the underlying organic matrix template. Specifically this study will characterise the orientation and crystal habit of the aragonite and the orientation and alignment of the organic matrix template of marine otoliths to assess whether otolith growth control varies between species or a common mechanism exists. The thorough examination of the otolith structure will provide an insight into the mechanism of biomineralisation and a context for subsequent elemental analysis.

Chapter three will optimise the analysis of low level minor elements by electron probe microanalysis in order to investigate the distribution of minor and trace elements in the otoliths of marine species and explore the relationship between elemental distribution and the otolith structure. Specifically this study will characterise the distribution of ecologically important elements, including Sr, S, Mg and Ba, and their relationship to the microstructure examined in Chapter 2 to assess the impact of the biomineralisation process on the occlusion of elements into the otolith structure.

A thorough characterisation of four marine species of otoliths at the microstructural level will be carried out by a range of techniques. Microstructural analysis of the aragonite crystal orientation and habit, and the orientation and alignment of the organic matrix template will be carried out by a range of scanning electron microscopy (SEM)

techniques, including secondary electron and backscatter electron imaging, and electron backscatter diffraction (EBSD) as detailed in Chapter 2. Characterisation of the elemental distribution will be optimised and carried out by electron probe microanalysis (EPMA) and laser ablation inductively coupled plasma mass spectrometry (LA-ICPMS) as detailed in Chapter 3.

Chapter 2

Investigation of the orientation and alignment of otolith aragonite with the organic matrix provides insight into the mechanism of otolith growth

Abstract

The orientation of aragonite and the organic matrix in otoliths of four marine species (*Platycephalus bassensis, Chrysophrys auratus, Trachurus novaezelandiae and Lates calcarifer)* were investigated to determine the mechanism of otolith mineralisation. Electron backscatter diffraction (EBSD) confirmed that aragonite grain growth is preferentially aligned with the otolith growth axis in all species analysed. Aragonite grew with the c-axis aligned parallel with the otolith growth axis. The a- and b- axes aligned perpendicular to the otolith growth axis, with rotation about the c-axis of approximately 60 degrees, due to aragonite twinning. Scanning Electron Microscopy (SEM) imaging of acid etched otoliths revealed the presence of the insoluble organic matrices. Raman microspectroscopy confirmed the insoluble organic matrices aligned perpendicular to the otolith growth axis, and parallel to the a- and b- axes. The results show that a spatial relationship exists between the otolith aragonite crystallographic axes and the insoluble organic matrix, indicating that the aragonite mineral growth is directed upon a matrix template via stereochemically controlled nucleation.

Introduction

Biomineralisation

The highly controlled growth of biominerals is regulated by organic macromolecules, but the mechanism of growth for each individual biomineral is so varied that the role of the macromolecules is only beginning to be understood. The growth of biominerals in precise locations within an organism and the formation of specific shapes and crystallographic orientations point towards active control of nucleation and growth (Lowenstam and Weiner 1989; Weiner 1986). Evidence suggests that organic compounds serve as a template for growth, providing preferential sites for nucleation

and controlling the orientation of the resulting crystals (De Yoreo and Vekilov 2003). X-Ray and electron diffraction studies of mollusc shells reveal that collagen-like proteins form a structural framework which is aligned with the mineral crystallographic axes, indicating that crystal growth occurs upon, and is constrained by, an organic matrix framework (Figure 7) (Weiner *et al.* 1983; Weiner and Traub 1980). Crystallographic studies of many mollusc shells have revealed that there is much variation between species in the level of preferred alignment of the crystallographic axes (Lowenstam and Weiner 1989), which may in turn influence trace element incorporation and ultimately their usefulness as environmental proxies (Schöne *et al.* 2013).

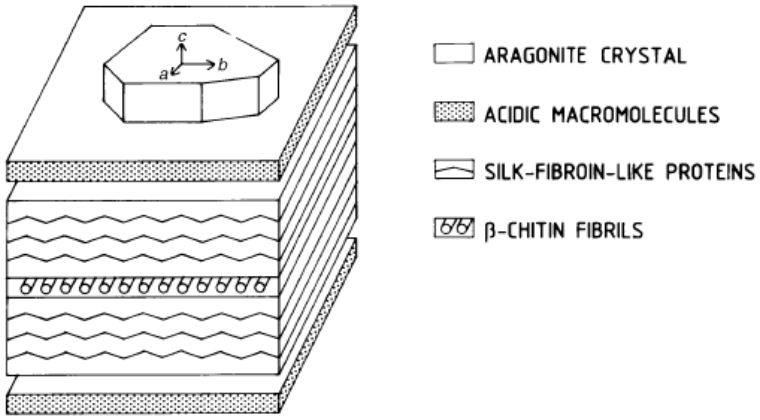

Figure 7: Schematic diagram of the spatial relationship between the aragonite crystallographic axes and the underlying organic matrix (Lowenstam and Weiner 1989).

The interactions between the crystal lattice and the organic matrix, in terms of both geometry and stereochemistry, influence the growth of biominerals by altering the energy barrier to formation (Addadi and Weiner 1985; Weiner and Dove 2003). The interaction of the organic matrix with the calcium carbonate crystal lattice may differ from species to species and in turn the trace element incorporation may differ. Study of the preferred crystallographic orientations in otoliths from different species may act as a proxy for understanding differences in the control exerted by the organic matrix and allow for assessment of the influence exerted over trace element uptake.

Otolith Organic Matrices

In the organic matrices of otoliths, a variety of proteins, collagens, amino acids, proteoglycans and organic macromolecules have been detected but the specific role of each in the biomineralisation process remains unclear (Borelli *et al.* 2003; Borelli *et al.* 2001; Tohse *et al.* 2008). Approximately half of the otolith matrix molecules are water insoluble and are thought to make up a structural framework used to direct calcification. Insoluble organic matrices, termed otolin-1, have been extracted and shown to be a collagen-like protein most likely involved in control of the shape and size of the otolith (Murayama *et al.* 2002). Soluble organic matrices are characterised by an abundance of acidic amino acids, and are suspected to be involved in nucleation and growth of the otolith aragonite. A water soluble protein from zebra-fish was characterised as having high acidic amino acid content and its control of calcium carbonate morphology and polymorphism was observed experimentally (Sollner *et al.* 2003). The wide variety of soluble organic matrices present in the otolith and the variation between species leaves the question of specific function of these organics unclear. The otolith soluble organic matrices were extracted and used to experimentally induce the overgrowth of aragonite on an aragonitic otolith (Falini *et al.* 2005). While the soluble organic matrices in this case directed the polymorph formed, the crystals overgrown experimentally showed no preferred orientation, which follows from the assumption that the insoluble matrices, not the soluble matrices, are responsible for the structural control (Falini *et al.* 2005).

Aragonite Crystal Structure

Aragonite is a naturally occurring form of calcium carbonate exhibiting orthorhombic crystal symmetry. Under standard temperatures and pressures aragonite is thermodynamically unstable and will eventually alter to calcite (Wray and Daniels, 1957). Aragonite can precipitate in a variety of crystal textures, which form both naturally and biologically. The aragonite structure consists of paired, superimposed triangular CO_3 groups, which are rotated by 60°, lie in the (001) plane and are linked by 9 cations, giving aragonite 9-fold coordination (Figure 8) (Strunz and Nickel, 2001). Studies of otolith aragonite show a predominance of the acicular and prismatic habits,

with twinning present in the grains (Gauldie and Nelson, 1988; Parmentier et al., 2007; Zhuo et al., 2009).

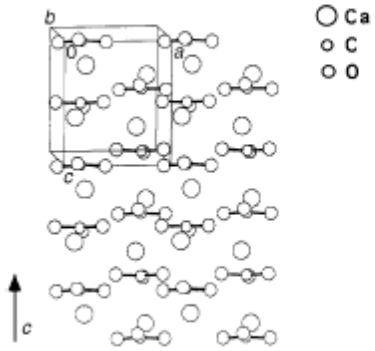

Figure 8: Aragonite crystal structure, tilted out of plane on the c axes by 5° to improve perspective (Weiner and Addadi, 1997).

Twinning

The growth of twinned crystals is a consequence of the symmetry of the internal structure. A twinned crystal is a single crystal which is divided into two or more parts, with one in reversed structural orientation with respect to the next. In aragonite, a plane runs through the lattice, across which the lattice inclination may have its orientation reversed without disturbing the fit between the lattice rows. Twinning will arise when atom groups are arranged to form part of the lattice on either side of the plane reversal. In a growing crystal such an orientation change results in the subsequently added atom layers assuming the new orientation and a twinned crystal results (Battey and Pring 1997).

Aragonite exhibits mimetic twinning, whereby twinning is repeated within one crystal resulting in pseudo hexagonal symmetry (Figure 9). Twinning is favoured in aragonite due to the near symmetrical arrangement of atom planes and axes. In the growth of crystals, minimising the internal lattice energy is the optimum condition but twinning disrupts this and increases the lattice energy. If the mismatch between neighbouring atoms is small, the reversal of atom groups one bond length from the plane doesn't impact the total lattice energy much and twinning can occur, as is seen in aragonite (Battey and Pring 1997).

Twinning initiation is credited to stacking faults which occur in the early stages of crystal growth, during which the crystal energy field needed to retain atoms in the correct orientation is small. If the crystal grows rapidly from a saturated solution the fault will be preserved as a twin. Stacking faults can occur at any time during crystal growth, but are more likely in the early stages of crystal nucleation. The growth of crystals is not an equilibrium process but occurs in response to a changing environment, which may favour the event of stacking fault initiation and therefore twinning (Battey and Pring 1997; Bloss 1971).

The occurrence of twinning in otoliths and the implications of it has been debated, with suggestions that aragonite twinning aids otolith growth and observations that twinning is not involved in the growth mechanism (Gauldie 1988; Parmentier *et al.* 2007). It is suggested by Gauldie et al (1988), that twinning leads to rapid otolith growth which in turn leads to the formation of the incremental daily growth rings, however there is currently no definitive evidence linking the two (Gauldie and Nelson 1988). The presence or absence of twinning in otolith aragonite may however give an insight into the biomineralisation mechanism and the level of control exerted by the organic matrix over aragonite orientation.

Otolith Aragonite Growth

Calcium carbonate crystallises into three different polymorphs, calcite, aragonite and vaterite, with calcite being the most thermodynamically stable polymorph (Wray and Daniels 1957). The growth of aragonite in otoliths indicates that there is thermodynamic control of the growth by the organic matrix. Experimental evidence from calcium carbonate overgrowth on the surface of otoliths has suggested that the intra-crystalline macromolecules associated to the otolith favour aragonitic polymorphism (Falini *et al.* 2005). Otolith aragonite growth can be controlled at the thermodynamic level and at the kinetic level. While polymorph is determined by thermodynamic control, crystal habit may be predominantly determined kinetically in otoliths. The habit of the crystal depends on a number of factors including growth speed, temperature, and the lack of uniformity in the chemical composition of the endolymph which could prevent or enhance growth in certain directions (Parmentier *et al.* 2007).

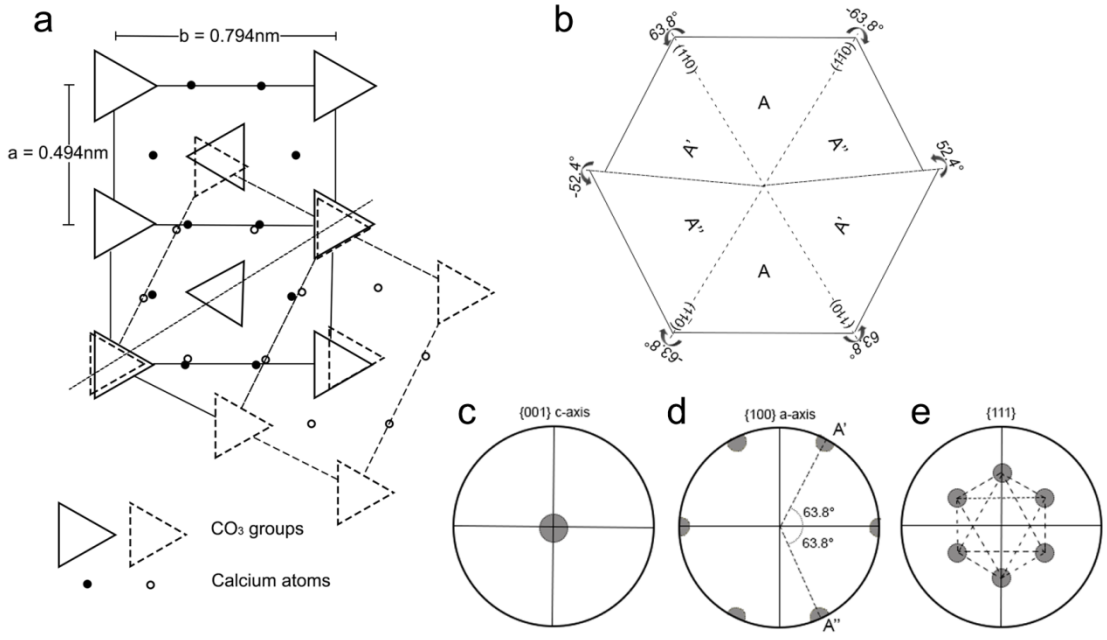

Figure 9: a) Relation of twinning to the structure in aragonite, b) Aragonite mimetic twinning schematic. Aragonite twins on [110] at an interfacial angle of 63.8° to produce interpenetrant triplets of pseudo-hexagonal shape. A is the parent individual, A' is derived by rotation twinning about the normal to (110) and A'' is derived by rotation about the normal to (1$\bar{1}$0). c-e) Pole figure representation of aragonite twinning as seen in Electron Back Scatter Diffraction (EBSD) data. To aid interpretation the c-axis is aligned with the EBSD normal direction. d) The [100] or a-axis shows the three preferred crystal orientations, A, A' and A''. The angles between A and A', and between A and A'' are 63.8° due to aragonite twinning. e) The twinning is also evident in the [111] but because the orthorhombic crystal has two diads the three preferred orientations have four-fold symmetry (Battey and Pring 1997).

Otolith Aragonite Orientation

Otolith crystal orientation has been investigated by Electron Backscatter Diffraction (EBSD) for only two species to date. *Poecilia mexicana* otoliths were evaluated by EBSD for the purpose of distinguishing between the otoliths of cave and surface dwelling fish, whilst the orientation of aragonite in *Carapus boraborensis* otoliths was studied to gain understanding of the formation process (Parmentier *et al.* 2007; Schulz-Mirbach *et al.*

2013). Neither study showed the aragonite twinning present in otolith aragonite, nor investigated the spatial relationship between the mineral orientation and the organic matrix orientation. In otoliths, the variation of preferred crystallographic alignment between species and the influence of orientation on the biomineralisation process and trace element uptake remains unknown.

Otolith Organic Matrix Orientation

Raman spectroscopy has been employed in several otolith studies investigating the distribution of the organic and mineral fractions in otoliths towards understanding biomineralisation (Jolivet *et al.* 2008; Zhang *et al.* 2008). The orientation of the otolith organic matrix has not been reported previously, though studies on silk proteins in spiders and silk worms and on collagen in bone have utilised Raman spectroscopy to measure the orientation of organic matrices in biomaterials (Lefevre *et al.* 2007; Raghavan 2011; Rousseau *et al.* 2004). Mollusc shell organic matrix orientations have been investigated by electron diffraction, where a spatial relationship was shown to exist between the organic matrix and the aragonite crystal, hence supporting the idea of epitaxial mineral growth upon a matrix template (Weiner *et al.* 1983). Morphological studies of newly formed crystals in mineralised tissues such as bones or shells indicated that they are generally orientated in a preferred direction, suggesting that their nucleation and growth is controlled by the matrix substrate (Weiner *et al.* 1983).

We hypothesise that otolith growth is controlled and directed by the insoluble organic matrix and suggest it specifically acts as a template for the aragonite growth by exerting control over the aragonite crystal habit and orientation. The objective of this study is to utilise scanning electron microscopy (SEM), electron backscatter diffraction (EBSD) and Raman microspectroscopy to investigate the relationship between the insoluble organic matrix and the aragonite microstructure, specifically aragonite crystal habit and orientation. We aim to evaluate the structural relationship between the organic and inorganic components of the otolith in order to improve our understanding of the mechanism of biomineralisation.

Methods

Sample Preparation

Sagittal otoliths were obtained from specimens of sand flathead (*Platycephalus bassensis*, Platycephalidae), snapper (*Chrysophrys auratus*), barramundi (*Lates calcarifer*) and mackerel (*Trachurus novaezelandiae*). Upon removal otoliths were rinsed in ultrapure water to remove any adhering tissue, air dried in a laminar fume hood, and stored in microcentrifuge tubes for later examination. Otoliths were subsequently embedded in two part epoxy resin and sectioned through the core to expose the growth increments using a Buehler ISOMET low speed saw. Sectioned otoliths were polished on a Struers TegraPol mechanical polisher, with a graded series of lapping cloths starting with 9 µm, 3 µm and finishing on 0.04 µm colloidal silica. Between each polish, samples were cleaned ultrasonically and rinsed thoroughly in ultrapure water. The distribution of the organic matrix was visualised on samples which were sectioned, polished and acid etched. Prior to scanning electron microscopy (SEM) otoliths were etched in acetic acid for 30s to remove the soluble organic matrix and enhance visualisation of the insoluble, collagen like matrix. For comparison non-biological aragonite was treated in the same way.

Powder X-Ray Diffraction

Powder X-Ray Diffraction was employed to confirm the otolith mineral as aragonite before imaging, EBSD and Raman analysis. XRD were collected on a Huber G760 100mm image plate Guinier Camera with *Kα1* radiation (λ = 1.78892 Å). Samples were ground in acetone, spread uniformly on MYLAR film and mounted on the sample oscillation unit for data collection.

Scanning Electron Microscopy and Image Analysis

Scanning electron microscopy (SEM) was employed to visualise the growth patterns and grain microstructure of the otoliths, primarily by backscatter electron imaging (BSE). All

images were acquired on a FEI Quanta 450 Field Emission Gun Environmental SEM (Eindhoven, Netherlands) operated in low vacuum mode at 20 kV.

Electron Backscatter Diffraction

Electron Backscatter Diffraction (EBSD) was employed to determine the grain orientation across the otolith sections. EBSD patterns were acquired on a Phillips XL30 FEG SEM (Eindhoven, Netherlands) equipped with an Oxford Instruments Channel 5 Nordlys EBSD detector. Operating conditions include an accelerating voltage of 15 kV for EBSD mapping, at a tilt angle of 70° and a working distance of 20 mm. Aragonite was indexed with a *Pcmn* unit cell setting with lattice parameters: a_0 = 4.9616 Å, b_0 = 7.9705 Å and c_0 = 5.7394 Å (DeVilliers 1971).

EBSD patterns were indexed with the HKL Flamenco software, which calculates the mean angular deviation (MAD) of the EBSD patterns to the indexed orientation. Indexing was accepted only when the MAD fell below 1.3. A two stage clean up procedure was performed following data collection. First, all single pixel indexed points with 8 nearest neighbour pixels of a different orientation were reassigned to the orientation of the nearest neighbours. Secondly, all non-indexed points with 8 nearest neighbours of the same orientation were reassigned to the orientation of the nearest neighbours in an iterative process. This clean-up procedure ensures that the final data on which analysis and interpretation is based are reliable.

Raman Microspectrometry

Raman microspectrometry was utilised to confirm the presence of organic matrices within the aragonite structure and qualitatively calculate the orientation of the insoluble organic matrix. Raman spectra were collected using a Nanonics-Horiba XploRA Raman microspectrometer equipped with polarisers. Raman spectra were excited by a 532nm laser focused onto the sample by a microscope using a 100x objective lens (numerical aperture 0.9). The incident and scattered light was filtered by polarisers and dispersed by a 1200 gratings mm-1 monochromator, using an entrance slit of 50 µm. Each spectra was acquired twice for 240s and averaged to reduce noise. No damage to

the sample surface was observed during collection. Peak fitting and background subtraction was performed using Horiba data analysis.

For orientation calculations polarised Raman spectra were collected by the procedure as described elsewhere (Raghavan 2011; Rousseau *et al.* 2004) from locations on a sectioned otolith of each species, and an otolith powdered sample. In all experiments the incident laser beam was polarised either parallel (*x*) or perpendicular (*y*) to the c-axis of the otolith aragonite. The scattered light was polarised either parallel or perpendicular to the polarisation direction of the incident light. The intensities (I) of the resulting four possible polarisations are given by their excitation and detection polarisations, I_{XX}, I_{YY}, I_{XY} and I_{YX}.

Polarized Raman spectroscopy provides the second-order parameter, <P2> which is used to describe the extent of orientation relative to a reference axis. The refractive index of the aragonitic otoliths was assumed to reflect that of mineral aragonite and was set as 1.65. Assuming a uniaxial cylindrical symmetry, the orientation order parameters <P2> was calculated for the insoluble organic matrix component of the otolith from the intensity ratios, R_x and R_y, where $R_X = I_{XY}/I_{XX}$ and $R_Y = I_{YX}/I_{YY}$, and the parameter *a.* The parameter *a,* of the Raman tensor, was determined from the isotropic depolarization ratio, R_{iso}, using an otolith pressed powder where $R_x = R_y = R_{iso}$. A detailed description of the derivation of the orientation order parameters is given by Rousseau et al. 2004 and reproduced in MATLAB code by Raghavan 2011.

Results

Powder X-Ray Diffraction

The otoliths were confirmed to be aragonitic by powder x-ray diffraction (XRD) prior to imaging and analysis. The mineral database matched all spectra as aragonite (Figure 10).

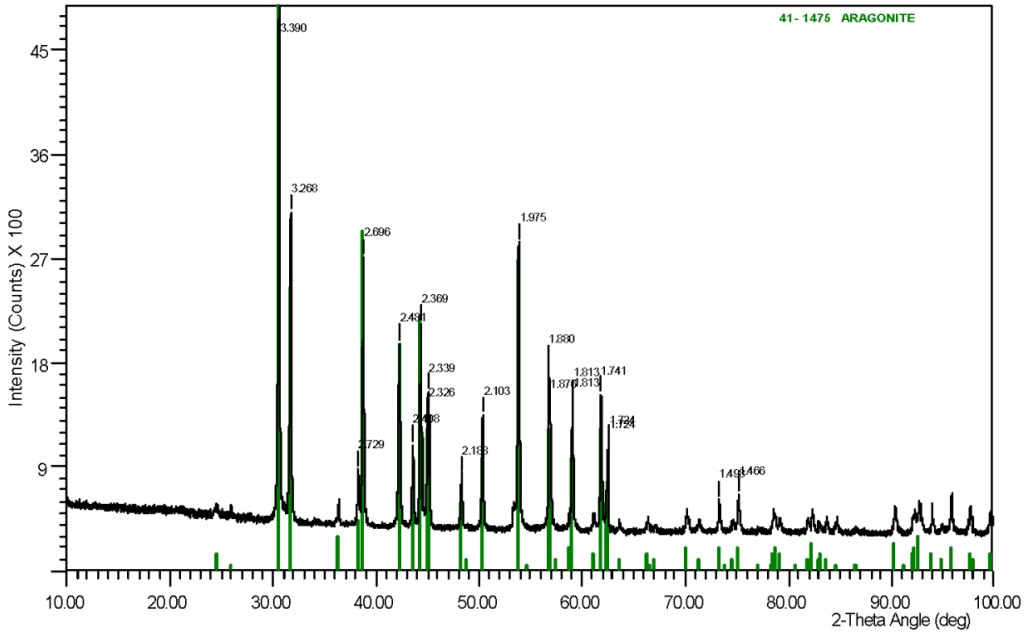

Figure 10: Powder XRD spectra of otolith aragonite, showing the matching aragonite peaks in green.

Scanning Electron Microscopy Imaging

The SEM images depict the characteristics of the microstructure of *P. bassensis, C. auratus, T. novaezelandiae* and *L. calcarifer* aragonite and the organic matrix within respectively. Sectioned otoliths of all species examined exhibit the typical alternating paired D-zone bands (areas rich in organic material) and L-zone bands (areas rich in calcium carbonate) (Figure 12). D-zone bands were clearly visible on the otoliths anti-sulcal side, though the thinner daily growth bands on the sulcal side were not always distinct. Backscatter electron imaging (BSE) revealed the presence of the D-zone bands throughout the aragonite grains. Acicular microstructure (crystal fabrics) dominates the otolith with growth occurring outwards from the core in a fan like manner. Prismatic

microstructure is also present on the otoliths, however it is predominantly present only on the anti-sulcal side. The change in crystal habit usually occurs abruptly, creating a distinct boundary between the acicular and prismatic habit types (Figure 11).

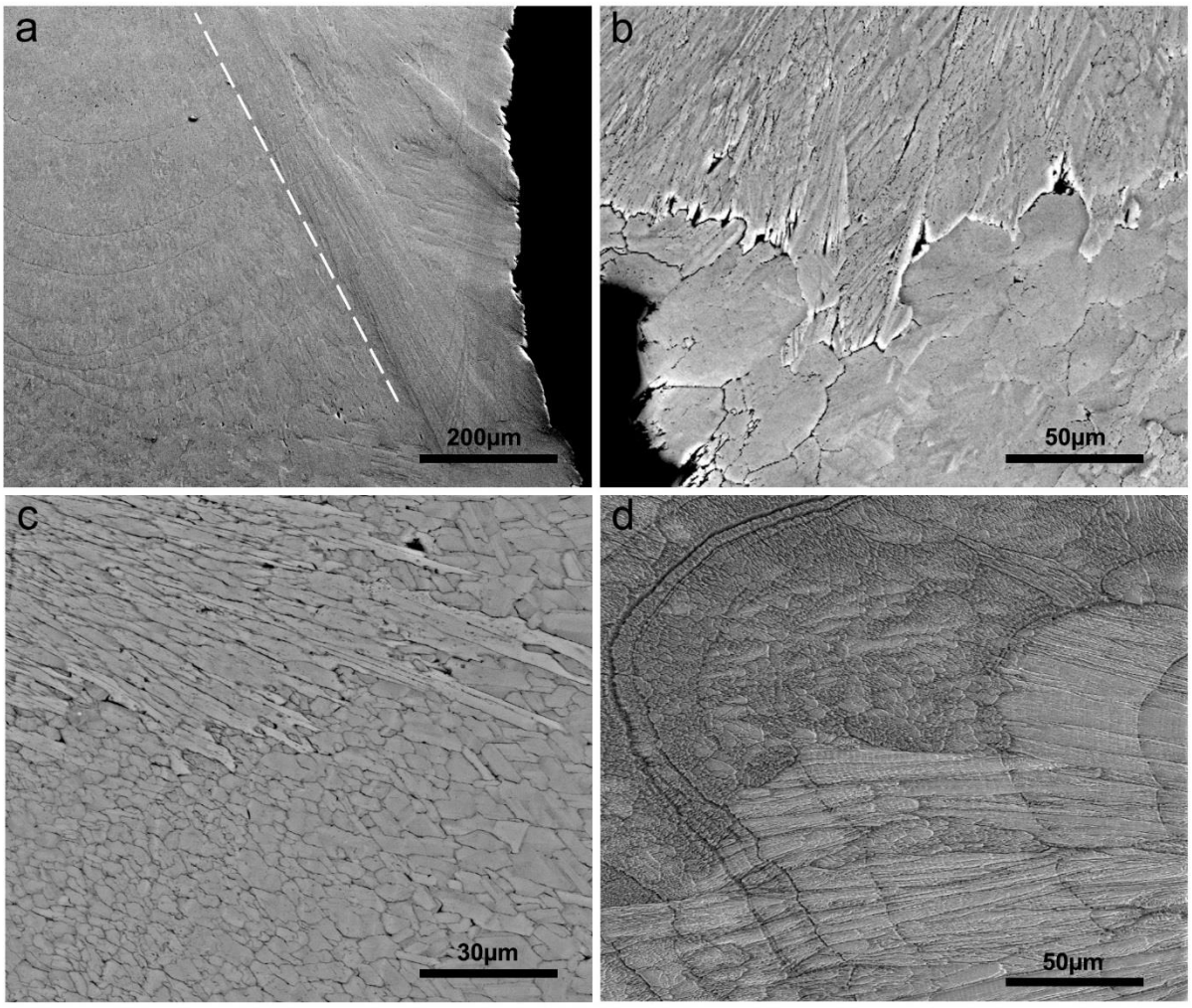

Figure 11: SEM images of the interface between the prismatic and acicular habits of aragonite in a)*, P. bassensis b) T. novaezelandiae, c) L. calcarifer* and *d) C. auratus*. In all species the acicular habit was dominant across the majority of the otolith however the anti-sulcal side exhibited a prismatic habit.

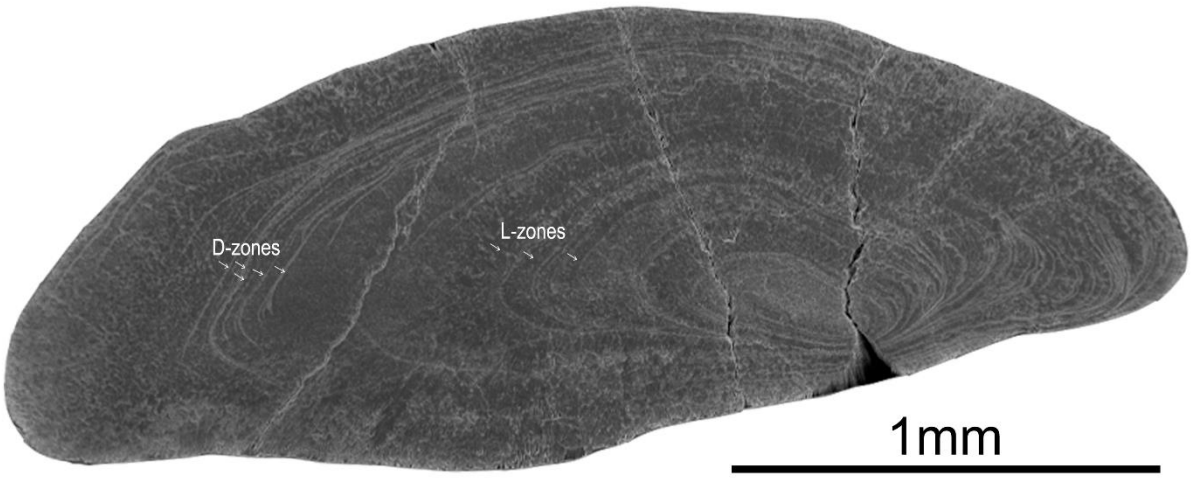

Figure 12: Otolith imaged in cross-section by scanning electron microscopy, SE charge contrast imaging, showing the growth increments. The D-zones, or the organic rich zones, are the thin bright bands as marked on the image. The L-zones, or the mineral rich zones, are the thicker dark bands as marked on the image.

On the sulcal side, where the bulk of otolith growth occurs, the D-zone bands were thinner and the L-zone bands were more defined in all species. Toward the anti-sulcus, grain size and L-zone band width was compressed, whereas the D-zone bands were broader, possibly due to a lower degree of calcification away from the sensory epithelium.

Etching of the otolith aragonite (Figure 14) reveals the presence of two types of organic matter i) insoluble organic matrix fibrils which tie aragonite grains together across the D-zones and ii) soluble organic fibrils which form a network within the aragonite grains (Figure 15). The soluble organic matrix is not observed directly but rather by removal of the soluble matrix from within the aragonite grains, leaving a network of empty spaces within the grains. The organic matrix network within the aragonite grains is dense and forms a substantial part of the grain. Such a network was absent in abiotic mineral aragonite treated in the same way (Figure 13).

In all species the insoluble organic matrix was visible in the etched D-zones, extending across the gap left by the soluble organic material removed in the acid etch. The aragonite grains are tied together by organic material present in the otolith D-zones, extending across the D-zone as fibrils approximately 100nm in width.

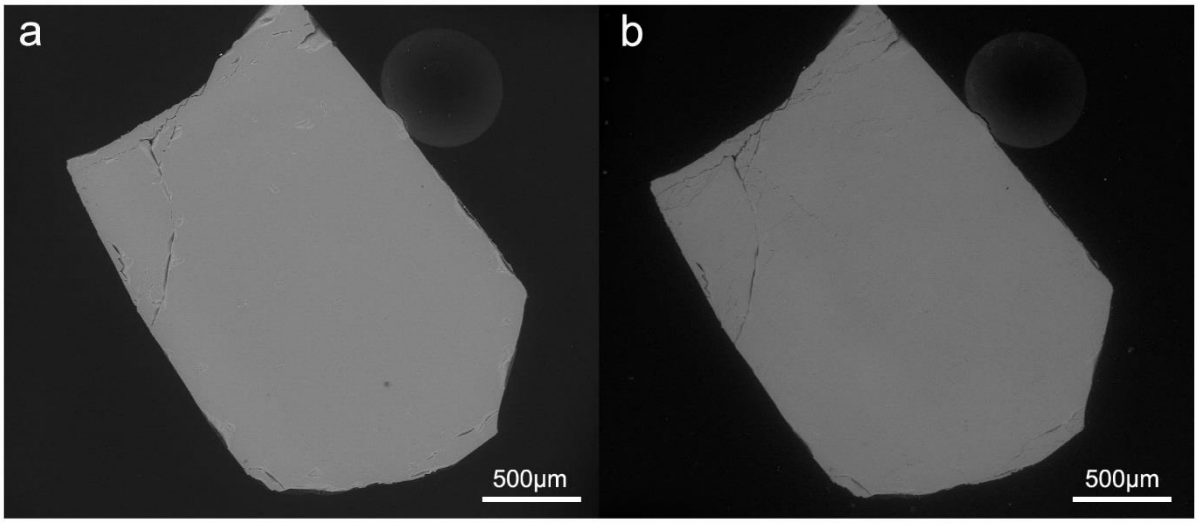

Figure 13: Abiotic mineral aragonite backscatter electron images a) untreated and b) etched for 120s with acetic acid. The abiotic mineral aragonite exhibits no etching effect as is seen for otolith aragonite due to the lack of organic material in abiotic aragonite.

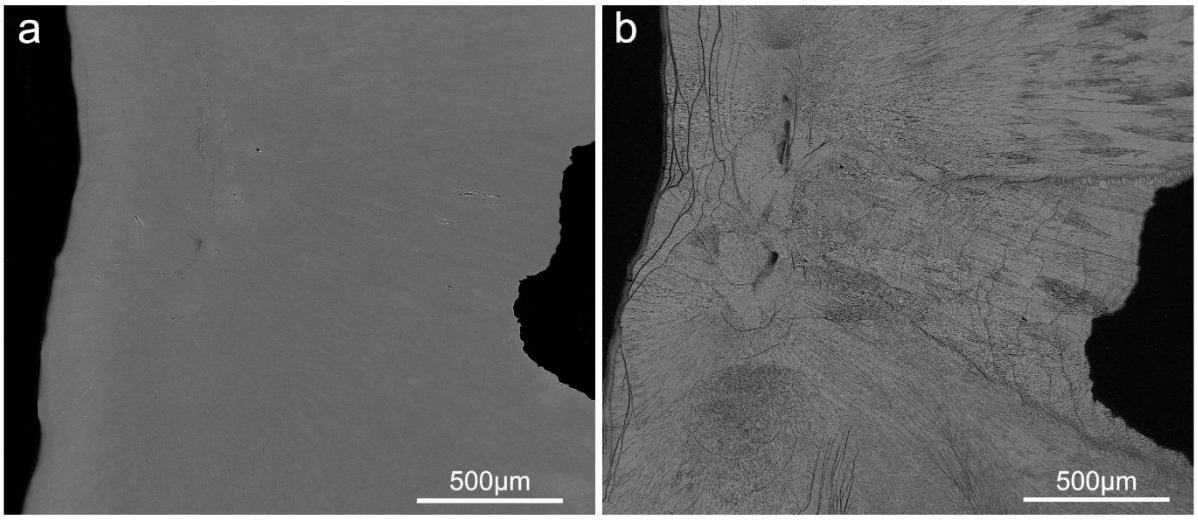

Figure 14: *Chrysophrys auratus* otolith cross section backscatter electron images, a) before etching and b) following etching with acetic acid for 30s. The organic rich growth bands are etched away, appearing as dark bands.

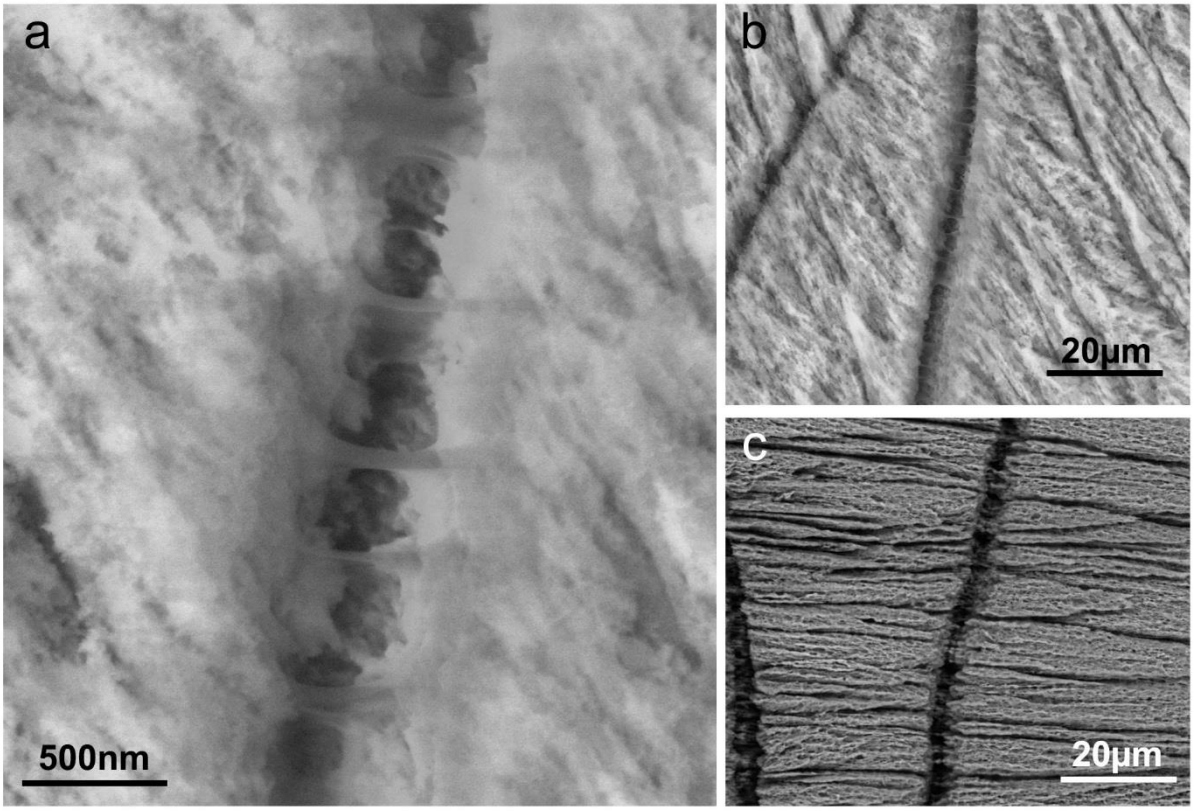

Figure 15: SEM images of a *Chrysophrys auratus (*snapper) otolith in cross section following etching with acetic acid for 30s. The organic rich growth bands are etched away, appearing as dark bands. Within the etched organic bands there remains organic material which bridges the band, the collagen-like protein, which is aligned perpendicular to the aragonite c-axis and the otolith growth axis and likely acts as a template to aragonite growth. (a) High magnification secondary electron image of the insoluble organic matrix stretching across the D-zone after removal of the soluble organic components, (b) Lower magnification secondary electron image of the insoluble organic matrix after 30s of etching. With longer etching times, 120s, as in (c) the aragonite grains also show, under backscatter electron imaging, considerable etching likely due to the removal of organic material present as a network within the aragonite grains.

Electron Backscatter Diffraction

Strong crystallographic directionality was evident throughout the analysed areas on all species, with aragonite grains exhibiting c-axes alignment with the direction of otolith

growth, (Figure 16). The crystallographic orientation maps measured by EBSD use inverse pole figure (IPF) colouring, indicating which crystal axis is parallel to the X-, Y- or Z-axis of the EBSD map (Figure 16 a-d). The pole figures display the orientational density distribution in the a-, b- and c-axis along with the (111), to highlight the presence of twinning (Figure 16). The aragonite grains are crystallographically co-orientated over large portions of the otolith.

Figure 16 shows the EBSD crystallographic orientation maps of the sulcal side of the otoliths, in which the EBSD band contrast (the quality of the EBSD pattern) is superimposed on the IPF colouring. The grain boundaries become visible in the band contrast as dark lines, because the EBSD pattern is weak at grain boundaries. The statistics of the crystallographic orientation is plotted by the pole figures and the grain boundary misorientation. The pole figures show that the crystallographic c-axis is aligned parallel to the otolith growth axis, while the a- and b- axes are distributed around the c-axis, however the distribution is not random due to the influence of aragonite twinning. The a- and b- axes show the presence of three pairs of reflections arising from the diad symmetry of three preferred orientations. The angles between two of the three orientations are consistent with the aragonite twinning angle of the (110) planes, ie. 63.8° (Checa *et al.* 2013; Griesshaber *et al.* 2012; Karney *et al.* 2012; Mukai *et al.* 2010).

Evaluation of the misorientation data gives a probability distribution of grain boundary misorientations, (Figure 16), with two major maxima in all species. A peak arises for small angle grain boundary misorientations (<5°) and a maximum at 64° corresponding to the (110) twinning orientation.

EBSD maps of otoliths of all species indicate that the aragonite c-axis is aligned with the otolith growth direction (Figure 16). The a- and b- axes show the presence of three pairs of reflections arising from the aragonite twinning. The aragonite twin reflections are less evident in the *C. auratus* otoliths than the other species, and the a- and b-axes pole figures show a continuous band of orientations around the c-axis, rather than the distinctive aragonite twin reflections. The grain boundary misorientation plots indicate that the majority of grain boundaries are either low angle boundaries, less than 5°, or fall between 60-70° due to aragonite twinning. In otoliths of *C. auratus* (Figure 16d) the

twinning is present to a lower degree than is evident for the other species (Figure 16a, b, c).

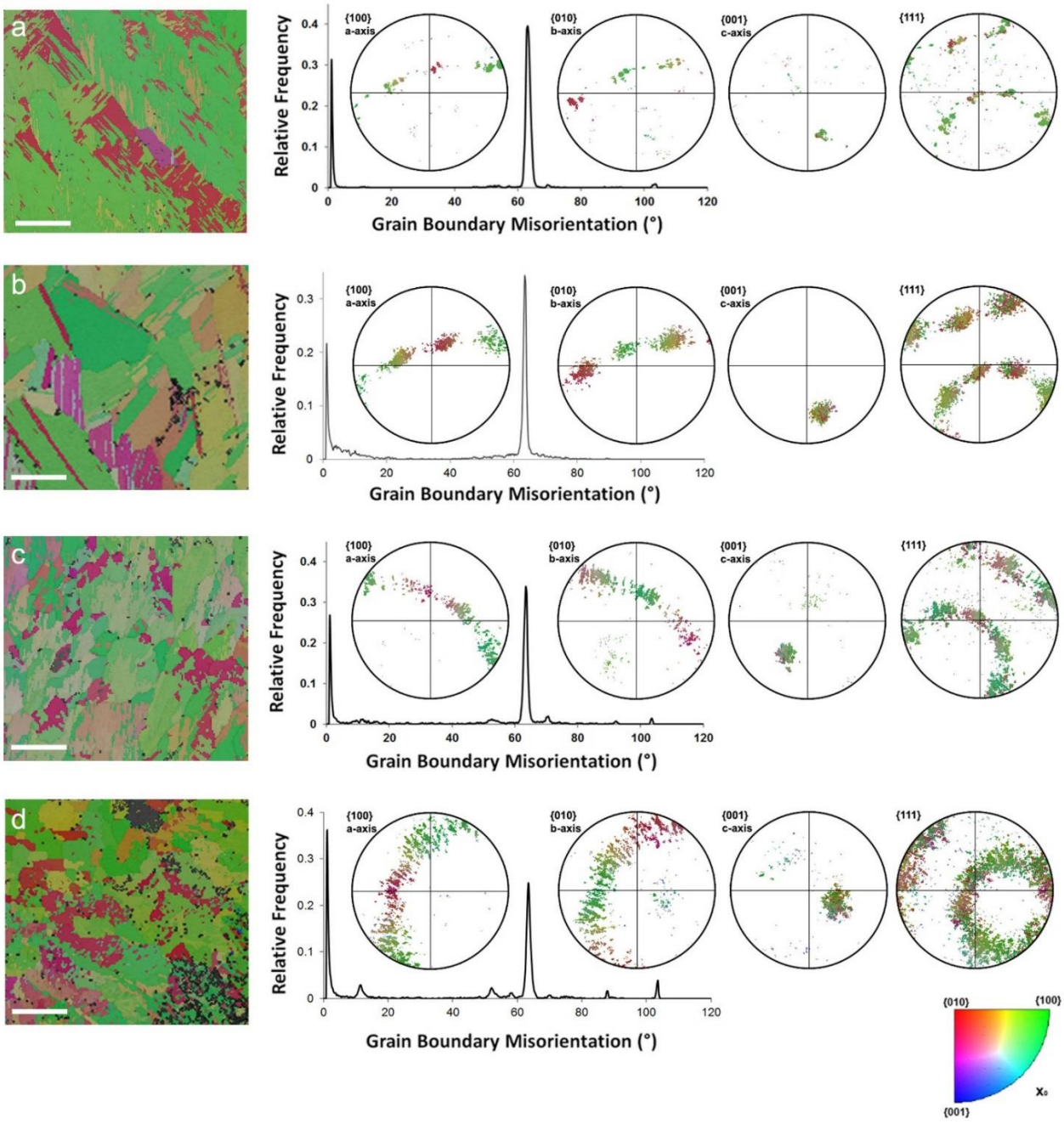

Figure 16: EBSD maps of all species, each taken on the sulcal side of the otolith, a) *L. calcarifer, b) P. bassensis, c) T. novaezelandiae, d) C. auratus.* Grain boundary misorientation and pole figures are given for each species. All exhibit the same orientation trends, though *C. auratus* shows less evident twinning of aragonite.

Raman Microspectroscopy

Raman spectra of the otolith (Figure 10) show the characteristic aragonite bands as well as bands originating from modes of the organic matrices. A spectrum collected on abiotic mineral aragonite for comparison shows a marked absence of the organic matrix bands (Figure 10). The major bands characteristic of otoliths are given in Table 1, though a comprehensive identification of Raman bands in otolith samples has been reported previously and so will not be reproduced here (Jolivet *et al.* 2008; Zhang *et al.* 2008). The bands characteristic of the insoluble organic matrix were identified by collection of Raman spectra on sectioned otoliths before and after etching of the soluble matrices. Orientation determination of the insoluble organic matrix was undertaken by examination of the carbonyl (C=O) stretch at 1707cm^{-1}. This band is not present in the mineral aragonite Raman spectra, indicating it belongs to the organic matrix and was still present following etching of the soluble matrix, indicating it belongs to the insoluble organic matrix. The band at 1707cm^{-1} has previously been reported in the Raman spectra of otoliths and was attributed by Jolivet to the organic matrix (Jolivet 2008). The carbonyl stretch at 1707cm^{-1} showed variation in intensity under polarisation, indicating that the scattering is influenced by the carbonyl group orientation.

Table 1: Major otolith Raman band attributions observed in this study, as given by Zhang et al. (2008) and Jolivet et al. (2008).

Wavenumber (cm^{-1})	**Band attribution (Jolivet *et al.* 2008; Zhang *et al.* 2008)**
702	Aragonite
851	δ(CCH) ring, ν(C–C), Tyr, Ac asp
1084	Aragonite
1461	Aragonite
1574	Aragonite
1707	ν(C=O) stretch, insoluble organic matrix
1813	ν(C=O) stretch, insoluble organic matrix

The intensity ratios R_X and R_Y, and the $<P_2>$ value calculated from the 1707cm^{-1} carbonyl stretch qualitatively defines the molecular orientation, with otoliths of all species having a calculated $<P_2>$ of approximately -0.5 (see Table 2), which defines perpendicular orientation with respect to the reference axis, in this case the aragonite c-axis. The orientation calculated is qualitative only, and serves only to confirm the observations of the insoluble organic matrix orientation in the SEM.

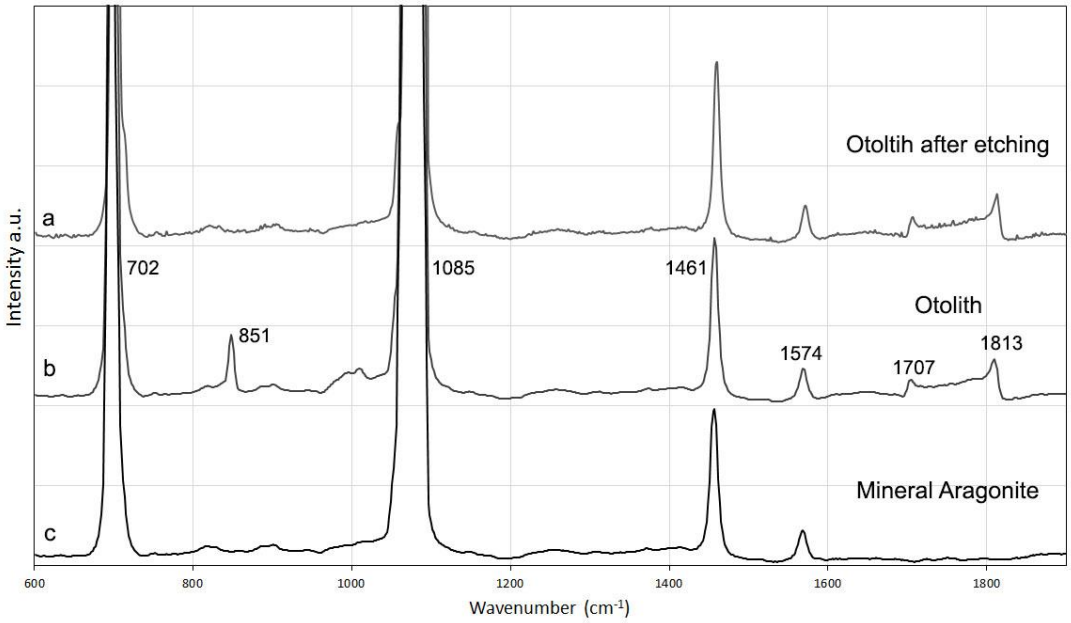

Figure 17: Raman spectra without polarisation of a) otolith after etching of the soluble matrix, b) otolith and c) mineral aragonite with the major Raman bands labelled.

Table 2: Raman intensities, ratios and calculated orientation parameter $<P_2>$ indicating the qualitative orientation of the insoluble organic matrix present in otoliths of each species, where a $<P_2>$ of -0.5 indicates perpendicular orientation relative to the reference axis.

Sample	**R_X**	**R_Y**	**$<P_2>$**
P. bassensis	0.49	1.55	-0.56
C. auratus	0.46	1.12	-0.65
L. calcarifer	0.37	1.25	-0.59
T.novaezelandiae	0.42	1.58	-0.58

Discussion

Otolith Mineral Polymorph

Both powder X-Ray Diffraction (XRD) and Electron Backscatter Diffraction (EBSD) confirmed the otoliths of the four marine species, *Platycephalus bassensis, Chrysophrys auratus, Trachurus novaezelandiae and Lates calcarifer* were all aragonitic. XRD provided a bulk analysis whilst EBSD allowed for small area high resolution analysis.

Otolith Growth and Habit

The presence of at least two distinct crystal habits in the otoliths of all species indicates that aragonite growth within the endolymph occurs under a changing set of conditions, as crystal habit is likely under kinetic control during growth. The acicular aragonite is dominant on the sulcal side of the otoliths of all species whilst the prismatic aragonite is found predominantly on the anti-sulcal side in three of the four species, with *P. bassensis* being the exception. The different habits are likely to be the result of different conditions within the endolymph, that is, the differential gradient of ion and protein concentration within the endolymph (Borelli 2001). The acicular habit is preferential at the sulcus where strong growth may be associated with the proximo-distally decreasing gradients of proteins and collagens (Borelli *et al.* 2001). Inversely the increasing proximo-distal gradient of proteoglycans may be limiting growth at the anti-sulcus, resulting in predominantly prismatic habits. However the possibility of an influence of the organic matrix over habit type cannot be ruled out at this stage.

The presence of only an acicular habit in *P. bassensis* may be due to the otoliths having been collected only from juvenile fish in the case of this species. The growth in the otoliths of juveniles is greater than that of mature fish, with growth rate slowing over time (Romanek and Gauldie 1996). A higher growth rate is expected to result in the presence of acicular habits in preference over a prismatic habit (Parmentier *et al.* 2007).

The presence of the same habits in the otoliths of four separate species indicates that there is a common mechanism of growth for these otoliths. Whether this is dependent

entirely on physico-chemical variations in the endolymph or whether it is influenced by the organic matrices remains to be seen.

The radial growth of aragonite in otoliths has already been described in numerous species and the aragonite growth axis has been highlighted in many biominerals previously (Lowenstam and Weiner 1989). The growth of aragonite in otoliths along the c-axis has been reported in only one species to date (Parmentier *et al.* 2007). Here we extend that to four other species, and postulate based on our observations that a common growth mechanism exists for otoliths across multiple species. There are of course likely to be exceptions however of the species studied here we observed a common mechanism.

Otolith Growth Orientation

Both the insoluble and soluble matrices were detected in the otoliths of all four species. The insoluble matrix left after etching is likely to be the collagen-like otolin-1 protein which has been extracted from otoliths previously (Murayama *et al.* 2002). The soluble organic matrix, observed here by absence as a dense network present within both the organic rich D-zones and the aragonite grains, or the L-zones, has been previously reported in otoliths and is described as an acidic, partially water soluble matrix. The D-zones are composed primarily of soluble organic matrices, however the insoluble matrix is also present as evidenced by this study (Figure 7). The L-zones have been shown previously by Raman spectroscopy to contain organic matrices as well as aragonite, though perhaps at a lower concentration than is present in the D-zone bands (Jolivet *et al.* 2008). In our study, the etching of the soluble organic matrices from within the aragonite grains in all species suggests this is a common growth mechanism across multiple species. The observation of the soluble organic matrix within the aragonite grains lends support to the proposal that the soluble matrices are responsible for directing otolith nucleation, growth and polymorph control, by providing binding sites for calcium carbonate nucleation and growth.

The insoluble organic matrix was observed in acid etched otoliths to bridge the gap left between the D-zones and the L-zones after removal of the soluble organic matrix. The

placement across the D-zone indicates that the insoluble matrix is involved in maintaining aragonite grain orientation across the organic rich D-zone. Experimental evidence has shown the soluble matrices do not exert control over aragonite orientation, and our observations indicate the soluble matrix is present as a network with no observable preferential alignment. Inversely we observe here for the first time that the insoluble matrix is aligned perpendicular with the otolith growth axis in all species. The perpendicular orientation was qualitatively confirmed by Raman microspectroscopy. The low concentration of organic matrices present within the otolith limited this study to qualitative evaluation of the orientation, as the signal intensity was not sufficient to warrant quantitative measurements. Improved signal intensity would allow for the calculation of a quantitative orientation distribution function.

EBSD mapping of the otolith aragonite shows that aragonite growth in all species occurred with the c-axis aligned parallel with the otolith growth axis. The a- and b- axes aligned perpendicular to the otolith growth axis, with rotation about the c-axis of approximately 60 degrees, due to aragonite twinning. The aragonite c-axis is therefore aligned perpendicular to the insoluble matrix growth in all species, suggesting that the aragonite c-axis orientation is constrained by the insoluble matrix. The inorganic matrix bridges the gap between the D-zones and the L-zones, allowing continuation of the aragonite grain growth with retained c-axis orientation. The aragonite a- and b-axes orientation however is constrained by the aragonite twinning.

The spatial relationship between the mineral and the organic matrices has the potential to provide information on nucleation of the mineral. A well-defined spatial relationship would suggest that nucleation occurs by epitaxy. Epitaxy is the orientated overgrowth of one crystalline phase on the face of another and occurs when the lattice arrangement in the template (the organic matrix) matches the lattice arrangement of the nucleating mineral (the aragonite) (Lowenstam and Weiner 1989). In the case of epitaxy the orientation of the mineral a-, b- and c-axes would all bear significant relationship to the matrix template structure. Such a relationship is not observed in otoliths, indicating growth is likely not epitaxial. Less controlled nucleation, such as that observed in this study, results in nucleation of the mineral upon the matrix template with well-defined

orientation of the aragonite c-axis perpendicular to the organic matrix template, however the a- and b-axes show no significant relation to the matrix template. Such a relationship has been defined in biomineral growth as stereochemically controlled nucleation (Weiner 1986), although cannot be strictly proven until more information is available on the molecular structure of the nucleation site itself. Stereochemically controlled nucleation occurs when the stereochemical requirements for a molecule to coordinate to a cation are met. The stereochemical requirements fix the nucleating mineral orientation in one direction, in this study perpendicular to the plane of the organic template matrix (Weiner 1986).

Implications for Otolith Applications

The consistency of the results across all species is encouraging for otolith applications as it indicates that the direction of grain orientation is common to multiple species. Whilst it cannot be said that the grain and matrix orientation has no influence over trace element uptake, it can be noted to be a negligible effect upon applications, as it occurs in a common manner in multiple species. Likewise the aragonite habit type varies consistently from the sulcus to the anti-sulcus in all species and so the effects on trace element uptake are expected to be seen as variation between sulcus and anti-sulcus, common to all species, rather than as species to species differences.

Conclusion

Otolith growth occurs with the aragonite grain orientation templated by the insoluble organic matrix, where the grain orientation is constrained in the aragonite c-axis by the perpendicularly aligned insoluble matrix. Aragonite grain orientation in the a- and b-axes however is dependent on the aragonite twinning, indicating mineral growth occurs via stereochemically controlled nucleation rather than epitaxially. Aragonite grain habit is consistent in all species, with the otolith dominated by acicular aragonite. The grain orientation appears to have little or no influence over trace element uptake, being controlled by the insoluble matrix. The aragonite habit varies from sulcus to anti-sulcus and being under kinetic control it is likely there are differences in trace element uptake in both regions, however the differences are consistent across the four species analysed.

Chapter 3

Quantitative electron microprobe mapping of otoliths suggests elemental incorporation is influenced by organic matrices: implications for the interpretation of otolith chemistry

Chapter content published partially in the Journal of Marine and Freshwater Research:

A. McFadden, B. Wade, C. Izzo, B.M.G. Gillanders, C.E. Lenehan, A. Pring, 2015, Quantitative electron microprobe mapping of otoliths suggests elemental incorporation is affected by organic matrices: implications for the interpretation of otolith chemistry, *Marine and Freshwater Research,* 2015, Online version, Vol 66, pp 1-10.

(Full article available in Appendix A).

Abstract

The distributions of strontium (Sr) and sulfur (S) in otoliths of a variety of marine species, *Platycephalus bassensis, Chrysophrys auratus, Trachurus novaezelandiae and Lates calcarifer,* were investigated in conjunction with otolith growth patterns in an effort to understand the mechanism of otolith mineralisation. Optimisation of quantitative elemental mapping by electron probe microanalysis (EPMA) achieved both high spatial resolution (<3 μm) and two dimensional visualisation of the fine scale Sr and S distributions in the otoliths with minimal damage. Results showed a correlation between Sr and S distributions in all species and a clear association with the otolith growth patterns determined by scanning electron microscopy (SEM). Further examination by laser ablation inductively coupled plasma mass spectrometry (LA-ICP-MS) showed that incorporation of Mg and Ba appear independent of both the S distribution and the growth patterns. The results suggest that element incorporation into the otolith is linked to the organic composition in the endolymph during mineralisation, and the organic matrices may in part assist the uptake of Sr. These findings may therefore have significant implications for the interpretation of otolith Sr chemistry.

Introduction

Otoliths are calcium carbonate structures mainly composed of calcium carbonate and organic matrices (<10%), which are involved in the maintenance of balance and hearing in the inner ear of teleost fish (Campana 1999; Carlstrom 1963; Degens *et al.* 1969). The predictable growth properties of otoliths and permanent uptake of trace elements from the environment is advantageous for a variety of ecological applications including age determination, stock identification, migration pathway reconstruction, and elucidation of environmental histories (Campana 1999; Elsdon *et al.* 2008). Otolith growth and composition are dependent on environmental factors such as water composition, temperature, and salinity, as well as biological factors including genetics, ontogeny, diet and elemental fractionation through biological transport (Barnes and Gillanders 2013; Reis-Santos *et al.* 2013; Woodcock *et al.* 2013).

Biomineralisation is highly regulated by organic macromolecules, which are usually negatively charged proteins containing carboxylate, sulfate, and phosphate functional groups (Addadi *et al.* 1987; Mann 1988). These groups are thought to bind Ca^{2+} ions, and could be involved in the control of crystal nucleation by lowering the energy of formation between the crystal and the organic substrate (De Yoreo and Vekilov 2003; Weiner 1986). Sulfur uptake in otoliths is well documented in the study of nutrient flows, migratory patterns and hypoxia (Limburg *et al.* 2015; Weber *et al.* 2002), but the role of sulfated macromolecules in biomineralisation is not well understood. In otoliths, it is thought that sulfate groups mainly occur in a class of proteins called proteoglycans (Addadi *et al.* 1987; Albeck *et al.* 1996). Evidence for the involvement of proteoglycans in biomineralisation is abundant across many biomineral types, including mollusc shells (Simkiss 1965), sea urchin spines (Wilt 1999), eggshells (Arias *et al.* 1992), and fish otoliths (Borelli *et al.* 2001). Inorganic experiments demonstrate the ability of various proteoglycans to stabilise nucleation and influence crystal size and orientation (Addadi *et al.* 1987; Addadi and Weiner 1985; Arias *et al.* 2004). To extract valuable information from the chemistry of otoliths it is therefore necessary to understand the mechanism of elemental uptake during organic mediated biomineralisation (Campana 1999; Kalish 1989).

Elemental incorporation in biominerals is not well understood, and whilst organic matrices determine the physical properties of biominerals and provide a template for formation (Addadi *et al.* 2006; Lowenstam and Weiner 1989; Weiner and Dove 2003), organic matrices may also exhibit affinities for minor and trace elements and preferentially facilitate or inhibit uptake. Based on shell microstructure and elemental composition, recent bivalve shell studies have suggested the possibility that Sr/Ca is not under environmental control (Foster *et al.* 2009; Poulain *et al.* 2015) but rather that Sr fractionation is mediated by sulfate rich organic macromolecules at the site of calcification (Schöne *et al.* 2013; Shirai *et al.* 2014). Studies of eel otoliths have indicated that excess glycosaminoglycans (GAGs), a component of proteoglycans, released during larval eel metamorphosis may influence Sr fractionation. The authors noted changes in the Sr/Ca ratios during metamorphosis that could not be accounted for by the surrounding ambient environmental conditions (Otake 1994; Tzeng 1996). The distribution of Sr within the otolith has been shown previously to be influenced by the formation of the seasonal translucent and opaque zones (Tomas *et al.* 2006; Toole *et al.* 1993). Despite these studies, to our knowledge the role that organic matrices play in the fractionation of minor and trace elements in otoliths has not been evaluated.

Elemental quantification within microstructural features (1-5 μm) of otoliths is limited by i) the spatial resolution of the commonly used techniques, ii) the sensitivity of the otolith structure to damage during analysis, and iii) the sensitivity of available techniques to the elements of interest. EPMA offers a significant improvement in spatial resolution as compared to LA-ICP-MS, and is a well-established technique for the evaluation of major and minor elements in otoliths (Gunn *et al.* 1992; Zimmerman and Nielsen 2003). However the sensitivity of the technique is generally limited for trace element applications due to the high beam current and long counting times required, in which significant damage and alteration can occur to the otoliths structure as the beam impacts on the sample at one point. Electron beam induced damage to the otolith surface includes pitting and compositional change, which affects its use as a quantitative technique. Alternate background collection methods in EPMA mapping have however made it possible to collect high spatial resolution quantitative compositional data. Traditionally, quantitative X-Ray mapping would require a first pass of the sample with

the diffracting crystals on elemental peak positions, and then a second pass of the sample with the diffracting crystals moved to an off-peak position for background determination. Quantitative X-Ray maps can now be collected in a single sweep through the use of the mean atomic number (MAN) background correction (Donovan and Tingle 1996). This method relies on the dependence of the X-Ray background continuum on mean atomic number of the sample, negating the need to measure the X-ray intensity at an off-peak position. The end result is a significant reduction to the acquisition time and the effect of beam damage in quantitative mapping. As mentioned previously, the detection limits of EPMA can also be a limiting factor in the measurement and quantification of trace elements. However more recent designs of large diffracting crystals, and the ability to aggregate X-ray intensities of signals from multiple spectrometers within the software make it possible to improve the sensitivity for elements close to the detection limit. To our knowledge, these methods have not been applied to beam sensitive otoliths, and facilitate the analysis of otolith microstructure with minimal damage.

This paper reports an optimised EPMA approach using mean atomic number background collection method for the two dimensional visualisation of elemental composition at high resolution (<3 µm). We hypothesise that otolith trace elements are fractionated during mineralisation in the endolymph and suggest that understanding this fractionation may reduce the assumptions inherent in interpretation of otolith chemistry. The objective of this study is to optimise quantitative EPMA mapping to investigate the relationship between otolith composition and growth patterns at a fine scale (<3 µm). We aim to evaluate the effect of the organic matrix on elemental fractionation in otolith biomineralisation for a variety of species to improve future interpretations of otolith chemistry in relation to ecological issues.

Methods

Sample Preparation

Sagittal otoliths were obtained from specimens of sand flathead (*Platycephalus bassensis*), snapper (*Chrysophrys auratus*), barramundi (*Lates calcarifer*) and mackerel

(*Trachurus novaezelandiae*). Upon removal otoliths were rinsed in ultrapure water to remove any adhering tissue, air dried in a laminar fume hood, and stored in microcentrifuge tubes for later examination. Otoliths were subsequently embedded in two part epoxy resin and sectioned through the core to expose the growth increments using a Buehler ISOMET low speed saw. Sectioned otoliths were polished on a Struers TegraPol mechanical polisher, with a graded series of lapping cloths starting with 9 µm, 3 µm and finishing on 0.04 µm colloidal silica. Between each polish, samples were cleaned ultrasonically and rinsed thoroughly in ultrapure water. Prior to scanning electron microscopy (SEM) and electron probe microanalysis (EPMA), the polished sections were carbon coated to avoid sample charging during analysis.

Scanning Electron Microscopy (SEM)

Scanning electron microscopy (SEM) was employed to visualise the growth patterns and grain microstructure of the otoliths, primarily by backscatter electron imaging (BSE). All images were acquired on a FEI Quanta 450 Field Emission Gun SEM (Eindhoven, Netherlands) operated at 20 kV.

Electron Probe Microanalysis (EPMA)

EPMA quantitative maps were acquired on a CAMECA SXFive microprobe (Paris, France). The instrument was equipped with five wavelength dispersive spectrometers (WDS), four of which have large diffracting crystals. Data were acquired and processed in the Probe for EPMA^{TM} software. Analytical conditions for spot analyses consisted of an accelerating voltage of 15 kV and a beam current of 20 nA, using beam diameters ranging between 2 and 20 µm. Elements analysed, peak/background positions, count times, standards, and elemental overlap corrections for spot analyses are summarised in the material available in Appendix A. Quantitative elemental maps were collected with a focused beam of 15 kV/100 nA, with pixel size and dwell time of 1 µm and 100 msec respectively. Oxygen and carbon content (weight percent, wt%) were calculated by stoichiometry. WDS signal aggregation was employed for S measurements to improve signal to noise ratio and detection limits. Mean atomic number (MAN) backgrounds were used for quantitative mapping to reduce damage to the beam

sensitive otoliths. Maps were processed in CalcImage™ and visualised in Surfer (Golden Software)™. The detection limits for Ca, Sr and S in EPMA maps were 500, 600 and 170 ppm respectively, calculated to assume detection at 3 times the background variance. The limits of quantification for Ca, Sr and S were subsequently calculated to be 1700, 1800 and 510 ppm respectively, calculated to assume quantification at 10 times the background variance.

EPMA Wavelength Dispersive Spectrometer Signal Aggregation

In otoliths the sulfur (S) concentration generally falls below 1000ppm. For EPMA spot analyses this is achievable with a beam diameter of the order of 20µm and a dwell time of 15s. For EPMA mapping however the beam diameter is limited to 1µm and the dwell time to 100ms, meaning the detection limits are inferior and the S concentration has the potential to fall below the detection limits. For this reason the effect of signal aggregation from multiple spectrometers was evaluated for the collection firstly of elemental maps and then secondarily of spot analyses.

To improve the signal to noise ratio and detection limits of the analysis of S, wavelength dispersive spectrometer (WDS) signal aggregation was employed using multiple LPET diffracting crystals. We evaluated the effect of signal aggregation on the S detection limits using first a single spectrometer, then two spectrometers in aggregation, three spectrometers and finally a maximum of five spectrometers in aggregation. The detection limits were calculated for each set of conditions and the optimum chosen for all mapping and spot analyses thereafter.

Due to the configuration of diffracting crystals in the 5 spectrometers, the aggregation of the S signal required a different setup for each condition tested. For the aggregation of two and three spectrometers the analysis required only a single pass of the electron beam, with all elements collected on the optimum diffracting crystal. The aggregation of five spectrometer signals required two passes of the electron beam across the sample and required Sr be collected with a PET diffracting crystal, rather than a TAP crystal which provides a greater Sr signal. In the case of the five spectrometer aggregation Sr

was analysed on four aggregated LPET crystals to overcome the lower signal achieved due to the use of PET crystals (Table 3).

Elemental maps on a test otolith, sample FH278, were collected using the three test conditions (Table 3) in order to assess the effect of signal aggregation using multiple spectrometers. The low concentration of S within the otoliths necessitates the use of spectrometer aggregation in order to improve the detection limits. Without signal aggregation, the detection limits for S mapping measured on a LPET crystal are on average 1050 ppm, which is higher than the average concentration of S in some otoliths. Due to the difference in spectrometer angle and type, the detection limits of each spectrometer are not equal and as such we report the average of each test condition (Table 4).

Table 3: Spectrometer configurations for the three test conditions assessing the effect of signal aggregation.

	Spectrometer Configuration				
Test Condition	**Spectro 1**	**Spectro 2**	**Spectro 3**	**Spectro 4**	**Spectro 5**
1 Two spectrometer signal aggregation	LTAP crystal Sr	TAP crystal Sr	LPET crystal Ca	LPET crystal S	LPET crystal S
2 Three spectrometer signal aggregation	LTAP crystal Sr	PET crystal Ca	LPET crystal S	LPET crystal S	LPET crystal S
3 Five spectrometer signal aggregation	LPET crystal S (1st pass) Sr (2nd pass)	PET crystal S (1st pass) Ca (2nd pass)	LPET crystal S (1st pass) Sr (2nd pass)	LPET crystal S (1st pass) Sr (2nd pass)	LPET crystal S (1st pass) Sr (2nd pass)

EPMA Repeated Spot Measurements

Repeated spot measurements at beam diameters of 2, 5, 7, 10 and 20 µm were collected on otolith material without moving the sample, in order to determine the degradation of the calcium carbonate over time and the optimum beam diameter for spot analysis and mapping. Three repeated measurements were taken at one location for each beam

diameter and the change in apparent Ca concentration recorded with each subsequent measurement.

EPMA Mean Atomic Number Backgrounds

The beam sensitive nature of otoliths prevents the collection of a second pass off-peak background acquisition for quantitative mapping, and as a result mean atomic number background (MAN) fits were assessed as an alternative for quantitative mapping of otoliths. A comparison of the accuracy and precision of elemental maps created using off-peak backgrounds versus those using MAN fit backgrounds was undertaken using mineral aragonite as a proxy for the otolith. The absolute numbers and errors were then compared to that of spot analysis on the aragonite. Aragonite was chosen as it is an ideal $CaCO_3$ mineral that is much less sensitive to beam damage than otoliths, removing this as a variable in the comparison.

Laser Ablation – Inductively Coupled Plasma Mass Spectrometry

LA-ICP-MS elemental analyses were performed on an Agilent 7700cx quadrupole ICP-MS (Agilent Technologies, Mulgrave, Victoria, Australia) coupled to a Resonetics M-50 Excimer Laser equipped with a Laurin Technic Cell (ACT, Australia). NIST 612 Standard Reference Material was used as the external standard, with the US Geological Survey calcium carbonate MACS-3 measured as a secondary standard. Spot analyses were undertaken adjacent to EPMA analyses at a pulse rate of 5Hz, fluence of approximately 3.5 $mJ\mu m^{-2}$, and spot diameters of 17 to 24 µm. All data were processed in Glitter™ and elemental concentrations were calculated by using the ^{43}Ca signal within each sample as an internal standard, which was previously quantified independently by EPMA. Elemental maps were collected using a pulse rate of 10 Hz, fluence of approximately 3.5 $mJ\mu m^{-2}$, 14 µm spot diameter and 14 μms^{-1} scan speed. Isotope dwell times were: ^{43}Ca 5 ms, ^{88}Sr 50 ms, ^{24}Mg 20 ms and ^{138}Ba 50 ms. All data were processed and output as elemental maps using the program Iolite™ developed by the Melbourne Isotope Group (Woodhead *et al.* 2007). The detection limits for Sr, Mg and Ba were calculated to be 59 ppm, 0.75 ppm and 0.15 ppm respectively, calculated to assume detection at 3 times the background variance. The limits of quantification for Sr, Mg and Ba were calculated

to be 199 ppm, 2.5 ppm and 0.5 ppm respectively, calculated to assume quantification at 10 times the background variance.

Results

Effect of Wavelength Dispersive Spectrometer Signal Aggregation in EPMA

Elemental S maps collected using test condition 1, aggregating the signal from 2 spectrometers, resulted in a S detection limit of 300ppm. By comparison elemental S maps using test condition 2, aggregating the signal from 3 spectrometers, gave detection limits for S of 170ppb. The detection limits calculated for test condition 3, aggregating the signal from 5 spectrometers, resulted in detection limits for S of 150ppb, demonstrating the superior detection limit possible with signal aggregation.

Table 4: Detection limits for Ca, Sr and S calculated under the three test conditions.

	Detection Limits		
Test Condition	**Ca (ppm)**	**Sr (ppm)**	**S (ppm)**
1 Signal aggregation of two spectrometers	580	550	300
2 Signal aggregation of three spectrometers	650	560	170
3 Signal aggregation of five spectrometers	510	500	150

The aggregation of the signal from 5 spectrometers did not show a significant enough improvement to negate the issues caused by analysing the sample surface in two passes. Due to the damage of the electron beam on the otolith surface during the first pass, the Sr and Ca quantitative results, collected on the second pass, become unreliable due to the loss of CO_2 from the aragonite structure. The Sr and Ca quantitative maps collected on the second pass visually show the damage caused (Figure 18). The resulting concentrations of Sr and Ca differed significantly from those collected in a single pass of the beam. Visualisation of the S distribution within the otolith was however greatly

improved with the aggregation of 5 spectrometers and so would be the recommended analysis method in cases where quantitative analysis is secondary to understanding the S distribution in otoliths.

The Ca detection limits calculated for test conditions 2 and 3 are higher than that of test condition 1 due to the spectrometer crystal used. Test condition 1 measured Ca on an LPET crystal which collects a greater signal than the PET crystal used in test conditions 2 and 3. Since Ca is present as a major element within otoliths, at approx. 38 wt%, the detection limits of all three conditions were deemed acceptable. The Sr detection limits for each test condition differed only slightly, however the spectrometer configuration utilised changed dramatically. For Sr analysis, test condition 1 utilised signal aggregation, whereas test condition 2 did not. The small difference in detection limit occurs because test condition 1 is aggregated on an LTAP and a TAP crystal, however the contribution to the signal from TAP is almost negligible next to the LTAP signal and the removal of TAP altogether does not impact the detection limit. Sr is present in greater concentration in otoliths than is seen for S and therefore the improvement in detection limit due to Sr signal aggregation was deemed insignificant compared to the improvement in S detection limits. Whilst test condition 3 utilised signal aggregation of four spectrometers for Sr, the use of LPET crystals results in a lower signal than obtained using LTAP crystals and therefore little improvement in detection limit was achieved despite the aggregation.

Based on these results, subsequent quantitative mapping on the otoliths of four species were conducted under test condition 2, using signal aggregation for S only and using only a single pass of the electron beam to avoid sample damage effects.

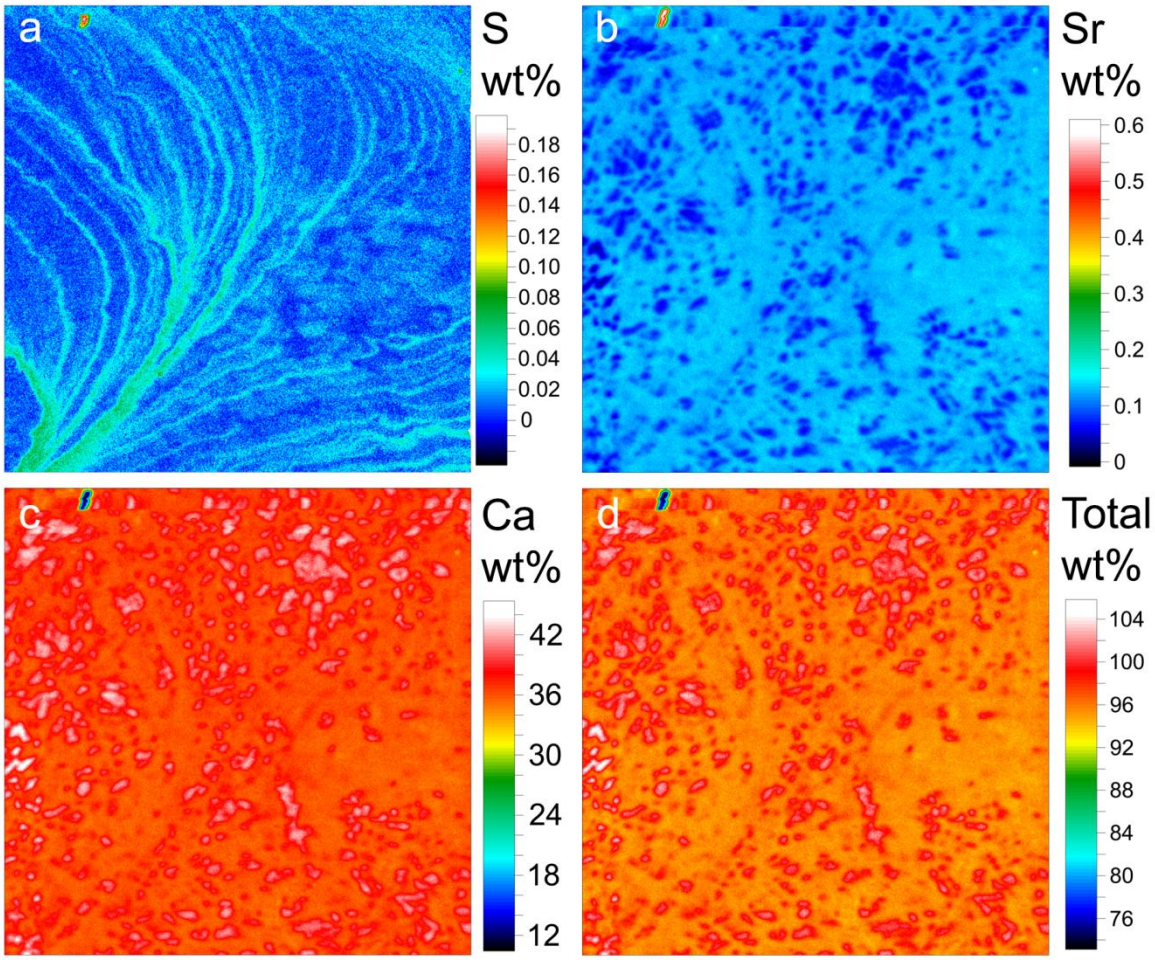

Figure 18: Elemental maps using 5 spectrometer aggregation of the S signal, a) S wt%, b) Sr wt%, c) Ca wt% and d) Total wt%. The S signal is vastly improved however the Sr and Ca quantitative results are unusable due to sample damage during the second beam pass. The damage to the sample surface is evident as area of increased Ca wt% and Total wt% in c) and d) due to the loss of CO_2 under the beam. The same areas have low Sr wt% as given in b). Image size 300µm x 300µm.

Effect of Repeated Measurements in EPMA

Repeated spot measurements at beam diameters of 2, 5, 7, 10 and 20 µm were collected on otolith material without moving the sample, in order to determine the degradation of the calcium carbonate over time (Figure 19). At small beam diameters (high beam power density) there was a significant increase in the apparent measured Ca wt% with repeated measures. Thus larger beam diameters are required to minimise damage to

the otolith during repeated measures. At small beam diameters, such as that required for mapping only a single measurement can be taken before beam damage increases the apparent Ca wt%. Traditional EPMA mapping using off peak background measurements requires multiple passes of the electron beam across the sample and will therefore result in erroneous concentrations on otolith samples.

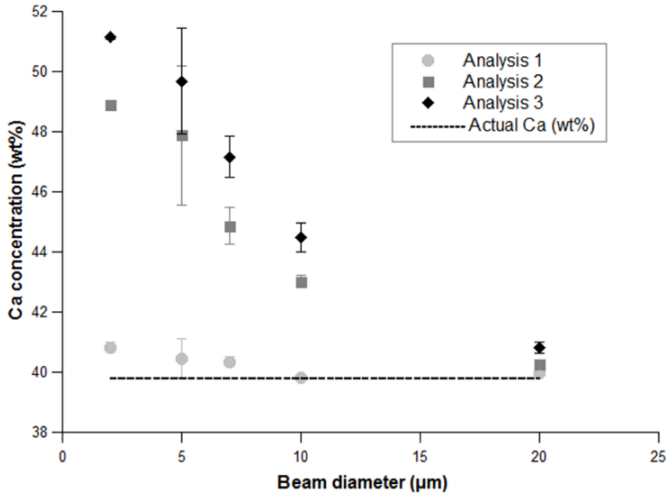

Figure 19: Effect of repeated measurements on the otolith Ca concentration, indirectly showing the loss of CO_2 due to electron beam damage through the increase in apparent Ca concentration (wt%).

Effect of Mean Atomic Number Backgrounds in EPMA

The beam sensitive nature of otoliths prevents the collection of a second pass off-peak background acquisition for quantitative mapping, and as a result mean atomic number background (MAN) fits were assessed as an alternative for quantitative mapping of otoliths. A comparison of the accuracy and precision of elemental maps created using off-peak backgrounds versus those using MAN fit backgrounds was undertaken using mineral aragonite as a proxy for the otolith. The absolute numbers and errors were then compared to that of spot analysis on the aragonite. Aragonite was chosen as it is an ideal $CaCO_3$ mineral that is much less sensitive to beam damage than otoliths, removing this as a variable in the comparison. The bulk concentrations of Ca, Sr and S for aragonite (taken as an average of the concentrations from each pixel within a 300x300 µm map)

determined by both off-peak and MAN background methods are shown in Table 5. Both methods gave virtually identical results, however the MAN approach required only one irradiation rather than the two used by off-peak background measurements, thus significantly reducing the likelihood of damage to the otoliths. The levels of Ca and Sr detected within the aragonite using both methods are typical of those of otoliths, and both are detectable at errors of less than 5%. Absolute values are also comparable to those determined by more accurate spot analyses (Table 5). In aragonite, S is present at lower levels (approx. 100 ppm) than is expected from the otoliths (approx. 500 ppm) and so errors are expected to be marginally improved for real otolith samples.

Table 5: Aragonite mineral maps of bulk composition, comparing the EPMA traditional off-peak background method to mean atomic number background (MAN) method and to spot analyses results. Bulk concentrations for the maps were calculated by averaging every pixel in a 300x300 µm map. Spot analyses of bulk concentrations are the average of 20 individual measurements, collected at 20 µm beam diameter.

	Ca (wt%)	Sr (ppm)	S (ppm)	Total (wt%)
Off peak	40.92	2000	100	101.06
Background	±0.63	±600	±100	± 0.69
MAN fit	40.93	2000	100	101.13
Background	±0.63	±500	±200	± 0.69
Spot	40.25	2030	60	100.39
Analyses	± 0.11	± 60	±7	± 0.12

Otolith Growth Patterns and Microstructure

In addition to that observed in Chapter 2 sectioned otoliths of all four species exhibit the typical alternating paired opaque D-zone bands (areas rich in organic material) and translucent L-zone bands (areas rich in calcium carbonate). D-zone bands were clearly

visible on the anti-sulcal side in otoliths of all species, though the thinner daily growth bands on the sulcal side were not always distinct.

On the sulcal side, where the bulk of otolith growth occurs, the D-zone bands were thinner and the L-zone bands were more defined. Toward the anti-sulcus, grain size and L-zone band width was compressed, whereas the D-zone bands were broader, possibly due to a lower degree of calcification away from the sensory epithelium.

Otolith Elemental Distribution by EPMA

Strontium and S were distributed heterogeneously across the two otolith samples analysed in all species (Figure 20, 21). The average and maximum Sr and S concentrations were calculated for each species using the quantitative maps (Table 6). In all otoliths the highest concentrations of both Sr and S occurred at the D-zone bands as compared to the intervening L-zone bands (Figure 21 and Table 6).

In all species the distribution of Sr and S showed a correlation with the D-zone (organic rich) bands. The growth bands on the anti-sulcal side were well resolved by EPMA mapping in all species, however the spatial resolution of the technique did not allow for adequate resolution of the much smaller growth bands on the sulcal side.

In the case of *Chrysophrys auratus* the growth bands were not well defined in the otoliths and the elemental maps for S showed distinct thin growth bands while the Sr maps showed a merging of bands, making it difficult to distinguish the D- and L-zones in the Sr map (Figure 21 j-l). The D-zone bands which exhibited the highest Sr concentration were correlated with the S maps, however the finer D-zone bands could not be distinguished.

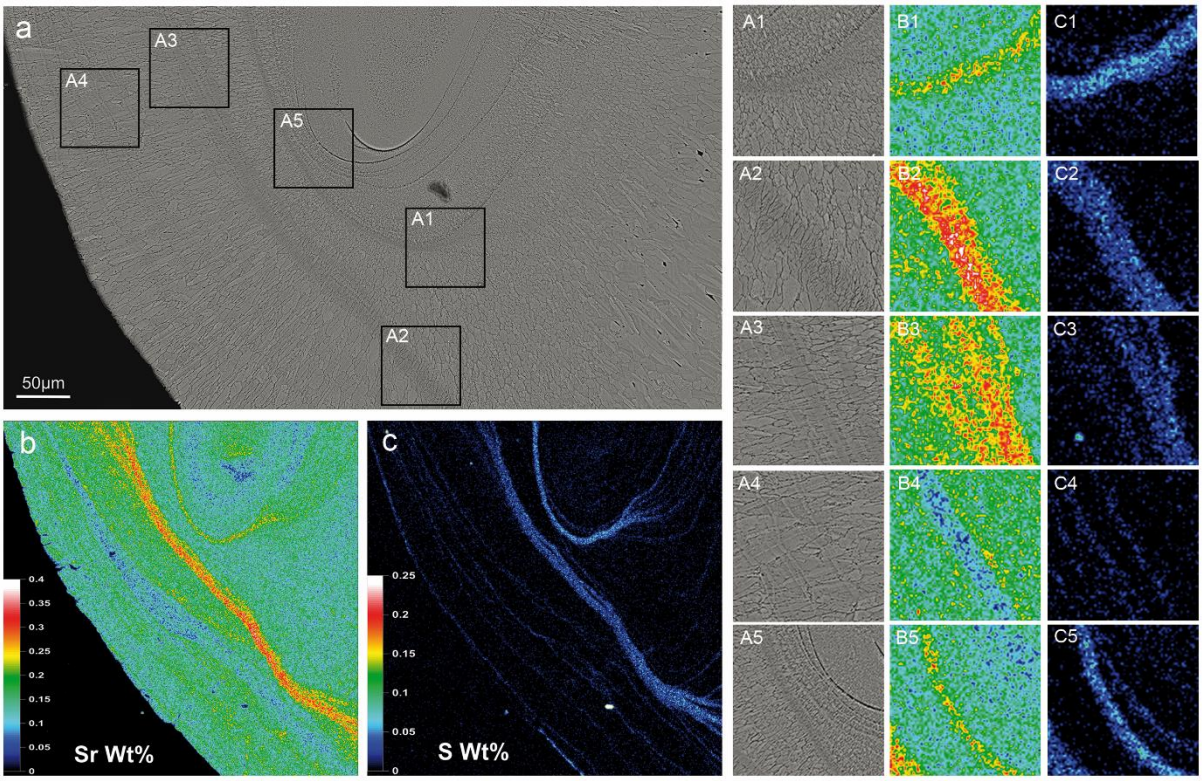

Figure 20: (a) Growth patterns of the core of sample FH278, typical for *Platycephalus bassensis*. Compared with the L-zone bands, the D-zone bands are characteristically darker in the scanning electron microscope backscatter electron imaging (BSE) images. (b, c) Electron probe microanalysis (EPMA) elemental maps showing the distribution of Sr (b) and S (c) across sample FH278, with concentration variations illustrated by the colour scale shown at the bottom left of each map. Higher-magnification images of the otolith growth patterns (A1–A5) and the elemental maps for Sr (B1–B5) and S (C1–C5) highlight the relationship between Sr, S and the growth patterns.

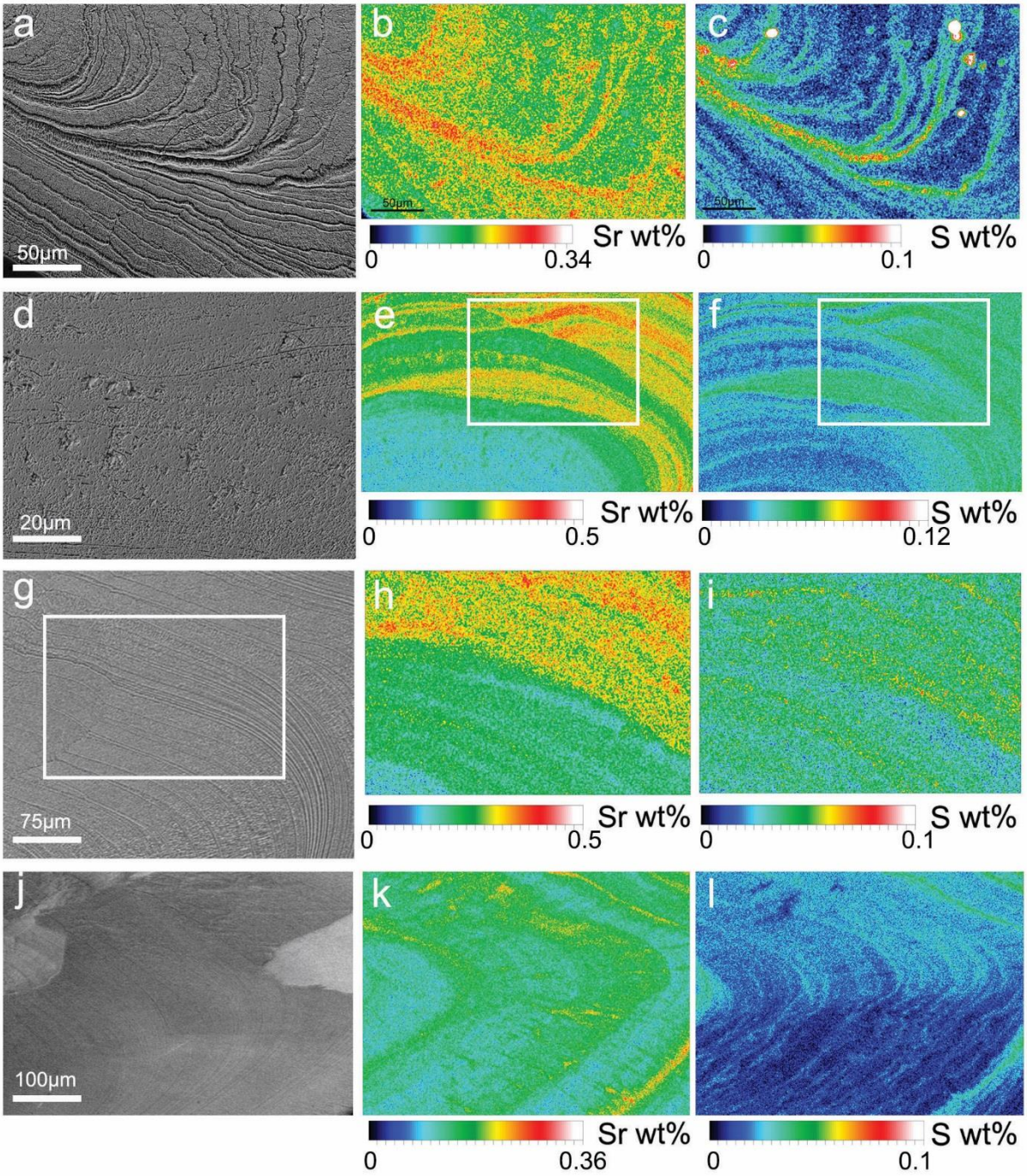

Figure 21: Elemental maps of all four species and the corresponding backscatter electron images, a) *P. bassensis* BSE image showing the growth patterns, b) corresponding Sr wt% EPMA map and c) S wt% EPMA map. d) *T. novaezelandiae* BSE image showing the growth patterns, e) corresponding Sr wt% EPMA map and f) S wt% EPMA map. g) *L. calcarifer* BSE image showing the growth patterns, h) corresponding Sr wt% EPMA map and i) S wt% EPMA map. j) *C. auratus* BSE image showing the growth

patterns, k) corresponding Sr wt% EPMA map and l) S wt% EPMA map. Areas marked in white indicate the magnified image in the corresponding elemental maps.

Table 6: Sr and S concentrations as calculated from entire otolith EPMA maps. Average concentration and maximum concentrations (± 95% confidence interval) calculated from two otolith maps for each species.

Species	Sr Average Concentration (ppm)	Sr Maximum Concentration (ppm)	S Average Concentration (ppm)	S Maximum Concentration (ppm)
Platycephalus bassensis	1700 ± 280	3600 ± 300	215 ± 50	1400 ± 75
Chrysophrys auratus	1350 ± 240	3600 ± 210	225 ± 35	1000 ± 50
Trachurus novaezelandiae	2650 ± 170	4200 ± 180	360 ± 20	1100 ± 40
Lates calcarifer	2350 ± 190	5600 ± 200	350 ± 40	1000 ± 65

Table 7: Sr concentration in the D-zone (organic rich) and L-zone (mineral rich) bands, calculated from the otolith EPMA maps and showing the average difference in concentration as a percent.

Species	D-zone bands Sr concentration (ppm)	L-zone band Sr concentration (ppm)	% Difference
Platycephalus bassensis	2300	1350	41
Chrysophrys auratus	2850	2000	30
Trachurus novaezelandiae	2700	1800	33
Lates calcarifer	2600	1550	41

Detection limits and Limits of Quantification by EPMA

On otoliths of all species, the concentrations of both Sr and S in the D-zone bands were at a maximum and were above the detection limit. The concentration of S in the L-zone bands however fell below the detection limits (below 170ppm). The Sr concentration in the D-zone bands is above the limits of quantification (above 1800ppm), however the Sr concentration in the L-zone bands falls just on the limit of quantification. The S concentration in the D-zone bands is above the limit of quantification (above 510ppm), however the S concentration in the L-zone bands falls below on the limit of quantification.

Otolith Elemental Distribution by LAICPMS

For each species an LA-ICP-MS map was collected to evaluate the distribution of Sr, Mg and Ba within the otolith. The resolution of the ICPMS was limited by the large spot diameter however and the fine scale growth bands could not be resolved. Instead the larger scale seasonal banding was evident. LA-ICP-MS maps of the otoliths seasonal translucent and opaque banding reveal that the distribution of Mg and Ba did not exhibit the same correlation with the otolith growth patterns, or the S distribution as was seen for Sr (Figure 22).

As they fell close to the limit of quantification obtained from mapping, Sr concentrations were also evaluated by LA-ICP-MS and EPMA spot analyses for *Platycephalus bassensis*. The average Sr concentrations were evaluated in four samples of *Platycephalus bassensis* via LA-ICP-MS using a 17 µm spot diameter, giving 2230 ppm ± 250 ppm at 95% confidence. EPMA spot analyses conducted again on four samples with a 20 µm beam diameter, gave average Sr concentrations 2020 ppm ± 200 ppm at 95% confidence as compared to the average Sr by EPMA mapping with a 1 µm beam diameter of 1720 ppm ± 290 ppm at 95% confidence. The results for all other species are expected to follow the same trend.

Table 8: Average Mg and Ba concentration and standard error (ppm) as determined by LA-ICP-MS.

Species	Mg Average Concentration (ppm)	Standard Error (ppm)	Ba Average Concentration (ppm)	Standard Error (ppm)
Platycephalus bassensis	9.1	1.1	1.3	0.19
Chrysophrys auratus	28.3	1.2	4.9	0.18
Trachurus novaezelandiae	12.3	0.8	35.7	5.8
Lates calcarifer	32	4.1	109	27

In otoliths of *T. novaezelandiae* the average Mg concentration was 12.3 ± 0.8 ppm at 95% confidence and the average Ba concentration was 35.7 ± 5.8 ppm at 95% confidence. The Mg concentration is elevated in the otolith core and broad, diffuse bands are discernible. The Ba distribution shows a steady increase outwards from the core, with thin bands visible in the outer half of the otolith, following the banding visible in the Sr map (Figure 22).

The average Mg concentration in otoliths of *P. bassensis* was 9.1 ppm ± 1.1 ppm at 95% confidence, and the average Ba concentration was 1.3 ppm ± 0.19 ppm at 95% confidence. The Mg distribution was largely inverse to that of Sr, with increased concentrations in the otolith core, and in diffuse bands where Sr levels were the lowest. The distribution of Ba showed some concentrated bands in common with Sr, though the thin bands of high concentration were inadequately resolved and could not be linked to growth pattern changes (Figure 23 g-i)).

In otoliths of *C. auratus* the average Mg concentration was 28.3 ppm ± 1.2 ppm at 95% confidence and the average Ba concentration was 4.9 ppm ± 0.18 ppm at 95% confidence. Again the Mg distribution shows a high concentration in the otolith core, and appears inverse to the Sr concentration with broad diffuse bands visible. The Ba distribution largely follows the Sr distribution, however the Ba map shows a greater number of thinner bands as compared to the Sr map (Figure 23 a-c).

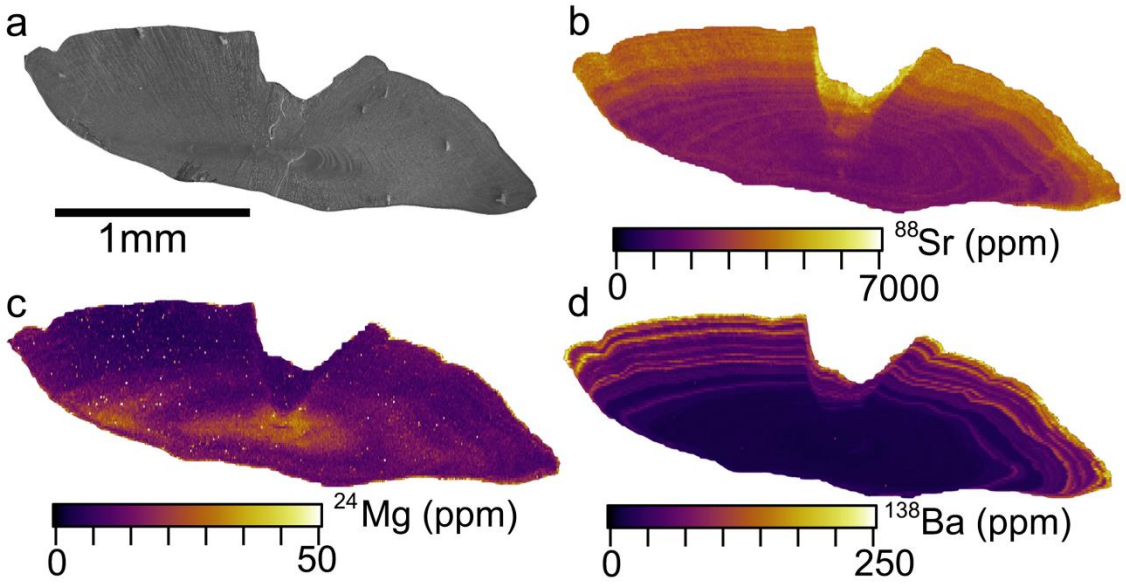

Figure 22: LA-ICP-MS elemental maps on *T. novaezelandiae* showing the distribution of Mg, Ba and Sr. a) Otolith SEM backscatter electron image, b) Sr distribution (ppm), c) Mg distribution (ppm) and d) Ba distribution (ppm).

In otoliths of *L. calcarifer* the average Mg concentration was 32 ± 4.1 ppm at 95% confidence and the average Ba concentration was 109 ± 27 ppm at 95% confidence. The Mg is elevated in the otolith core and broad, diffuse bands are visible, largely inverse in concentration to the Sr map. The Ba concentration in *L. calcarifer* is much higher than is seen for the other species and does not show the same growth banding as the others. Instead the otolith core is elevated in Ba and drops rapidly at a distinct point in time (Figure 23 d-f).

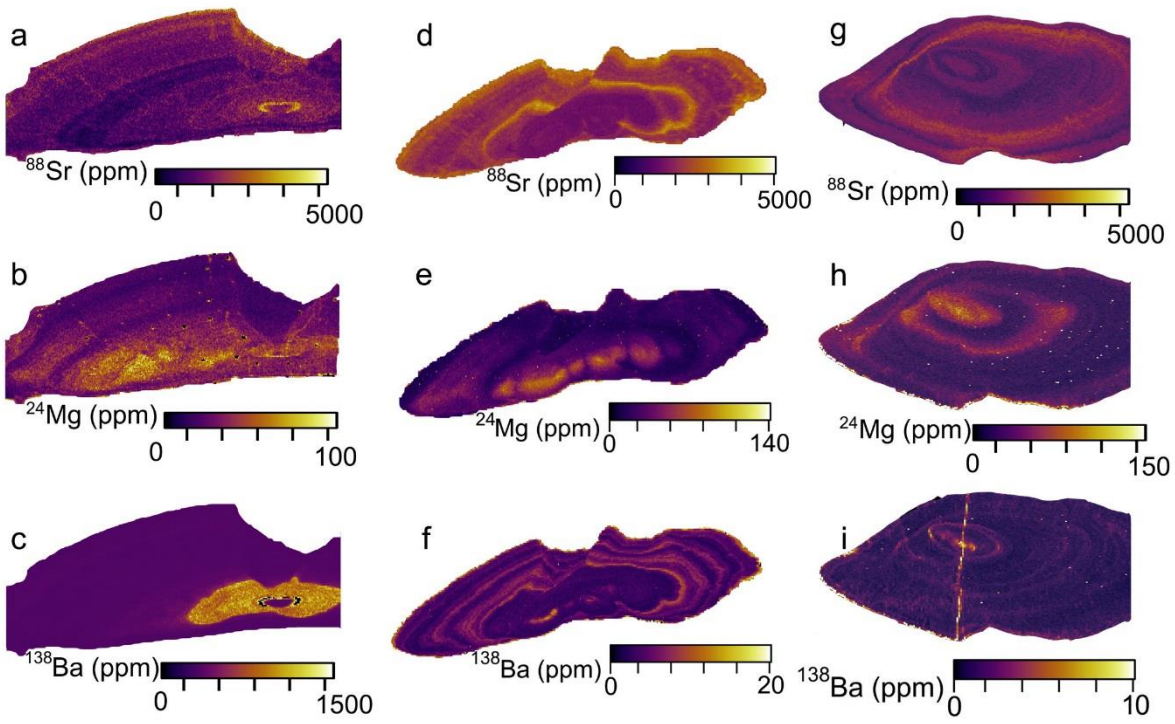

Figure 23: LA-ICP-MS elemental maps on otoliths showing the distribution of Mg, Ba and Sr. a-c) *Chrysophrys auratus* otolith elemental maps, Sr, Mg and Ba respectively, d-f) *Lates calcarifer* otolith elemental maps, Sr, Mg and Ba respectively, g-i) *Platycephalus bassensis* otolith elemental maps, Sr, Mg and Ba respectively.

Discussion

Optimisation of EPMA Mapping

EPMA mapping was optimised for quantification of Sr and S to take advantage of the high spatial resolution (<3 µm) provided by the technique. One of the major limitations of quantitative mapping by EPMA is the damage caused by the electron beam on sensitive materials such as otoliths. This damage is due to the decomposition of the aragonite structure and subsequent loss of CO_2 under the beam, and is particularly problematic for repeated measurements (Gunn *et al.* 1992; Zimmerman and Nielsen 2003). As beam diameter increased however, beam power density ($\mu W \mu m^{-2}$) was reduced due to beam spread across a larger area and consequently CO_2 loss also decreased. Otolith analysis should utilise a beam power density of <3 $\mu W \mu m^{-2}$, as noted by Gunn et al., (1992), which we found corresponded to a beam diameter of 20 µm. We observed significant changes in elemental quantification with repeated measurements, suggesting that accurate quantitative analyses requires a reduction in beam time and the elimination of repeated measurements (but see Zimmerman et al., 2003 who found contrasting results). To circumvent the problem of damage at small beam diameters and the need for repeated measures during quantitative mapping, mean atomic number (MAN) backgrounds were assessed as an alternative to traditional off-peak background measurements to reduce beam time on the sample.

Traditional off-peak background collection requires two sweeps of the electron beam across the sample, which is unacceptable for elemental quantification of otoliths. Unlike off-peak backgrounds, MAN backgrounds are calculated from the dependence of the X-ray background continuum on mean atomic number. By measuring and curve fitting the background X-ray intensities at the analytical peak in standards that do not contain any of the analyte or interfering elements, the acquisition time and the effect of beam damage is significantly reduced (Donovan and Tingle 1996).

Quantitative elemental mapping at spatial resolutions close to the size of the otolith growth features allows for a better understanding of the relationship between the growth pattern and composition. Coarser sampling by LA-ICP-MS and EPMA spot analyses demonstrate the effect of averaging across the growth patterns, whereby the

extreme values can be under or overestimated due to sampling at resolutions larger than the growth features. The effect of signal averaging at coarse spatial resolution has been investigated in mollusc shells, where there was a pronounced reduction in peak height of the highest concentrations across the growth lines (Shirai *et al.* 2014). The effect of averaging was largely overcome in our study by EPMA mapping as the features of interest, the D and L zones, were larger than or equal in size to the beam diameter. Averaging is particularly problematic in relation of the growth patterns in otoliths and should always be considered with care in the interpretation of chronological profiles.

Otolith Composition and Structure

The association between the distribution of Sr and S, and the otolith growth patterns indicates that the incorporation of Sr is influenced by the biomineralisation process in the otoliths for all four species analysed. The role of biological processes in trace element partitioning have been previously reported (Campana 1999; Kalish 1989) and the effect of the elemental pathways and barriers between the water and the otolith are summarised by Campana (1999). Whilst the influence of partitioning on physiologically important elements such as Na, P, K and Cl is significant and unpredictable (Campana 1999), the effect on many trace elements is more subtle (Kalish 1989) and is often considered negligible when it closely reflects the elemental composition of the water. Based on observations of the present study and the assumption that the changing growth pattern and S distribution reflect the organic composition at the site of mineralisation, we suggest that the organic matrices in the endolymph partially facilitate the uptake of Sr and influence the overall otolith composition. Recent reports from mollusc shell studies support this interpretation, as the Sr/Ca and S/Ca ratios exhibit a distinct relationship with the shell microstructure (Foster *et al.* 2009; Schöne *et al.* 2013; Shirai *et al.* 2014). The consistency of results across the species analysed suggests that this mechanism is widespread among marine species.

Role of the Organic Matrix

Based upon the correlation of S with the D-zone bands, S is assumed to be incorporated in the otolith as a component of the organic matrix, not as inorganic sulfate. Studies of aragonitic mollusc shells support this assumption in which S mainly exists as sulfate within polysaccharides and proteoglycans, whereas a smaller fraction is included as amino acids (Cuif *et al.* 2003; Dauphin *et al.* 2005). Neither $CaSO_4$ nor $SrSO_4$ have been reported in otoliths, however some mollusc shell studies have reported the presence of inorganic sulfate (Siriprom *et al.* 2011; Yoshimura *et al.* 2013). Though not undertaken on otoliths, chemical speciation studies on a variety of biominerals including mollusc shells and corals indicate that S exists mainly as a component of the organic matrix (Cuif *et al.* 2003; Lowenstam and Weiner 1989). The function of sulfated macromolecules in biominerals has not been established, but it is proposed that organic sulfate contained within the crystal grains plays a role in nucleation, whereas organic sulfate between the grains is responsible for controlling properties such as size and shape (Addadi *et al.* 2006; Arias *et al.* 2004).

The organic macromolecules most likely responsible for the high S concentrations at the growth bands are sulfated proteoglycans, which have been observed in the endolymph and extracted from otoliths (Arias *et al.* 2004; Borelli *et al.* 2001; Payan *et al.* 1997). The role of proteoglycans in otolith biomineralisation has not been established, but their anionic properties have led to the suggestion of a role in concentrating Ca^{2+} ions at the endolymph-crystal interface (Borelli *et al.* 2001). Borelli et al. (2001) observed an increasing proximo-distal gradient of proteoglycans in the endolymphs of *Oncorhychus mykiss* and *Psetta maxima*, whereas proteins, collagens and amino acids exhibited a decreasing proximo-distal gradient. It was suggested that there may be a relationship between the endolymph gradient and the otolith growth axes, notably that the strong growth at the sulcus may be associated with the proximo-distally decreasing gradients of proteins and collagens (Borelli *et al.* 2001). Inversely the increasing proximo-distal gradient of proteoglycans may be limiting growth at the anti-sulcus by binding free cations in the endolymphatic fluid (Payan *et al.* 2002). At the anti-sulcal side where grain size is smaller, the appearance of broader D-zone bands in all species supports the notion of growth inhibiting action by S rich organic matrices. The growth pattern

correlation with Sr would also suggest such organic macromolecules exhibit a high cation binding affinity, perhaps leading to an enhanced Sr incorporation, predominantly at the anti-sulcus. However, the fine scale microstructure on the sulcal side is not adequately resolved by EPMA mapping in any species to determine whether such observations are exclusive to the anti-sulcus, or are equivalent on the sulcal side at a finer, unresolved scale.

Otolith Chemistry

The differences in distribution of Sr, Mg and Ba throughout the otoliths may be a result of environmental changes, but may also be explained in part by the differences in the site occupied by each element in the aragonite structure. High energy X-ray absorption studies have revealed that Sr is randomly substituted for Ca in the aragonite structure of otoliths (Doubleday *et al.* 2014). The relationship between Sr and the S rich organic matrices is therefore unlikely to be a result of direct binding of the organic matrix to Sr, but rather a result of organic mediated fractionation during mineralisation. It is predicted that most of the discrimination against Sr incorporation occurs during crystallisation rather than during Sr uptake from the water, due to the similarity in the water-otolith and endolymph-otolith partition coefficients (Campana 1999). Using our results the water-otolith partition coefficient (D_{Sr}) is calculated to be on average 0.21 assuming an average seawater Sr/Ca of 8.9 mmol/mol. This is comparable to estimates of other studies and to the calculated endolymph-otolith D_{Sr} of 0.25 (Kalish 1989). It is however unclear whether the Sr fractionation is related to the presence of S rich proteoglycans due to the limits of detection and spatial resolution constraints of EPMA mapping. Sr and S are shown to correlate at the D-zone bands where concentrations are the highest, but the S concentrations fall below the detection limits within the L-zone bands. Current observations point towards the facilitation of Sr uptake by the S rich organic matrices, however it is unclear whether these observations are exclusive to the D-zone bands, or extend throughout the otolith structure at concentrations below the detection limits of EPMA.

Mg is present in otoliths at concentrations too low to evaluate its bonding mode, however mollusc shell studies show Mg to be hosted by the organic component as a

disordered phase in biogenic aragonite (Foster *et al.* 2008). The high concentration of Mg observed in the otolith core by LA-ICP-MS mapping supports this possibility in otoliths as well, although it also indicates that the organic matrix involved in otolith nucleation and initial growth may not be the S rich organic matrix observed by proxy in this study. Sulfur rich proteoglycans are not known to be involved in the nucleation process, but rather are implicated in the inhibition of crystal growth in specific stereochemical directions (Addadi *et al.* 1987). Mg is more likely to be bound by a component of the organic matrix involved in nucleation, rather than have uptake facilitated as in the case of Sr.

The host site of Ba within otoliths has not been evaluated, though it is predicted to occupy sites analogous to those of Sr (Dietzel *et al.* 2004; Pingitore 1986). Due to the larger ionic radius of Ba (1.47 Å) when compared to that of Ca (1.18 Å) substitution of Ba for Ca is more limited than that of Sr. Due to the increase in crystal defects with greater Sr uptake (Pingitore 1986), uptake of Ba may be facilitated by Sr in waters of high Sr/Ca (de Vries *et al.* 2005). However based on our LA-ICP-MS maps Ba is not influenced by the organic matrix or the Sr concentration, which may be due to a low Sr/Ca ratio for our samples (1-3 mmol/mol), below that needed to facilitate Ba uptake (>4 mmol/mol) (de Vries *et al.* 2005). Despite this, it cannot be ruled out that a relationship exists at a spatial resolution below that achieved by LA-ICP-MS mapping.

Implications for Otolith Chemistry Interpretation

The correlation of Sr with both S and the otolith growth patterns may have implications for the interpretation of otolith chemistry, however there are still ambiguities to be addressed before such implications can be fully understood. Our study highlights that Sr and S are linked in the D-zone bands, and suggests that S rich organic matrices play a role in Sr incorporation, possibly by concentrating Sr at the site of mineralisation. However, the detection limits of EPMA limit our understanding of the relationship across the entire otolith. If Sr and S are correlated within the L-zone bands as well as the D-zone bands then it is possible that S rich organics are responsible for the fractionation of Sr between the endolymph and otolith. The observed variation in Sr in that case would therefore be directly related to ambient water concentration. However, if the

correlation is only present within the organic rich D-zone bands then the observed Sr variation at the bands may be a result of the concentration of the organic matrices in the endolymph, rather than the ambient water concentration. The distinction is one of importance in regard to implications for otolith chemistry interpretations, however a definitive answer currently remains below the spatial resolution and detection limits of the available techniques.

Conclusion

Utilising MAN background fits and signal aggregation, high resolution, two dimensional elemental mapping of otoliths by EPMA reveal a relationship between the Sr and S distribution and the otolith growth patterns, giving insight into the role of biomineralisation in otolith elemental incorporation in a variety of species. Under the assumption that S is present as a component of the organic matrix, we suggest that Sr uptake is mediated by organic macromolecules in the endolymph, with S rich organic matrix components such as proteoglycans likely candidates in the facilitation. Without direct measurement of the organic matrices it is not possible to conclude with certainty however recent findings in mollusc shells support the suggestion of an organic mediated Sr uptake in biogenic systems. Further studies are needed to investigate the extent of the relationship across the otoliths at lower detection limits to fully understand the implications of biomineralisation on otolith chemistry interpretations. Further investigations into the organic matrix at a fine scale will also improve our understanding of elemental uptake in biogenic systems such as otoliths.

Chapter 4

Conclusion and Future Directions

Introduction

The aim of this project was to uncover the physical regulation of the otolith biomineralisation process in order to begin reducing the assumptions inherent in the current interpretation of otolith chemistry. The characterisation of otoliths of four species addressed two inter-dependent aims centred around gaining insight into the otolith biomineralisation mechanism and its influence on elemental uptake. Assessment of the distribution of trace elements incorporated into the growing otolith structure and the structural relationship between the crystalline and organic components of otoliths has led to an improved understanding of otolith biomineralisation and its role in trace element uptake.

Chapter two examined the otolith structure and explored the relationship between the crystalline aragonite structure and the underlying organic matrix template with a view to assess whether otolith growth control varied between species or a common mechanism exists. The thorough examination of the otolith structure provided insights into the mechanism of biomineralisation and a context for subsequent elemental analysis.

Chapter three optimised the analysis of low level minor elements by electron probe microanalysis in order to investigate the distribution of minor and trace elements in the otoliths of marine species and explore the relationship between elemental distribution and the otolith structure. Specifically this study characterised the distribution of ecologically important elements, including Sr, S, Mg and Ba, and their relationship to the microstructure examined in Chapter 2 to assess the impact of the biomineralisation process on the occlusion of elements into the otolith structure.

Discussion

The thorough characterisation of four species of otoliths at the microstructural level in this study yielded information about the otolith biomineralisation process and its role in trace element incorporation.

The spatial relationship between the mineral and the organic matrices in otoliths provided insight to the process of aragonite nucleation. The relationship between the mineral and the insoluble organic component observed in this study is not constrained strictly enough to indicate epitaxial growth. The aragonite c-axis is aligned perpendicular to the organic matrix template, however the a- and b-axes show no significant relation to the matrix template and are determined instead by the aragonite twinning. Such a relationship has been defined in biomineral growth as stereochemically controlled nucleation (Weiner 1986). The stereochemical requirements fix the nucleating mineral orientation in one direction, in this study perpendicular to the plane of the organic template matrix (Weiner 1986).

The presence of the same crystal habits of aragonite in the otoliths of four separate species indicates that there is a common mechanism of growth for these otoliths. Aragonite grain habit is consistent in all species, with the otolith dominated by acicular aragonite. The dominance of the acicular aragonite habit on the sulcal side is predicted here to be a result of the differential gradient of ion and protein concentration within the endolymph (Borelli 2001). The strong growth at the sulcus may be associated with the higher Ca^{2+} concentration and the lower protein concentration in that region of the endolymph.

The endolymph composition is also seen to play a role in the uptake of trace elements, specifically the Sr and S incorporation. The organic macromolecules most likely responsible for the high S concentrations at the growth bands are sulfated proteoglycans, whose role in otolith biomineralisation has not been established, but their anionic properties have led to the suggestion of a role in concentrating Ca^{2+} ions at the endolymph-crystal interface (Borelli *et al.* 2001). It was suggested that there may be a relationship between the endolymph concentration gradient and the otolith growth axes, notably that the strong growth at the sulcus may be associated with the

proximo-distally decreasing gradients of proteins and collagens (Borelli *et al.* 2001). Inversely the increasing proximo-distal gradient of proteoglycans may be limiting growth at the anti-sulcus by binding free cations in the endolymphatic fluid (Payan *et al.* 2002). At the anti-sulcal side where grain size is smaller, and the crystal habit is predominantly prismatic, the appearance of broader D-zone bands in all species supports the notion of growth inhibiting action by S rich organic matrices in this region. The growth pattern correlation with Sr also suggests such organic macromolecules exhibit a high cation binding affinity, perhaps leading to an enhanced Sr incorporation, predominantly at the anti-sulcus.

The correlation of Sr with both S and the otolith growth patterns may have implications for the interpretation of otolith chemistry, however there are still ambiguities to be addressed before such implications can be fully understood. Our study highlights that Sr and S are linked in the D-zone bands, and suggests that S rich soluble organic matrices play a role in Sr incorporation, possibly by concentrating Sr at the site of mineralisation. Under the assumption that S is present as a component of the organic matrix, we suggest that Sr uptake is mediated by organic macromolecules in the endolymph, with S rich organic matrix components such as proteoglycans likely candidates in the facilitation. Without direct measurement of the organic matrices it is not possible to conclude with certainty however recent findings in mollusc shells support the suggestion of an organic mediated Sr uptake in biogenic systems.

The trace elements Mg and Ba in the otoliths of all species, showed no correlation with the organic growth bands or the S distribution. The mode of binding of each trace element is expected to have an impact on the elemental uptake, with neither Mg or Ba being as favourable as the uptake of Sr. Sr was the only element evaluated which was shown have uptake influenced by the organic matrices and the biomineralisation process.

The consistency of the results across all species is encouraging for otolith applications as it indicates that the direction of grain orientation and the influence of the organic matrix over Sr uptake is common to multiple species. Whilst it cannot be said that the grain and matrix orientation has no influence over trace element uptake, it can be noted to be a negligible effect upon applications, as it occurs in a common manner in multiple

species. Likewise the aragonite habit type varies consistently from the sulcus to the anti-sulcus in all species and so the effects on trace element uptake are expected to be seen as variation between sulcus and anti-sulcus, common to all species, rather than as species to species differences. The correlation of Sr with both S and the otolith growth patterns may have implications for the interpretation of otolith chemistry, however there are still ambiguities to be addressed before such implications can be fully understood.

Future Directions

Further research into otolith biomineralisation is required to understand the mechanism at work. While the elemental composition is remarkably well characterised, there is a lack of understanding about the organic matrices themselves and their relationship to the mineral. This lack arises partially from the difficulty in studying the matrix. Going forward, further inquiry into the organic matrix composition and its relationship to the mineral will be vital to elucidating the mechanism of biomineralisation.

Raman microspectrometry may provide further insights to the relationship between the organic and the mineral, however as with all the techniques utilised in this study, greater spatial resolution and detection limits are needed.

A deeper investigation of the otolith protein composition and structure will be required to confirm the mechanism of growth and understand the chemistry of the binding between the mineral and organic components. One possible avenue of research include the use of synchrotron radiation in protein crystallography and elemental analysis.

Conclusion

Although the biomineralisation process in otolith formation is often considered negligible in the interpretation of otolith chemistry, which is widely applied to answer questions of ecological significance, it is vital to understand and the accurate interpretation of otolith data relies upon it. The reconstruction of fish migration

pathways, stock identification, age validations and elucidation of environmental histories are all dependent upon separating environmentally regulated processes from biologically regulated processes such as the biomineralisation of the otolith itself.

As outlined in Chapter 1, the primary aim of this study was to investigate the relationship between the microstructure and the chemistry of otoliths of four marine fish species, to gain insight into the biomineralisation mechanism and its influence on elemental uptake. Much of the challenge in studying otolith biomineralisation is the inaccessibility of the bone, and in examining the micro and nano-scale interactions of mineral and organic components without loss of context. This chapter summarises some of the key contributions of this thesis towards overcoming such challenges and discusses possible directions of inquiry for future work.

Chapter 2 investigated for the first time both the orientation of the mineral aragonite and the organic matrix in otoliths. It was shown that the aragonite aligns with the c-axis parallel to the otolith growth axis in all species, and the a- and b-axes aligned perpendicular to the otolith growth axis with rotation about the c-axis of approximately 60 degrees due to aragonite twinning. The otolith insoluble organic matrix was observed by SEM and its orientation qualitatively evaluated by Raman spectroscopy for the first time, showing that the matrix aligned perpendicular to the aragonite c-axis and the otolith growth axis. The results indicate that a spatial relationship exists between the otolith aragonite crystallographic axes and the insoluble organic matrix, indicating that the aragonite mineral growth is directed upon a matrix template. This initial study also suggests that Raman may be a powerful tool in further investigating the molecular order and composition of the otolith organic matrix in future studies.

Chapter 3 examined the minor and trace element composition of otoliths, and the relationship between elemental distribution and structure. Optimisation of the EPMA analysis of otolith structures provided a method for quantitative mapping of minor elements at high spatial resolution, therefore allowing correlation to the microstructure. The correlation between the distribution of Sr, S and the organic matrix in all species suggests that the incorporation of Sr may be in part assisted by the organic matrices. The distributions of Mg and Ba, though analysed at much lower spatial resolution by LA-ICPMS, were seen to be independent from the organic matrix. The

results may have significant implications for the interpretation of otolith chemistry however further investigations are still needed.

References

Addadi, L., Moradian, J., Shay, E., Maroudas, N.G., and Weiner, S. (1987) A chemical model for the cooperation of sulfates and carboxylates in calcite crystal nucleation: Relevance to biomineralization. *Proceedings of the National Academy of Sciences* **84**(9), 2732-2736.

Addadi, L., and Weiner, S. (1985) Interactions between acidic proteins and crystals - stereochemical requirements in biomineralization. *Proceedings of the National Academy of Sciences of the United States of America* **82**(12), 4110-4114.

Addadi, L., Joester, D., Nudelman, F., and Weiner, S. (2006) Mollusk shell formation: a source of new concepts for understanding biomineralization processes. *Chemistry – A European Journal* **12**(4), 980-987.

Albeck, S., Weiner, S., and Addadi, L. (1996) Polysaccharides of intracrystalline glycoproteins modulate calcite crystal growth in vitro. *Chemistry-a European Journal* **2**(3), 278-284.

Alvarez, A., Morales-Nin, B., Palmer, M., Tomas, J., and Sastre, J. (2008) A two-dimension otolith growth inverse model. *Journal of Fish Biology* **72**(3), 512-522.

Arias, J.L., Carrino, D.A., Fernandez, M.S., Rodriguez, J.P., Dennis, J.E., and Caplan, A.I. (1992) Partial biochemical and immunochemical characterization of avian eggshell extracellular matrices. *Archives of Biochemistry and Biophysics* **298**(1), 293-302.

Arias, J.L., Neira-Carrillo, A., Arias, J.I., Escobar, C., Bodero, M., David, M., and Fernandez, M.S. (2004) Sulfated polymers in biological mineralization: a plausible source for bio-inspired engineering. *Journal of Materials Chemistry* **14**(14), 2154-2160.

Barnes, T.C., and Gillanders, B.M. (2013) Combined effects of extrinsic and intrinsic factors on otolith chemistry: implications for environmental reconstructions. *Canadian Journal of Fisheries and Aquatic Sciences* **70**(8), 1159-1166.

Battey, M.H., and Pring, A. (1997) 'Mineralogy for students.' (Addison-Wesley Longman)

Bloss, F.D. (1971) 'Crystallography and crystal chemistry.' (Holt, Rinehart and Winston Inc. : New York and London)

Borelli, G., Guibbohni, M.E., Mayer-Gostan, N., Priouzeau, F., De Pontual, H., Allemand, D., Puverel, S., Tambutte, E., and Payan, P. (2003) Daily variations of endolymph composition: relationship with the otolith calcification process in trout. *Journal of Experimental Biology* **206**(15), 2685-2692.

Borelli, G., Mayer-Gostan, N., De Pontual, H., Boeuf, G., and Payan, P. (2001) Biochemical relationships between endolymph and otolith matrix in the trout (*Oncorhynchus mykiss*) and turbot (*Psetta maxima*). *Calcified Tissue International* **69**(6), 356-364.

Bower, D.I. (1972) Investigation of molecular orientation distributions by polarised raman scattering and polarized fluorescence. *Journal of Polymer Science Part B-Polymer Physics* **10**(11), 2135-2153.

Britannnica (2016) Aragonite. (Encyclopedia Britannica: http://www.britannica.com/science/aragonite)

Brown, R., and Severin, K.P. (1999) Elemental distribution within polymorphic inconnu (Stenodus leucichthys) otoliths is affected by crystal structure. *Canadian Journal of Fisheries and Aquatic Sciences* **56**(10), 1898-1903.

Campana, S.E. (1997) Use of radiocarbon from nuclear fallout as a dated marker in the otoliths of haddock Melanogrammus aeglefinus. *Marine Ecology Progress Series* **150**(1-3), 49-56.

Campana, S.E. (1999) Chemistry and composition of fish otoliths: pathways, mechanisms and applications. *Marine Ecology Progress Series* **188**, 263-297.

Carlstrom, D.D. (1963) Crystallographic study of vertebrate otoliths. *Biological Bulletin* **125**(3), 441-&.

Checa, A.G., Mutvei, H., Osuna-Mascaró, A.J., Bonarski, J.T., Faryna, M., Berent, K., Pina, C.M., Rousseau, M., and Macías-Sánchez, E. (2013) Crystallographic control on the substructure of nacre tablets. *Journal of Structural Biology* **183**(3), 368-376.

Cuif, J.-P., Dauphin, Y., Doucet, J., Salome, M., and Susini, J. (2003) XANES mapping of organic sulfate in three scleractinian coral skeletons. *Geochimica et Cosmochimica Acta* **67**(1), 75-83.

Dauphin, Y., Cuif, J.-P., Salomé, M., and Susini, J. (2005) Speciation and distribution of sulfur in a mollusk shell as revealed by in situ maps using X-ray absorption near-edge structure (XANES) spectroscopy at the S K-edge. *American Mineralogist* **90**(11-12), 1748-1758.

de Vries, M.C., Gillanders, B.M., and Elsdon, T.S. (2005) Facilitation of barium uptake into fish otoliths: Influence of strontium concentration and salinity. *Geochimica et Cosmochimica Acta* **69**(16), 4061-4072.

De Yoreo, J.J., and Vekilov, P.G. (2003) Principles of Crystal Nucleation and Growth. *Reviews in Mineralogy and Geochemistry* **54**(1), 57-93.

Degens, E.T., Deuser, W.G., and Haedrich, R.L. (1969) Molecular structure and composition of fish otoliths. *Marine Biology* **2**(2), 105-&.

DeVilliers, J.P.R. (1971) Crystal structures of aragonite, strontianite and witherite. *The American Mineralogist* **56**(May-June), 758-768.

Dietzel, M., Gussone, N., and Eisenhauer, A. (2004) Co-precipitation of Sr2+ and Ba2+ with aragonite by membrane diffusion of CO2 between 10 and 50 °C. *Chemical Geology* **203**(1–2), 139-151.

Donovan, J.J., and Tingle, T.N. (1996) An improved mean atomic number background correction for quantitative microanalysis. *Microscopy and Microanalysis* **2**(01), 1-7.

Doubleday, Z.A., Harris, H.H., Izzo, C., and Gillanders, B.M. (2014) Strontium randomly substituting for calcium in fish otolith aragonite. *Analytical Chemistry* **86**(1), 865-869.

Dove, S.G., Gillanders, B.M., and Kingsford, M.J. (1996) An investigation of chronological differences in the deposition of trace metals in the otoliths of two temperate reef fishes. *Journal of Experimental Marine Biology and Ecology* **205**(1-2), 15-33.

Elsdon, T.S., Wells, B.K., Campana, S.E., Gillanders, B.M., Jones, C.M., Limburg, K.E., Secor, D.H., Thorrold, S.R., and Walther, B.D. (2008) Otolith chemistry to describe movements and life-history parameters of fishes: Hypotheses, assumptions, limitations and inferences. In Oceanography and Marine Biology: An Annual Review, Vol 46. Vol. 46. (Eds. RN Gibson, RJA Atkinson and JDM Gordon) pp. 297-+. (Crc Press-Taylor & Francis Group: Boca Raton)

Engler, O., and Randle, V. (2009) 'Introduction to Texture Analysis: Macrotexture, Microtexture, and Orientation Mapping, Second Edition.' (CRC Press)

Falini, G., Albeck, S., Weiner, S., and Addadi, L. (1996) Control of aragonite or calcite polymorphism by mollusk shell macromolecules. *Science* **271**(5245), 67-69.

Falini, G., Fermani, S., Vanzo, S., Miletic, M., and Zaffino, G. (2005) Influence on the formation of aragonite or vaterite by otolith macromolecules. *European Journal of Inorganic Chemistry*(1), 162-167.

Foster, L.C., Allison, N., Finch, A.A., and Andersson, C. (2009) Strontium distribution in the shell of the aragonite bivalve *Arctica islandica*. *Geochemistry, Geophysics, Geosystems* **10**(3), Q03003.

Foster, L.C., Finch, A.A., Allison, N., Andersson, C., and Clarke, L.J. (2008) Mg in aragonitic bivalve shells: Seasonal variations and mode of incorporation in *Arctica islandica*. *Chemical Geology* **254**(1–2), 113-119.

Gallahar, N.K., and Kingsford, M.J. (1996) Factors influencing Sr/Ca ratios in otoliths of Girella elevata: an experimental investigation. *Journal of Fish Biology* **48**(2), 174-186.

Gauldie, R.W. (1988) Function, form and time-keeping properties of fish otoliths. *Comparative Biochemistry and Physiology Part A: Physiology* **91**(2), 395-402.

Gauldie, R.W., and Nelson, D.G.A. (1988) Aragonite twinning and neuroprotein secretion are the cause of daily growth rings in fish otoliths. *Comparative Biochemistry and Physiology Part A: Physiology* **90**(3), 501-509.

Griesshaber, E., Ubhi, H.S., and Schmahl, W.W. (2012) Nanometer scale microstructure and microtexture of biological materials revealed by high spatial resolution (15 to 5 kV) EBSD. In Textures of Materials, Pts 1 and 2. Vol. 702-703. (Eds. A Tewari, S Suwas, D Srivastava, I Samajdar and A Haldar) pp. 924-927.

Gunn, J.S., Harrowfield, I.R., Proctor, C.H., and Thresher, R.E. (1992) Electron probe microanalysis of fish otoliths — evaluation of techniques for studying age and stock discrimination. *Journal of Experimental Marine Biology and Ecology* **158**(1), 1-36.

Hasse, B., Ehrenberg, H., Marxen, J.C., Becker, W., and Epple, M. (2000) Calcium carbonate modifications in the mineralized shell of the freshwater snail Biomphalaria glabrata. *Chemistry-a European Journal* **6**(20), 3679-3685.

Jolivet, A., Bardeau, J.-F., Fablet, R., Paulet, Y.-M., and Pontual, H. (2008) Understanding otolith biomineralization processes: new insights into microscale spatial distribution of organic and mineral fractions from Raman microspectrometry. *Analytical and Bioanalytical Chemistry* **392**(3), 551-560.

Kalish, J.M. (1989) Otolith microchemistry - Validation of the effects of physiology, age and environment on otolith composition. *Journal of Experimental Marine Biology and Ecology* **132**(3), 151-178.

Kalish, J.M. (1991) Determinants of otolith chemistry - seasonal variation in the composition of blood plasma, endolymph and otoliths of bearded rock cod *Pseudophycis Barbartus*. *Marine Ecology Progress Series* **74**(2-3), 137-159.

Kalish, J.M. (1992) Formation of a stress-induced chemical check in fish otoliths. *Journal of Experimental Marine Biology and Ecology* **162**(2), 265-277.

Karney, G.B., Butler, P.G., Speller, S., Scourse, J.D., Richardson, C.A., Schröder, M., Hughes, G.M., Czernuszka, J.T., and Grovenor, C.R.M. (2012) Characterizing the microstructure of Arctica islandica shells using NanoSIMS and EBSD. *Geochemistry, Geophysics, Geosystems* **13**(4)

Kavanagh, A.M., Rayment, T., and Price, T.J. (1990) Inhibitor effects on calcite growth at low supersaturations. *Journal of the Chemical Society-Faraday Transactions* **86**(6), 965-972.

Lefevre, T., Rousseau, M.-E., and Pezolet, M. (2007) Protein secondary structure and orientation in silk as revealed by Raman spectromicroscopy. *Biophysical Journal* **92**(8), 2885-2895.

Limburg, and E., K. (1995) Otolith strontium traces environmental history of subyearling American shad *Alosa sapidissima*. *Marine Ecology Progress Series* **119**, 25-35.

Limburg, K.E., Walther, B.D., Lu, Z., Jackman, G., Mohan, J., Walther, Y., Nissling, A., Weber, P.K., and Schmitt, A.K. (2015) In search of the dead zone: Use of otoliths for tracking fish exposure to hypoxia. *Journal of Marine Systems* **141**, 167-178.

Lowenstam, H.A., and Weiner, S. (1989) 'On Biomineralization.' (Oxford University Press, USA)

Mann, S. (1988) Molecular recognition in biomineralization. *Nature* **332**(6160), 119-124.

Martin, G.B., Thorrold, S.R., and Jones, C.M. (2004) Temperature and salinity effects on strontium incorporation in otoliths of larval spot (*Leiostomus xanthurus*). *Canadian Journal of Fisheries & Aquatic Sciences* **61**(1), 34-42.

Melancon, S., Fryer, B.J., Ludsin, S.A., Gagnon, J.E., and Yang, Z. (2005) Effects of crystal structure on the uptake of metals by lake trout (*Salvelinus namaycush*) otoliths. *Canadian Journal of Fisheries and Aquatic Sciences* **62**(11), 2609-2619.

Mukai, H., Saruwatari, K., Nagasawa, H., and Kogure, T. (2010) Aragonite twinning in gastropod nacre. *Journal of Crystal Growth* **312**(20), 3014-3019.

Murayama, E., Takagi, Y., Ohira, T., Davis, J.G., Greene, M.I., and Nagasawa, H. (2002) Fish otolith contains a unique structural protein, otolin-1. *European Journal of Biochemistry* **269**(2), 688-696.

Murayama, E., Herbomel, P., Kawakami, A., Takeda, H., and Nagasawa, H. (2005) Otolith matrix proteins OMP-1 and Otolin-1 are necessary for normal otolith growth and their correct anchoring onto the sensory maculae. *Mechanisms of Development* **122**(6), 791-803.

Otake, T. (1994) Drastic changes in otolith strontium/calcium ratios in leptocephali and glass eels of Japanese eel *Anguilia japonica. Marine Ecology Progress Series* **112**, 189-193.

Pannella, G. (1971) Fish otoliths - Daily growth layers and periodical patterns. *Science* **173**(4002), 1124-&.

Parmentier, E., Cloots, R., Warin, R., and Henrist, C. (2007) Otolith crystals (in *Carapidae*): Growth and habit. *Journal of Structural Biology* **159**(3), 462-473.

Payan, P., Borelli, G., Priouzeau, F., De Pontual, H., Boeuf, G., and Mayer-Gostan, N. (2002) Otolith growth in trout *Oncorhynchus mykiss*: supply of Ca2+ and Sr2+ to the saccular endolymph. *Journal of Experimental Biology* **205**(17), 2687-2695.

Payan, P., Kossmann, H., Watrin, A., Mayer-Gostan, N., and Boeuf, G. (1997) Ionic composition of endolymph in teleosts: origin and importance of endolymph alkalinity. *Journal of Experimental Biology* **200**(13), 1905-12.

Pingitore, N.E. (1986) Modes of coprecipitation of Ba2+ and Sr2+ with calcite *Acs Symposium Series* **323**, 574-586.

Poulain, C., Gillikin, D.P., Thebault, J., Munaron, J.M., Bohn, M., Robert, R., Paulet, Y.-M., and Lorrain, A. (2015) An evaluation of Mg/Ca, Sr/Ca, and Ba/Ca ratios as environmental proxies in aragonite bivalve shells. *Chemical Geology* **396**, 42-50.

Radtke, R., Townsend, D., Folsom, S., and Morrison, M. (1990) Strontium:calium concentration ratios in otoliths of herring larvae as indicators of environmental histories. *Environmental Biology of Fishes* **27**(1), 51-61.

Radtke, R.L., Showers, W., Moksness, E., and Lenz, P. (1996) Environmental information stored in otoliths: Insights from stable isotopes. *Marine Biology* **127**(1), 161-170.

Raghavan, M. (2011) Investigation of mineral and collagen organization in bone using Raman spectroscopy. University of Michigan

Reis-Santos, P., Tanner, S.E., Elsdon, T.S., Cabral, H.N., and Gillanders, B.M. (2013) Effects of temperature, salinity and water composition on otolith elemental incorporation of *Dicentrarchus labrax*. *Journal of Experimental Marine Biology and Ecology* **446**, 245-252.

Ren, D., Ma, Y., Li, Z., Gao, Y., and Feng, Q. (2011) Hierarchical structure of asteriscus and in vitro mineralization on asteriscus substrate. *Journal of Crystal Growth* **325**(1), 46-51.

Romanek, C.S., and Gauldie, R.W. (1996) A predictive model of otolith growth in fish based on the chemistry of the endolymph. *Comparative Biochemistry and Physiology a-Physiology* **114**(1), 71-79.

Rousseau, M.E., Lefevre, T., Beaulieu, L., Asakura, T., and Pezolet, M. (2004) Study of protein conformation and orientation in silkworm and spider silk fibers using Raman microspectroscopy. *Biomacromolecules* **5**(6), 2247-2257.

Schöne, B.R., Radermacher, P., Zhang, Z., and Jacob, D.E. (2013) Crystal fabrics and element impurities (Sr/Ca, Mg/Ca, and Ba/Ca) in shells of *Arctica islandica*—Implications for paleoclimate reconstructions. *Palaeogeography, Palaeoclimatology, Palaeoecology* **373**(0), 50-59.

Schulz-Mirbach, T., Gotz, A., Griesshaber, E., Plath, M., and Schmahl, W.W. (2013) Texture and nano-scale internal microstructure of otoliths in the *Atlantic molly, Poecilia mexicana*: A high-resolution EBSD study. *Micron* **51**, 60-69.

Shirai, K., Schöne, B.R., Miyaji, T., Radarmacher, P., Krause Jr, R.A., and Tanabe, K. (2014) Assessment of the mechanism of elemental incorporation into bivalve shells (*Arctica islandica*) based on elemental distribution at the microstructural scale. *Geochimica et Cosmochimica Acta* **126**(0), 307-320.

Simkiss, K. (1965) Organic matric of oyster shell. *Comparative Biochemistry and Physiology* **16**(4), 427-&.

Siriprom, W., Kaewkhao, J., Phachana, K., and Limsuwan, P. (2011) Crystal Structure and Morphology Dependence of the Phase of Mollusc Shell: A Case Study of XRD, SEM and ESR. *2nd International Symposium on Advanced Magnetic Materials and Applications (Isamma 2010)* **266**.

Sollner, C., Burghammer, M., Busch-Nentwich, E., Berger, J., Schwarz, H., Riekel, C., and Nicolson, T. (2003) Control of crystal size and lattice formation by starmaker in otolith biomineralization. *Science* **302**(5643), 282-286.

Strunz, H., and Nickel, E.H. (2001) 'Strunz Mineralogical Tables.' (Schweizerbart)

Tohse, H., Takagi, Y., and Nagasawa, H. (2008) Identification of a novel matrix protein contained in a protein aggregate associated with collagen in fish otoliths. *Febs Journal* **275**(10), 2512-2523.

Tomas, J., Geffen, A.J., Millner, R.S., Pineiro, C.G., and Tserpes, G. (2006) Elemental composition of otolith growth marks in three geographically separated populations of European hake (*Merluccius merluccius*). *Marine Biology* **148**(6), 1399-1413.

Toole, C., Markle, D.F., and Harris, P.M. (1993) Relationships between otolith microstructure. microchemistry, and early life history events in Dover sole, *Microstomus pacificus*. *Fisheries Bulletin* **91**(4), 732-753.

Townsend, D.W., Radtke, R.L., Corwin, S., and Libby, D.A. (1992) Strontium-calcium ratios in juvenile Atlantic herring *Clupea Harengus* - otoliths as a function of water temperature. *Journal of Experimental Marine Biology and Ecology* **160**(1), 131-140.

Tzeng, W.-N. (1996) Effects of salinity and ontogenetic movements on strontium:calcium ratios in the otoliths of the Japanese eel, *Anguilla japonica* Temminck and Schlegel. *Journal of Experimental Marine Biology and Ecology* **199**(1), 111-122.

Tzeng, W.N., Shiao, J.C., and Iizuka, Y. (2002) Use of otolith Sr:Ca ratios to study the riverine migratory behaviors of Japanese eel *Anguilla japonica*. *Marine Ecology Progress Series* **245**, 213-221.

Weber, P.K., Hutcheon, I.D., McKeegan, K.D., and Ingram, B.L. (2002) Otolith sulfur isotope method to reconstruct salmon (*Oncorhynchus tshawytscha*) life history *Canadian Journal of Fisheries and Aquatic Sciences* **59**(5), 923-923.

Weiner, S. (1986) Organization of extracellularly mineralized tissues - A comparative study of biological crystal growth. *Crc Critical Reviews in Biochemistry* **20**(4), 365-408.

Weiner, S., and Addadi, L. (1991) Acidic Macromolecules of mineralized tissues - the controllers of formation. *Trends in Biochemical Sciences* **16**(7), 252-256.

Weiner, S., and Addadi, L. (1997) Design strategies in mineralized biological materials. *Journal of Materials Chemistry* **7**(5), 689-702.

Weiner, S., and Dove, P.M. (2003) An overview of biomineralization processes and the problem of the vital effect. In Biomineralization. Vol. 54. (Eds. PM Dove, JJ DeYoreo and S Weiner) pp. 1-29.

Weiner, S., Talmon, Y., and Traub, W. (1983) Electron diffraction of mollusk shell organic matrices and their relationship to the mineral phase. *International Journal of Biological Macromolecules* **5**(6), 325-328.

Weiner, S., and Traub, W. (1980) X-ray diffraction study of the insoluble organic matrix of mollusc shells. *Febs Letters* **111**(2), 311-316.

Wilt, F.H. (1999) Matrix and mineral in the sea urchin larval skeleton. *Journal of Structural Biology* **126**(3), 216-226.

Woodcock, S.H., Grieshaber, C.A., and Walther, B.D. (2013) Dietary transfer of enriched stable isotopes to mark otoliths, fin rays, and scales. *Canadian Journal of Fisheries and Aquatic Sciences* **70**(1), 1-4.

Woodhead, J.D., Hellstrom, J., Hergt, J.M., Greig, A., and Maas, R. (2007) Isotopic and elemental imaging of geological materials by laser ablation inductively coupled plasma-mass spectrometry. *Geostandards and Geoanalytical Research* **31**(4), 331-343.

Wray, J.L., and Daniels, F. (1957) Precipitation of Calcite and Aragonite. *Journal of the American Chemical Society* **79**(9), 2031-2034.

Yoshimura, T., Tamenori, Y., Suzuki, A., Nakashima, R., Iwasaki, N., Hasegawa, H., and Kawahata, H. (2013) Element profile and chemical environment of sulfur in a giant clam shell: Insights from mu-XRF and X-ray absorption near-edge structure. *Chemical Geology* **352**, 170-175.

Zhang, F., Cai, W., Sun, Z., and Zhang, J. (2008) Regular variations in organic matrix composition of small yellow croaker (Pseudociaena polyactis) otoliths: an in situ Raman microspectroscopy and mapping study. *Analytical and Bioanalytical Chemistry* **390**(2), 777-782.

Zhuo, L., Yonghua, G., and Qingling, F. (2009) Hierarchical structure of the otolith of adult wild carp. *Materials Science & Engineering: C (Materials for Biological Applications)* **29**(3), 919-924.

Zimmerman, C.E., and Nielsen, R.L. (2003) Effect of analytical conditions in wavelength dispersive electron microprobe analysis on the measurement of strontium-to-calcium (Sr/Ca) ratios in otoliths of anadromous salmonids. *Fishery Bulletin* **101**(3), 712-718.

Appendix A

A. McFadden, B. Wade, C. Izzo, B.G. Gillanders, C.E. Lenehan, A. Pring, 2015, Quantitative electron microprobe mapping of otoliths suggests elemental incorporation is affected by organic matrices: implications for the interpretation of otolith chemistry, *Marine and Freshwater Research,* 2015, Online version, Vol 66, pp 1-10.

SPECIAL ISSUE

CSIRO PUBLISHING

Marine and Freshwater Research, 2016, 67, 889–898
http://dx.doi.org/10.1071/MF15074

Quantitative electron microprobe mapping of otoliths suggests elemental incorporation is affected by organic matrices: implications for the interpretation of otolith chemistry

A. McFadden[A,B,E], *B. Wade*[B], *C. Izzo*[C], *B. M. Gillanders*[C], *C. E. Lenehan*[D] *and A. Pring*[D]

[A]Department of Chemistry, School of Physical Sciences, The University of Adelaide, North Terrace, Adelaide, SA 5005, Australia.
[B]Adelaide Microscopy, The University of Adelaide, Frome Road, Adelaide, SA, 5005, Australia.
[C]Southern Seas Ecology Laboratories, School of Biological Sciences, The University of Adelaide, North Terrace, Adelaide, SA 5005, Australia.
[D]School of Chemical and Physical Sciences, Flinders University, Bedford Park, SA, 5042, Australia.
[E]Corresponding author. Email: aoife.mcfadden@adelaide.edu.au

Abstract. In an effort to understand the mechanism of otolith elemental incorporation, the distribution of strontium (Sr) and sulfur (S) in otoliths of *Platycephalus bassensis* was investigated in conjunction with otolith growth patterns. Optimisation of electron probe microanalysis (EPMA) quantitative mapping achieved both high spatial resolution (<3 μm) and two-dimensional visualisation of the fine scale Sr and S distributions in otoliths of *P. bassensis* with minimal damage. Electron backscatter diffraction (EBSD) mapping confirmed that grain growth is aligned with the otolith *c*-axis, with grain orientation independent of both otolith elemental composition and growth patterns. Results showed a linear correlation between Sr and S distribution ($R^2 = 0.86$), and a clear association with the otolith growth patterns determined by scanning electron microscopy. Further examination by laser ablation–inductively coupled plasma–mass spectrometry (LA-ICP-MS) showed that incorporation of Mg and Ba appeared independent of both S distribution and the growth patterns. The results suggest that element incorporation into the otolith is linked to the organic composition in the endolymph during mineralisation, and the organic matrices may assist, in part, the uptake of Sr. Thus, these findings may have significant implications for the interpretation of otolith Sr chemistry.

Additional keywords: biomineralisation, electron backscatter diffraction, electron probe microanalysis, fish.

Received 25 February 2015, accepted 28 September 2015, published online 27 November 2015

Introduction

Otoliths are calcium carbonate structures primarily composed of calcium carbonate and organic matrices (<10%) that are involved in the maintenance of balance and hearing in the inner ear of teleost fish. The predictable growth properties of otoliths and permanent uptake of trace elements from the environment is advantageous for a variety of ecological applications, including age determination, stock identification, migration pathway reconstruction and elucidation of environmental histories (Campana 1999; Elsdon *et al.* 2008). Otolith growth and composition are dependent on environmental factors, such as water composition, temperature and salinity, as well as biological factors including genetics, ontogeny, diet and elemental fractionation through biological transport (Barnes and Gillanders 2013; Reis-Santos *et al.* 2013; Woodcock *et al.* 2013).

Biomineralisation is highly regulated by organic macromolecules, which are usually negatively charged proteins containing carboxylate, sulfate and phosphate functional groups (Addadi *et al.* 1987; Mann 1988). These groups are thought to bind Ca^{2+} ions, and could be involved in the control of crystal nucleation by lowering the energy of formation between the crystal and the organic substrate (Weiner 1986; De Yoreo and Vekilov 2003). Sulfur uptake in otoliths is well documented in the study of nutrient flows, migratory patterns and hypoxia (Weber *et al.* 2002; Limburg *et al.* 2015), but the role of sulfated macromolecules in biomineralisation is not well understood. In otoliths, it is thought that sulfate groups primarily occur in a class of proteins called proteoglycans (Addadi *et al.* 1987; Albeck *et al.* 1996). Evidence for the involvement of proteoglycans in biomineralisation is abundant across many biomineral

types, including mollusc shells (Simkiss 1965), sea urchin spines (Wilt 1999), eggshells (Arias *et al.* 1992) and fish otoliths (Borelli *et al.* 2001). Inorganic experiments demonstrate the ability of various proteoglycans to stabilise nucleation and influence crystal size and orientation (Addadi and Weiner 1985; Addadi *et al.* 1987; Arias *et al.* 2004). To extract valuable information from the chemistry of otoliths, it is necessary to understand the mechanism of elemental uptake during organic-mediated biomineralisation (Campana 1999; Kalish 1989).

Elemental incorporation in biominerals is not well understood and, although organic matrices determine the physical properties of biominerals and provide a template for formation (Lowenstam and Weiner 1989; Weiner and Dove 2003; Addadi *et al.* 2006), organic matrices may exhibit affinities for minor and trace elements and preferentially facilitate or inhibit uptake. Based on shell microstructure and elemental composition, recent bivalve shell studies have suggested the possibility that Sr is not under environmental control (Foster *et al.* 2009; Poulain *et al.* 2015) but rather that Sr fractionation is mediated by sulfate-rich organic macromolecules at the site of calcification (Schöne *et al.* 2013; Shirai *et al.* 2014). However, aragonitic shells are considerably more enriched in trace elements than otoliths, so the mechanism of incorporation may differ between the two biominerals (Schöne *et al.* 2013; Shirai *et al.* 2014). Otoliths undergo greater biological fractionation of elements on uptake than shells (Campana 1999), although the trace element compositions of both biominerals are predicted to reflect the environment, suggesting a related, although perhaps not identical mechanism. As such, studies of eel otoliths have indicated that excess glycosaminoglycans (GAGs), a component of proteoglycans, released during larval eel metamorphosis may affect Sr fractionation (Otake 1994; Tzeng 1996). Both studies noted changes in the Sr : Ca ratios during metamorphosis that could not be accounted for by the surrounding ambient environmental conditions (Otake 1994; Tzeng 1996). Distribution of Sr within the otolith has also been noted to be affected by the formation of the seasonal translucent and opaque zones (Toole *et al.* 1993; Tomás *et al.* 2006). Despite these studies, to our knowledge the role organic matrices play in the fractionation of minor and trace elements in otoliths has not been evaluated.

Elemental quantification within microstructural features (1–5 μm) of otoliths is limited by: (1) the spatial resolution of the commonly used techniques; (2) the sensitivity of the otolith structure to damage during analysis; and (3) the sensitivity of available techniques to the elements of interest. Electron microprobe analysis (EPMA) offers a significant improvement in spatial resolution compared with laser ablation–inductively coupled plasma–mass spectrometry (LA-ICP-MS) and is a well-established technique for the evaluation of major and minor elements in otoliths (Gunn *et al.* 1992; Zimmerman and Nielsen 2003). Herein we report an optimised EPMA method using mean atomic number (MAN) background collection for the two-dimensional visualisation of minor and trace elemental composition at high resolution (<3 μm).

We hypothesised that otolith trace elements are fractionated during mineralisation in the endolymph and suggest that understanding this fractionation may reduce the assumptions inherent in interpretation of otolith chemistry. The aim of the present study was to optimise quantitative EPMA mapping to investigate the relationship between otolith composition and growth patterns at a fine scale (<3 μm) with a view to evaluating the effect of the organic matrix on elemental fractionation in otolith biomineralisation to improve future interpretations of otolith chemistry in relation to ecological issues.

Materials and methods

Sample preparation

Sagittal otoliths were obtained from specimens of juvenile sand flathead (*Platycephalus bassensis*, Platycephalidae) a demersal coastal marine species collected from Investigator Strait, South Australia. Upon removal, otoliths were rinsed in ultrapure water to remove any adhering tissue, air dried in a laminar fume hood and stored in microcentrifuge tubes for later examination. Otoliths were subsequently embedded in two part epoxy resin and sectioned through the core to expose the growth increments using a Buehler ISOMET low-speed saw (Lake Bluff, IL, USA). Sectioned otoliths were polished on a Struers TegraPol mechanical polisher (Cleveland, OH, USA), with a graded series of lapping cloths starting with 9 μm, 3 μm and finishing on 0.04 μm colloidal silica. Between each polish, samples were cleaned ultrasonically and rinsed thoroughly in ultrapure water. Prior to scanning electron microscopy (SEM) and EPMA, the polished sections were carbon coated to avoid sample charging during analysis.

SEM and image analysis

SEM was used to visualise the growth patterns and grain microstructure of the otoliths, primarily by backscatter electron imaging (BSE). All images were acquired on an FEI (Eindhoven, Netherlands) Quanta 450 Field Emission Gun SEM operated at 20 kV. High-magnification images were subsequently stitched together in Microsoft (Redmond, WA, USA) ICE. These images were used to relate the otolith growth patterns and grain microstructure to the elemental distribution maps. No etching of the surface was used before imaging to avoid removing minor and trace elements. Of the samples imaged, four otoliths (FH275, FH276, FH277 and FH278) were selected for quantitative mapping by EPMA.

Image analysis, undertaken in ImageJ (National Institutes of Health (NIH), Bethesda, MD, USA) and Avizo Fire 8.1 (FEI), allowed for the determination of grain size across the otolith sections. Grain size was determined through segmentation of the SEM images by thresholding and the application of an adjustable watershed that segments grains based on the Euclidean distance map method (Vincent and Soille 1991). All images were analysed in both ImageJ and Avizo Fire to ensure reproducible results.

Electron backscatter diffraction

Electron backscatter diffraction (EBSD) was used to determine the grain orientation across the otolith sections. EBSD patterns were acquired on a Phillips (Eindhoven) XL30 FEG SEM equipped with an Oxford Instruments Channel 5 Nordlys (Abingdon, UK) EBSD detector. Operating conditions included an accelerating voltage of 15 kV for EBSD mapping at a tilt angle of 70° and a working distance of 20 mm.

Table 1. Summary of electron probe microanalysis spot analysis conditions, including the elements analysed, peak and background positions, count times, standards and elemental overlap corrections for spot analyses
Kα and Lα are X-ray lines, and Kα1 II is a second order X-ray line

Element/ line	Diffracting crystal	Peak count time (s)	Background type/fit	Background points (low/high)	Background count time (low/high) (s)	Standard	Overlapping line/order	Overlap standard
Ca/Kα	LPET	30	Multipoint/linear	3/3	15/15	Astimex Calcite	–	–
Sr/Lα	LTAP	90	Multipoint/linear	1/2	60/30	Astimex Celestite	Ca Ka1 II	Astimex Calcite
Sr/Lα	TAP	90	Multipoint/linear	1/2	60/30	Astimex Celestite	Ca Ka1 II	Astimex Calcite
S/Kα	LPET	45	Multipoint/linear	3/3	30/30	Astimex Anydrite	–	–
S/Kα	LPET	45	Multipoint/linear	3/3	30/30	Astimex Anydrite	–	–

Electron probe microanalysis

EPMA quantitative maps were acquired on a CAMECA (Paris, France) SXFive microprobe. The instrument was equipped with five wavelength dispersive spectrometers (WDS), four of which have large diffracting crystals. Data were acquired and processed in Probe for EPMA software (Eugene, OR, USA). Analytical conditions for spot analyses consisted of an accelerating voltage of 15 kV and a beam current of 20 nA, using beam diameters ranging between 2 and 20 μm. Elements analysed, peak and background positions, count times, standards and elemental overlap corrections for spot analyses are summarised in Table 1. Quantitative elemental maps were collected with a focussed beam of 15 kV, 100 nA, with pixel size of 1 μm and a dwell time of 100 ms. Oxygen and carbon weight percentage content (wt%) were calculated by stoichiometry.

To improve the signal to noise ratio and detection limits of the analysis of sulfur (S), WDS signal aggregation was used with two LPET diffracting crystals. Elemental S maps of the four otolith samples were processed using each LPET spectrometer individually and also via aggregating the counts into a single file. The subsequent detection limits for the two individual spectrometers and the aggregated data were determined for S. The detection limits, expressed as parts per million (equivalent to milligrams per kilogram), for Spectrometer A, Spectrometer B and the aggregated signal were 900, 1200 and 300 ppm respectively, demonstrating the superior detection limit possible with count aggregation.

MAN backgrounds were used for quantitative mapping to reduce damage to the beam-sensitive otoliths. Maps were processed in CalcImage (Probe Software, Eugene, OR, USA) and visualised in Surfer (Golden Software, Golden, CO, USA). The detection limits for Ca, Sr and S in EPMA maps were calculated to be 500, 600 and 300 ppm respectively, calculated to assume detection at threefold the background variance. The limits of quantification for Ca, Sr and S were subsequently calculated to be 1700, 1800 and 900 ppm respectively, calculated to assume quantification at 10-fold the background variance. The effective spatial resolution of the electron beam, taking into account accelerating voltage, beam current and sample matrix, was ~2 μm in diameter, which is adequate to resolve the L and D zones on the antisulcal side of the otoliths; however, the sulcal L and D zones are finer than the effective spatial resolution and as a result are averaged.

Laser ablation inductively coupled plasma mass spectrometry

LA-ICP-MS elemental analyses were performed on an Agilent 7700cx quadrupole ICP-MS (Agilent Technologies, Melbourne, Vic., Australia) coupled to an ASI Resonetics (M-50 Excimer Laser equipped with a Laurin Technic Cell (ASI, Canberra, ACT, Australia). National Institute of Standards and Technology (NIST) 612 standard reference material was used as the external standard, with the US Geological Survey calcium carbonate MACS-3 measured as a secondary standard. Spot analyses were undertaken adjacent to EPMA analyses at a pulse rate of 5 Hz, laser fluence of ~3.5 mJ μm^{-2} and spot diameters of 17–24 μm. All data were processed in Glitter (GEMOC, Macquarie University, Sydney, NSW, Australia) and elemental concentrations were calculated by using the ^{43}Ca signal within each sample as an internal standard, because Ca was previously quantified independently by EPMA. Elemental maps were collected using a pulse rate of 10 Hz, laser fluence of ~3.5 mJ μm^{-2}, 14-μm spot diameter and a scan speed of 14 μm s^{-1}. Isotope dwell times were as follows: ^{43}Ca, 5 ms; ^{88}Sr, 50 ms; ^{24}Mg, 20 ms; ^{138}Ba, 50 ms. All data were processed and output as elemental maps using the program Iolite (Melbourne University, Melbourne, Vic.) developed by the Melbourne Isotope Group (Woodhead *et al.* 2007). The detection limits for Sr, Mg and Ba were calculated to be 59, 0.75 and 0.15 ppm respectively, calculated to assume detection at threefold the background variance. The limits of quantification for Sr, Mg and Ba were calculated to be 199, 2.5 and 0.5 ppm respectively, calculated to assume quantification at 10-fold the background variance. The effective spatial resolution of the LA-ICP-MS maps is 14 μm in the *y* direction and ~4 μm in the *x* direction. The spatial resolution in the *y* direction is fixed by the spot diameter, whereas the spatial resolution in the *x* direction is dependent on the spot diameter, scan speed and analysis time. Therefore, the LA-ICP-MS maps are only able to resolve the seasonal growth of otoliths.

Results

Effect of MAN backgrounds

Repeated spot measurements at beam diameters of 2, 5, 7, 10 and 20 μm were collected on otolith material without moving the sample in order to determine the degradation of the calcium

carbonate over time (Fig. 1) At small beam diameters (high beam power density) there was a significant increase in the apparent measured Ca wt% with repeated measures. Thus, larger beam diameters are required to minimise damage to the otolith during repeated measures.

The beam-sensitive nature of otoliths prevents the collection of a second pass off-peak background acquisition for quantitative mapping and, as a result, MAN background fits were assessed as an alternative for quantitative mapping of otoliths. A comparison of the accuracy and precision of elemental maps created using off-peak backgrounds *v.* those using MAN fit backgrounds was undertaken using a natural aragonite crystal from the Tazouta Mine, Sefrou Morocco (voucher number G34206; South Australian Museum, Adelaide, SA, Australia) as a proxy for the otolith. The absolute numbers and errors were then compared with those of the spot analysis on the aragonite. Aragonite was chosen because it is an ideal $CaCO_3$ mineral that is much less sensitive to beam damage than otoliths, removing this as a variable in the comparison. The bulk concentrations of Ca, Sr and S for aragonite (taken as an average of the concentrations from each pixel within a 300 × 300-μm map) determined by both off-peak and MAN background methods are given in Table 2. Both methods gave virtually identical results; however, the MAN approach required only one irradiation rather than the two used by off-peak background measurements, thus significantly reducing the likelihood of damage to otoliths. The levels of Ca and Sr detected within the aragonite using both methods are typical of those of otoliths, and both are detectable at errors of <5%. Absolute values are also comparable to those determined by more accurate spot analyses (Table 2). In aragonite, S is present at lower levels (~100 ppm) than is expected from the otoliths (~500 ppm) and so errors are expected to be marginally improved for real otolith samples.

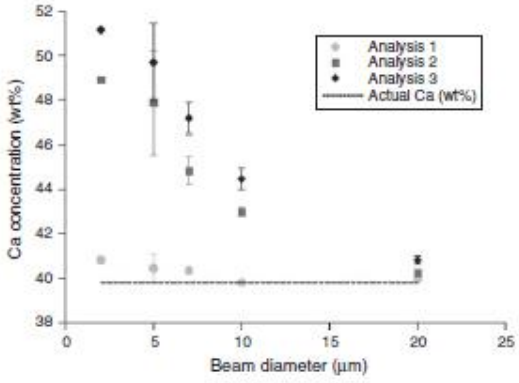

Fig. 1. Apparent Ca weight percentage content (wt%) collected by an electron microprobe analyser (EPMA) on otoliths at 15 kV and 20 nA plotted against beam diameter. The effect of beam damage with repeated measurements is significant at small beam diameters and decreases with increasing beam diameter, stabilising at the actual Ca wt% with a 20-μm beam. Data are the mean ± 95% confidence interval.

Otolith growth patterns and microstructure

Sectioned *P. bassensis* otoliths exhibit the typical alternating paired opaque D-zone bands (areas rich in organic material) and translucent L-zone bands (areas rich in calcium carbonate; for a more detailed definition, see Jolivet *et al.* 2008). D-Zones were clearly visible on the antisulcal side of otoliths, ranging in width from 1 to 15 μm, although the thinner daily growth bands on the sulcal side, with widths ≤1 μm, were not always distinct. BSE imaging revealed the presence of D-zone bands throughout the aragonite grains (Fig. 2). Acicular microstructure (crystal fabrics) dominates the otolith, with growth occurring outwards from the core. The grain size increases from the core, where individual grains are small (<0.5 μm^2) and bordering on indistinct because of a high organic content, to large grains (>100 μm^2) at the outer growth surface.

An exception to the general trend of grain size increase from the core to the outer surface was observed when the sulcal and antisulcal sides of the otolith were compared. Grain size showed a greater increase towards the sulcus. On the sulcal side, where the bulk of otolith growth occurs, the D-zone bands were thinner and the L-zone bands were more defined. Towards the antisulcus, grain size and L-zone width were compressed, whereas the D-zones were broader, possibly due to a lower degree of calcification away from the sensory epithelium.

EBSD maps indicated that the aragonite grain growth is aligned with the *c*-axis (Fig. 3). Grain orientation was independent of growth patterns and elemental composition.

Otolith elemental distribution

Strontium and S were distributed heterogeneously across the four otolith samples analysed, each with the highest concentrations at the D-zones compared with the intervening L-zones (Fig. 4). The mean (±95% confidence interval (CI)) Sr

Table 2. Aragonite mineral maps of bulk composition, comparing the electron probe microanalysis traditional off-peak background method with the mean atomic number background (MAN) method as well as spot analyses results

Data are the mean ±95% confidence interval. Bulk concentrations for the maps were calculated by averaging every pixel in a 300 × 300-μm map. Spot analyses of bulk concentrations are the average of 20 individual measurements, collected at a beam diameter of 20 μm

	Ca (wt%)	Sr (ppm)	S (ppm)	Total (wt%)
Off peak background	40.92 ± 0.63	2000 ± 600	100 ± 100	101.06 ± 0.69
MAN fit background	40.93 ± 0.63	2000 ± 500	100 ± 200	101.13 ± 0.69
Spot analyses	40.25 ± 0.11	2030 ± 60	60 ± 7	100.39 ± 0.12

concentration across the entire otolith map for all four samples (FH275, FH276, FH277 and FH278) was 1720 ± 280 ppm, with the highest mean Sr concentration being 3400 ± 300 ppm. The mean (±95% CI) S concentration across the entire otolith map for all four samples was 550 ± 50 ppm, with the highest mean concentration being 1000 ± 75 ppm. Concentrations of Sr and S were linearly correlated in all four samples. Plotting the correlation for sample FH278 gave an R^2 of 0.86 (Fig. 5).

The distribution of Sr and S in *P. bassensis* otoliths showed a correlation with the D-zones (Fig. 4). The growth bands on the antisulcal side were well resolved by EPMA mapping, but the spatial resolution of the technique did not allow for adequate resolution of the much finer growth bands on the sulcal side. Quantitative EPMA maps revealed that Sr concentrations were, on average, 40% higher in the D-zones than the adjacent L-zones, whereas concentrations of S in the L-zones fell below the detection limit. The concentration of Sr in each D-zone varied, whereas S concentrations remained consistent across all D-zones (Fig. 4). Although the Sr concentration in the D-zones was above the limits of quantification, the concentration of S in the bands was just on the limit of quantification.

Because they fell close to the limit of quantification obtained from mapping, Sr concentrations were also evaluated by LA-ICP-MS and EPMA spot analyses. The mean (±95% CI) Sr concentration determined by LA-ICP-MS in the four samples using a 17-μm spot diameter was 2230 ± 250 ppm. EPMA spot analyses with a 20-μm beam diameter yielded a mean (±95% CI) Sr concentration in the four samples of 2020 ± 200 ppm (Table 3), compared with a mean (±95% CI) Sr concentration determined by EPMA mapping with a 1-μm beam diameter of 1720 ± 280 ppm.

LA-ICP-MS maps of the otolith seasonal translucent and opaque banding revealed that the distribution of Mg and Ba did not exhibit the same correlation with otolith growth patterns, or S distribution as seen for Sr (Fig. 6). The mean (±95% CI) Mg and Ba concentrations in the four samples were 9.1 ± 1.1 and 1.3 ± 0.19 ppm respectively. The Mg distribution was largely inverse to that of Sr, with increased concentrations in the otolith core, and in diffuse bands where Sr levels were the lowest (Fig. 6). The distribution of Ba showed some concentrated bands in common with Sr, although the thin bands of high concentration were inadequately resolved and could not be linked to growth pattern changes (Fig. 6).

Discussion

Optimisation of EPMA mapping

EPMA mapping was optimised for quantification of Sr and S to take advantage of the high spatial resolution (<3 μm) provided by the technique. One of the major limitations of quantitative mapping by EPMA is the damage caused by the electron beam to sensitive materials such as otoliths. This damage is due to the decomposition of the aragonite structure and subsequent loss of CO_2 under the beam and is particularly problematic for repeated measurements (Gunn *et al.* 1992; Zimmerman and Nielsen 2003). However, as beam diameter increased, beam power density was reduced because of beam spread across a larger area, and consequently CO_2 loss decreased. Otolith analysis should use a beam

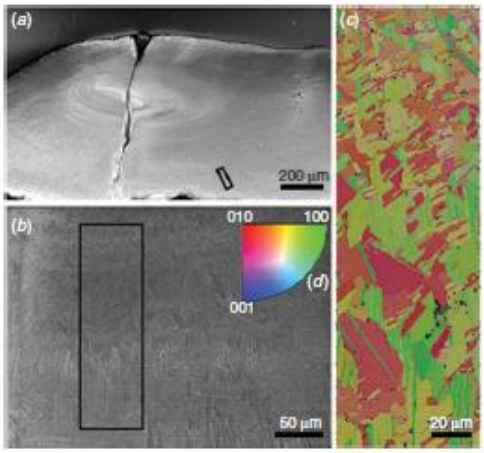

Fig. 3. (*a*) Low-magnification secondary electron scanning electron microscope (SEM) image of sample FH278, sectioned through the otolith core, with the location of the electron backscatter diffraction (EBSD) map indicated near the sulcus. (*b*) High-magnification secondary electron SEM image showing the otolith grain structure and the location of the EBSD map. (*c*) Corresponding EBSD map of FH278 where colour indicates grain orientation, as given by (*d*). The absence of blue in the EBSD map demonstrates that the aragonite *c*-axis (001) remains aligned perpendicular to the sample surface across the entire map.

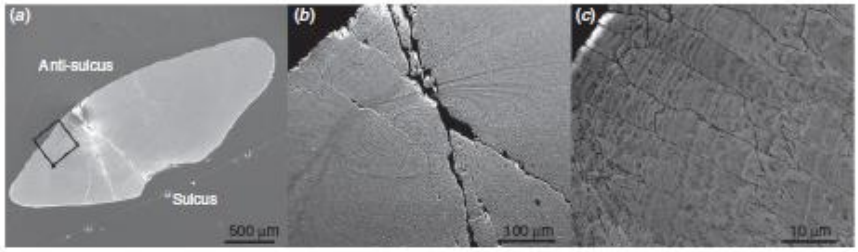

Fig. 2. Scanning electron microscope images of the core of *Platycephalus bassensis* otoliths, showing (*a*) the grain structure and (*b*, *c*) the growth patterns present throughout the aragonite grains as darker bands. The box in (*a*) indicates the area mapped by electron probe microanalysis (EPMA) for Ca, Sr and S concentrations.

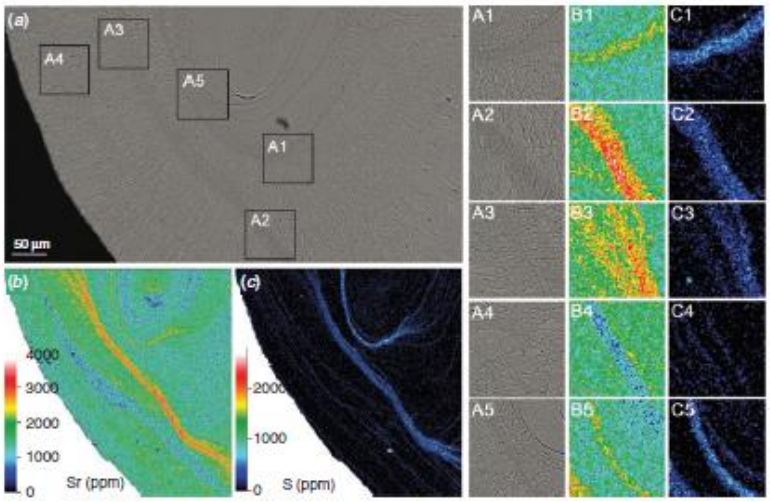

Fig. 4. (*a*) Growth patterns of the core of sample FH278, typical for *Platycephalus bassensis*. Compared with the L-zone bands, the D-zone bands are characteristically darker in the scanning electron microscope backscatter electron imaging (BSE) images. (*b*, *c*) Electron probe microanalysis (EPMA) elemental maps showing the distribution of Sr (*b*) and S (*c*) across sample FH278, with concentration variations illustrated by the colour scale shown at the bottom left of each map. Higher-magnification images of the otolith growth patterns (*A1–A5*) and the elemental maps for Sr (*B1–B5*) Sr and S (*C1–C5*) highlight the relationship between Sr, S and the growth patterns.

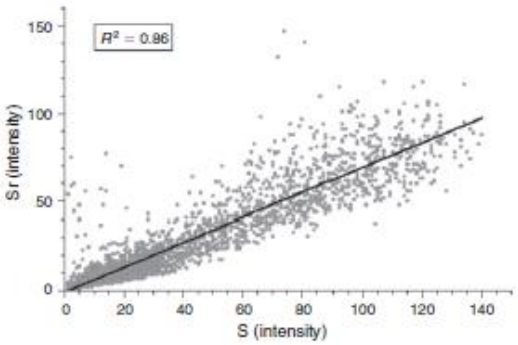

Fig. 5. Correlation of Sr and S in sample FH278, plotted from electron probe microanalysis (EPMA) intensity maps, excluding all points below the EPMA detection limit.

power density of <3 µW µm^{-2}, as noted by Gunn *et al.* (1992), which we found corresponded to a beam diameter of 20 µm. We observed significant changes in elemental quantification with repeated measurements, suggesting that accurate quantitative analyses require a reduction in beam time and the elimination of repeated measurements (but see Zimmerman and Nielsen 2003, who found contrasting results). To circumvent the problem of damage at small beam diameters and the need for repeated measures during quantitative mapping, MAN backgrounds were assessed as an alternative to traditional off-peak background measurements to reduce beam time on the sample.

Table 3. Comparison of laser ablation inductively coupled plasma mass spectrometry (LA-ICP-MS) and electron probe microanalysis (EPMA) spot analysis, giving the mean (±s.e.m.) Sr concentration for each sample

LA-ICP-MS measurements used a 17-µm spot diameter, whereas EPMA used a 20-µm spot diameter. The analyses are compared and the percentage deviation between the techniques is given for each sample

Sample	Sr (ppm)		Percentage deviation
	LA-ICP-MS	EPMA	
FH275	2568.3 ± 22.4	2257.4 ± 37.5	12.10
FH276	2393.3 ± 22.0	2094.7 ± 33.2	12.48
FH277	2007.5 ± 16.8	1875.3 ± 72.8	6.58
FH278	1989.0 ± 17.8	1834.9 ± 60.8	7.74

Traditional off-peak background collection requires two sweeps of the electron beam across the sample, which is unacceptable for elemental quantification of otoliths. Unlike off-peak backgrounds, MAN backgrounds are calculated from the dependence of the X-ray background continuum on MAN. By measuring and curve fitting the background X-ray intensities at the analytical peak in standards that do not contain any of the analyte or interfering elements, the acquisition time and the effect of beam damage is significantly reduced (Donovan and Tingle 1996).

Quantitative elemental mapping at spatial resolutions close to the size of the otolith growth features allows for a better understanding of the relationship between the growth pattern

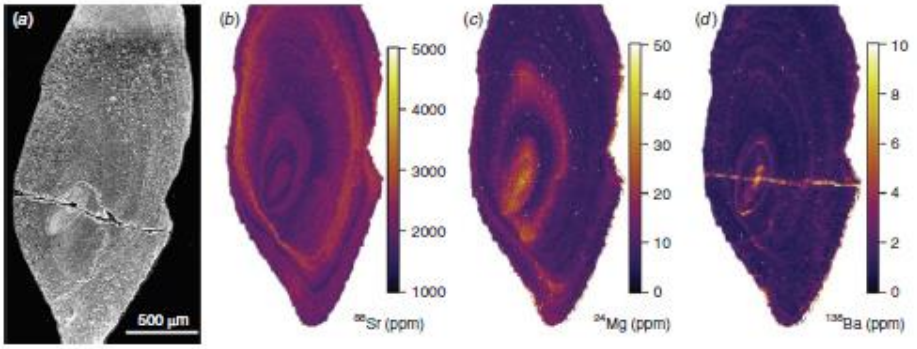

Fig. 6. (*a*) Scanning electron microscope image of sample FH278 alongside (*b–d*) laser ablation inductively coupled plasma mass spectrometry elemental maps giving the distribution of Sr (*b*), Mg (*c*) and Ba (*d*) across the sample, with concentration variations illustrated by the colour scale shown to the right of each map.

and composition. Coarser sampling by LA-ICP-MS and EPMA spot analyses demonstrated the effect of averaging across the growth patterns, whereby the extreme values can be under- or overestimated because of sampling at resolutions larger than the growth features. The effect of signal averaging at coarse spatial resolution has been investigated in mollusc shells, where there was a pronounced reduction in peak height of the highest concentrations across the growth lines (Shirai *et al.* 2014). The effect of averaging was largely overcome in the present study by EPMA mapping because the features of interest (i.e. the D and L zones) were larger than or equal in size to the beam diameter. Averaging is particularly problematic when relating growth patterns to composition in otoliths and should always be considered with care in the interpretation of chronological profiles.

Otolith composition and structure

The association between the distribution of Sr and S, and the otolith growth patterns, indicates that the incorporation of Sr is affected by the biomineralisation process in the otoliths of *P. bassensis*. The role of biological processes in trace element partitioning has been reported previously (Kalish 1989; Campana 1999) and the effects of the elemental pathways and barriers between the water and the otolith have been summarised by Campana (1999). Although the effects of partitioning on physiologically important elements such as Na, P, K and Cl are significant and unpredictable (Campana 1999), the effects on many trace elements are more subtle (Kalish 1989) and are often considered negligible when concentration closely reflects the elemental composition of the water. Based on observations of the present study and the assumption that the changing growth pattern and S distribution reflect the organic composition at the site of mineralisation, we suggest that the organic matrices in the endolymph partially facilitate the uptake of Sr and affect overall otolith composition. Recent reports from mollusc shell studies support this interpretation, because the Sr : Ca and S : Ca ratios exhibit a distinct relationship with the shell microstructure (Foster *et al.* 2009; Schöne *et al.* 2013; Shirai *et al.* 2014).

Role of the organic matrix

Based on the correlation of S with the D-zones, S is assumed to be incorporated in the otolith as a component of the organic matrix, not as inorganic sulfate. This assumption is supported by studies of aragonitic mollusc shells, in which S primarily exists as sulfate within polysaccharides and proteoglycans, whereas a smaller fraction is included as amino acids (Cuif *et al.* 2003; Dauphin *et al.* 2005). Neither $CaSO_4$ nor $SrSO_4$ have been reported in otoliths, but some mollusc shell studies have reported the presence of inorganic sulfate (Siriprom *et al.* 2011; Yoshimura *et al.* 2013). Although not undertaken on otoliths, chemical speciation studies on a variety of biominerals, including mollusc shells and corals, indicate that S exists primarily as a component of the organic matrix (Lowenstam and Weiner 1989; Cuif *et al.* 2003). The function of sulfated macromolecules in biominerals has not been established, but it is proposed that organic sulfate contained within the crystal grains plays a role in nucleation, whereas organic sulfate between the grains is responsible for controlling properties such as size and shape (Arias *et al.* 2004; Addadi *et al.* 2006).

The organic macromolecules most likely responsible for the high S concentrations at the growth bands are sulfated proteoglycans, which have been observed in the endolymph and extracted from otoliths (Payan *et al.* 1997; Borelli *et al.* 2001; Arias *et al.* 2004). The role of proteoglycans in otolith biomineralisation has not been established, but their anionic properties have led to the suggestion of a role in concentrating Ca^{2+} ions at the endolymph–crystal interface (Borelli *et al.* 2001). Borelli *et al.* (2001) observed an increasing proximodistal gradient of proteoglycans in the endolymphs of *Oncorhychus mykiss* and *Psetta maxima*, whereas proteins, collagens and amino acids exhibited a decreasing proximodistal gradient. It was suggested that there may be a relationship between the endolymph gradient and the otolith growth axes, notably that the strong growth at the sulcus may be associated with the proximodistally decreasing gradients of proteins and collagens (Borelli *et al.* 2001). Inversely, the increasing proximodistal gradient of proteoglycans may be limiting growth at the antisulcus by binding free cations in the endolymphatic fluid

(Payan *et al.* 2002). At the antisulcal side, where grain size is smaller, the appearance of broad D-zones supports the notion of a growth-inhibiting action of S-rich organic matrices. The growth pattern correlation with Sr would also suggest such organic macromolecules exhibit a high cation-binding affinity, perhaps leading to enhanced Sr incorporation, predominantly at the antisulcus. However, the fine scale microstructure on the sulcal side is not adequately resolved by EPMA mapping to determine whether such observations are exclusive to the antisulcus or are equivalent on the sulcal side at a finer, unresolved scale.

The role of proteoglycans in otoliths has not been established, but if they are indeed the macromolecules observed by proxy through the S distribution, then a role in crystal orientation control can be ruled out. Grain orientation in biominerals is predicted to be constrained by the organic template, an insoluble collagen-like protein present throughout the mineral structure. The independence of grain orientation and elemental composition in the present study suggests that the organic template exerts little or no control over trace element uptake.

Otolith chemistry

Differences in the distribution of Sr, Mg and Ba throughout the otolith may be a result of environmental changes, but may also be explained, in part, by differences in the site occupied by each element in the aragonite structure. High-energy X-ray absorption studies have revealed that Sr is randomly substituted for Ca in the aragonite structure of otoliths (Doubleday *et al.* 2014). Therefore, the relationship between Sr and the S-rich organic matrices is unlikely to be a result of direct binding of the organic matrix to Sr, but rather a result of organic-mediated fractionation during mineralisation. It is predicted that most of the discrimination against Sr incorporation occurs during crystallisation rather than during Sr uptake from the water because of the similarity in the water–otolith and endolymph–otolith partition coefficients (Campana 1999). Using our results, the mean water–otolith partition coefficient (D_{Sr}) is calculated to be 0.19 assuming a mean seawater Sr : Ca ratio of 8.9 mmol mol^{-1}. This is comparable to estimates of other studies and to the calculated endolymph–otolith D_{Sr} of 0.25 (Kalish 1989); however, it is unclear whether the Sr fractionation is related to the presence of S-rich proteoglycans because of the limits of detection and spatial resolution constraints of EPMA mapping. Sr and S were shown to be correlated at the D-zones, where concentrations are the highest, but the S concentrations fell below the detection limits within the L-zones. Current observations point towards the facilitation of Sr uptake by the S-rich organic matrices, but it is unclear whether these observations are exclusive to the D-zones or extend throughout the otolith structure at concentrations below the detection limits of EPMA.

Mg is present in otoliths at concentrations too low to evaluate its bonding mode; however, mollusc shell studies show Mg to be hosted by the organic component as a disordered phase in biogenic aragonite (Foster *et al.* 2008). The high concentration of Mg observed in the otolith core by LA-ICP-MS mapping supports this possibility in otoliths as well, although it also indicates that the organic matrix involved in otolith nucleation and initial growth may not be the S-rich organic matrix observed by proxy in the present study. The S-rich proteoglycans are not known to be involved in the nucleation process, but rather are implicated in the inhibition of crystal growth in specific stereochemical directions (Addadi *et al.* 1987). Mg is more likely to be bound by a component of the organic matrix involved in nucleation, rather than have uptake facilitated as in the case of Sr.

The host site of Ba within otoliths has not been evaluated, although it is predicted to occupy sites analogous to those of Sr (Pingitore 1986; Dietzel *et al.* 2004). Because of the larger ionic radius of Ba (1.47 Å) than Ca (1.18 Å), substitution of Ba for Ca is more limited than that of Sr. Because of the increase in crystal defects with greater Sr uptake (Pingitore 1986), uptake of Ba may be facilitated by Sr in waters with a high Sr : Ca ratio (de Vries *et al.* 2005). However, based on our LA-ICP-MS maps, Ba is not affected by the organic matrix or the Sr concentration, which may be due to a low Sr : Ca ratio for our samples (1–3 mmol mol^{-1}), below that needed to facilitate Ba uptake (>4 mmol mol^{-1}; de Vries *et al.* 2005). Despite this, it cannot be ruled out that a relationship exists at a spatial resolution below that achieved by LA-ICP-MS mapping.

Implications for otolith chemistry interpretation

The correlation of Sr with both S and otolith growth patterns may have implications for the interpretation of otolith chemistry, but there are still ambiguities to be addressed before such implications can be fully understood. The present study highlights that Sr and S are linked in the D-zones, and suggests that S-rich organic matrices play a role in Sr incorporation, possibly by concentrating Sr at the site of mineralisation. However, the detection limits of EPMA limit our understanding of the relationship across the entire otolith. If Sr and S are correlated within the L-zones as well as the D-zones, then it is possible that S-rich organics are responsible for the fractionation of Sr between the endolymph and otolith. In that case, the observed variation in Sr would be directly related to ambient water concentration. However, if the correlation is only present within the organic-rich D-zones, then the observed Sr variation at the bands may be a result of the concentration of the organic matrices in the endolymph, rather than the ambient water concentration. The distinction is one of importance with regard to implications for otolith chemistry interpretations, but a definitive answer currently remains below the spatial resolution and detection limits of the techniques available.

Conclusions

Using MAN background fits and signal aggregation, high-resolution, two-dimensional elemental mapping of otoliths by EPMA revealed a relationship between Sr and S distribution and the otolith growth patterns, providing an insight into the role of biomineralisation in otolith elemental incorporation. Otolith grain orientation was independent of otolith growth patterns and composition, suggesting that the organic template upon which growth is constrained is unlikely to be involved in elemental uptake. Under the assumption that S is present as a component of the organic matrix, we suggest that Sr uptake is mediated by organic macromolecules in the endolymph, with S-rich organic matrix components, such as proteoglycans, likely candidates in the facilitation. Without direct measurement of the organic

matrices, it is not possible to reach definitive conclusions, but recent findings in mollusc shells support the suggestion of an organic-mediated Sr uptake in biogenic systems. Further studies are needed to investigate the extent of the relationship across the otolith at lower detection limits to fully understand the implications of biomineralisation on otolith chemistry interpretations. Further investigations into the organic matrix at a fine scale will also improve our understanding of elemental uptake in biogenic systems, such as otoliths.

Acknowledgements

The authors acknowledge the facilities and the scientific and technical assistance of the Australian Microscopy and Microanalysis Research Facility at Adelaide Microscopy, The University of Adelaide. The support of all the Adelaide Microscopy staff is gratefully acknowledged. B. M. Gillanders was supported by an Australian Research Council Future Fellowship (FT100100767).

References

Addadi, L., and Weiner, S. (1985). Interactions between acidic proteins and crystals – stereochemical requirements in biomineralization. *Proceedings of the National Academy of Sciences of the United States of America* **82**, 4110–4114. doi:10.1073/PNAS.82.12.4110

Addadi, L., Moradian, J., Shay, E., Maroudas, N. G., and Weiner, S. (1987). A chemical model for the cooperation of sulfates and carboxylates in calcite crystal nucleation: relevance to biomineralization. *Proceedings of the National Academy of Sciences of the United States of America* **84**, 2732–2736. doi:10.1073/PNAS.84.9.2732

Addadi, L., Joester, D., Nudelman, F., and Weiner, S. (2006). Mollusk shell formation: a source of new concepts for understanding biomineralization processes. *Chemistry* **12**, 980–987. doi:10.1002/CHEM.200500980

Albeck, S., Weiner, S., and Addadi, L. (1996). Polysaccharides of intracrystalline glycoproteins modulate calcite crystal growth *in vitro*. *Chemistry – a European Journal* **2**, 278–284. doi:10.1002/CHEM.19960020308

Arias, J. L., Carrino, D. A., Fernandez, M. S., Rodriguez, J. P., Dennis, J. E., and Caplan, A. I. (1992). Partial biochemical and immunochemical characterization of avian eggshell extracellular matrices. *Archives of Biochemistry and Biophysics* **298**, 293–302. doi:10.1016/0003-9861(92)90126-H

Arias, J. L., Neira-Carrillo, A., Arias, J. I., Escobar, C., Bodero, M., David, M., and Fernandez, M. S. (2004). Sulfated polymers in biological mineralization: a plausible source for bio-inspired engineering. *Journal of Materials Chemistry* **14**, 2154–2160. doi:10.1039/B401396D

Barnes, T. C., and Gillanders, B. M. (2013). Combined effects of extrinsic and intrinsic factors on otolith chemistry: implications for environmental reconstructions. *Canadian Journal of Fisheries and Aquatic Sciences* **70**, 1159–1166. doi:10.1139/CJFAS-2012-0442

Borelli, G., Mayer-Gostan, N., De Pontual, H., Boeuf, G., and Payan, P. (2001). Biochemical relationships between endolymph and otolith matrix in the trout (*Oncorhynchus mykiss*) and turbot (*Psetta maxima*). *Calcified Tissue International* **69**, 356–364. doi:10.1007/S00223-001-2016-8

Campana, S. E. (1999). Chemistry and composition of fish otoliths: pathways, mechanisms and applications. *Marine Ecology Progress Series* **188**, 263–297. doi:10.3354/MEPS188263

Cuif, J.-P., Dauphin, Y., Doucet, J., Salome, M., and Susini, J. (2003). XANES mapping of organic sulfate in three scleractinian coral skeletons. *Geochimica et Cosmochimica Acta* **67**, 75–83. doi:10.1016/S0016-7037(02)01041-4

Dauphin, Y., Cuif, J.-P., Salomé, M., and Susini, J. (2005). Speciation and distribution of sulfur in a mollusk shell as revealed by *in situ* maps using X-ray absorption near-edge structure (XANES) spectroscopy at the S K-edge. *The American Mineralogist* **90**, 1748–1758. doi:10.2138/AM.2005.1640

de Vries, M. C., Gillanders, B. M., and Elsdon, T. S. (2005). Facilitation of barium uptake into fish otoliths: influence of strontium concentration and salinity. *Geochimica et Cosmochimica Acta* **69**, 4061–4072. doi:10.1016/J.GCA.2005.03.052

De Yoreo, J. J., and Vekilov, P. G. (2003). Principles of crystal nucleation and growth. *Reviews in Mineralogy and Geochemistry* **54**, 57–93. doi:10.2113/0540057

Dietzel, M., Gussone, N., and Eisenhauer, A. (2004). Co-precipitation of Sr^{2+} and Ba^{2+} with aragonite by membrane diffusion of CO_2 between 10 and 50°C. *Chemical Geology* **203**, 139–151. doi:10.1016/J.CHEMGEO.2003.09.008

Donovan, J. J., and Tingle, T. N. (1996). An improved mean atomic number background correction for quantitative microanalysis. *Microscopy and Microanalysis* **2**, 1–7. doi:10.1017/S1431927696210013

Doubleday, Z. A., Harris, H. H., Izzo, C., and Gillanders, B. M. (2014). Strontium randomly substituting for calcium in fish otolith aragonite. *Analytical Chemistry* **86**, 865–869. doi:10.1021/AC4034278

Elsdon, T. S., Wells, B. K., Campana, S. E., Gillanders, B. M., Jones, C. M., Limburg, K. E., Secor, D. H., Thorrold, S. R., and Walther, B. D. (2008). Otolith chemistry to describe movements and life-history parameters of fishes: hypotheses, assumptions, limitations and inferences. In 'Oceanography and Marine Biology: An Annual Review', Vol 46. (Eds R. N. Gibson, R. J. A. Atkinson and J. D. M. Gordon.) pp. 297–330. (CRC Press–Taylor & Francis Group: Boca Raton.)

Foster, L. C., Finch, A. A., Allison, N., Andersson, C., and Clarke, L. J. (2008). Mg in aragonitic bivalve shells: seasonal variations and mode of incorporation in *Arctica islandica*. *Chemical Geology* **254**, 113–119. doi:10.1016/J.CHEMGEO.2008.06.007

Foster, L. C., Allison, N., Finch, A. A., and Andersson, C. (2009). Strontium distribution in the shell of the aragonite bivalve *Arctica islandica*. *Geochemistry Geophysics, Geosystems* **10**, Q03003. doi:10.1029/2007GC001915

Gunn, J. S., Harrowfield, I. R., Proctor, C. H., and Thresher, R. E. (1992). Electron probe microanalysis of fish otoliths: evaluation of techniques for studying age and stock discrimination. *Journal of Experimental Marine Biology and Ecology* **158**, 1–36. doi:10.1016/0022-0981(92)90306-U

Jolivet, A., Bardeau, J.-F., Fablet, R., Paulet, Y.-M., and Pontual, H. (2008). Understanding otolith biomineralization processes: new insights into microscale spatial distribution of organic and mineral fractions from Raman microspectrometry. *Analytical and Bioanalytical Chemistry* **392**, 551–560. doi:10.1007/S00216-008-2273-8

Kalish, J. M. (1989). Otolith microchemistry: validation of the effects of physiology, age and environment on otolith composition. *Journal of Experimental Marine Biology and Ecology* **132**, 151–178. doi:10.1016/0022-0981(89)90126-3

Limburg, K. E., Walther, B. D., Lu, Z., Jackman, G., Mohan, J., Walther, Y., Nissling, A., Weber, P. K., and Schmitt, A. K. (2015). In search of the dead zone: use of otoliths for tracking fish exposure to hypoxia. *Journal of Marine Systems* **141**, 167–178. doi:10.1016/J.JMARSYS.2014.02.014

Lowenstam, H. A., and Weiner, S. (1989) 'On Biomineralization.' (Oxford University Press: New York.)

Mann, S. (1988). Molecular recognition in biomineralization. *Nature* **332**, 119–124. doi:10.1038/332119A0

Otake, T. (1994). Drastic changes in otolith strontium/calcium ratios in leptocephali and glass eels of Japanese eel *Anguilla japonica*. *Marine Ecology Progress Series* **112**, 189–193. doi:10.3354/MEPS112189

Payan, P., Kossmann, H., Watrin, A., Mayer-Gostan, N., and Boeuf, G. (1997). Ionic composition of endolymph in teleosts: origin and importance of endolymph alkalinity. *The Journal of Experimental Biology* **200**, 1905–1912.

Payan, P., Borelli, G., Priouzeau, F., De Pontual, H., Boeuf, G., and Mayer-Gostan, N. (2002). Otolith growth in trout *Oncorhynchus mykiss*: supply of Ca^{2+} and Sr^{2+} to the saccular endolymph. *The Journal of Experimental Biology* **205**, 2687–2695.

Pingitore, N. E. (1986). Modes of coprecipitation of Ba^{2+} and Sr^{2+} with calcite. *ACS Symposium Series* **323**, 574–586. doi:10.1021/BK-1987-0323.CH027

Poulain, C., Gillikin, D. P., Thebault, J., Munaron, J. M., Bohn, M., Robert, R., Paulet, Y.-M., and Lorrain, A. (2015). An evaluation of Mg/Ca, Sr/Ca, and Ba/Ca ratios as environmental proxies in aragonite bivalve shells. *Chemical Geology* **396**, 42–50. doi:10.1016/J.CHEMGEO.2014.12.019

Reis-Santos, P., Tanner, S. E., Elsdon, T. S., Cabral, H. N., and Gillanders, B. M. (2013). Effects of temperature, salinity and water composition on otolith elemental incorporation of *Dicentrarchus labrax*. *Journal of Experimental Marine Biology and Ecology* **446**, 245–252. doi:10.1016/J.JEMBE.2013.05.027

Schöne, B. R., Radermacher, P., Zhang, Z., and Jacob, D. E. (2013). Crystal fabrics and element impurities (Sr/Ca, Mg/Ca, and Ba/Ca) in shells of *Arctica islandica*: implications for paleoclimate reconstructions. *Palaeogeography, Palaeoclimatology, Palaeoecology* **373**, 50–59. doi:10.1016/J.PALAEO.2011.05.013

Shirai, K., Schöne, B. R., Miyaji, T., Radermacher, P., Krause, R. A., Jr, and Tanabe, K. (2014). Assessment of the mechanism of elemental incorporation into bivalve shells (*Arctica islandica*) based on elemental distribution at the microstructural scale. *Geochimica et Cosmochimica Acta* **126**, 307–320. doi:10.1016/J.GCA.2013.10.050

Simkiss, K. (1965). Organic matric of oyster shell. *Comparative Biochemistry and Physiology* **16**, 427–435. doi:10.1016/0010-406X(65)90307-5

Siriprom, W., Kaewkhao, J., Phachana, K., and Limsuwan, P. (2011). Crystal structure and morphology dependence of the phase of mollusc shell: a case study of XRD, SEM and ESR. In '2nd International Symposium on Advanced Magnetic Materials and Applications (ISAMMA 2010)', 12–16 July 2010, Sendai, Japan. (Eds M. Takahashi, H. Saito, S. Yoshimura, K. Takanashi, M. Sahashi, and M. Tsunoda). Vol. 266, paper 012124. (IOP Publishing Ltd: Bristol.)

Tomás, J., Geffen, A. J., Millner, R. S., Pineiro, C. G., and Tserpes, G. (2006). Elemental composition of otolith growth marks in three geographically separated populations of European hake (*Merluccius merluccius*). *Marine Biology* **148**, 1399–1413. doi:10.1007/S00227-005-0171-6

Toole, C., Markle, D. F., and Harris, P. M. (1993). Relationships between otolith microstructure. microchemistry, and early life history events in Dover sole, *Microstomus pacificus*. *Fish Bulletin* **91**, 732–753.

Tzeng, W.-N. (1996). Effects of salinity and ontogenetic movements on strontium: calcium ratios in the otoliths of the Japanese eel, *Anguilla japonica* Temminck and Schlegel. *Journal of Experimental Marine Biology and Ecology* **199**, 111–122. doi:10.1016/0022-0981(95)00185-9

Vincent, L., and Soille, P. (1991). Watersheds in digital spaces: an efficient algorithm based on immersion simulations. *IEEE Transactions on Pattern Analysis and Machine Intelligence* **13**, 583–598. doi:10.1109/34.87344

Weber, P. K., Hutcheon, I. D., McKeegan, K. D., and Ingram, B. L. (2002). Otolith sulfur isotope method to reconstruct salmon (*Oncorhynchus tshawytscha*) life history. *Canadian Journal of Fisheries and Aquatic Sciences* **59**, 923–923. doi:10.1139/F02-901

Weiner, S. (1986). Organization of extracellularly mineralized tissues: a comparative study of biological crystal growth. *CRC Critical Reviews in Biochemistry* **20**, 365–408. doi:10.3109/10409238609081998

Weiner, S., and Dove, P. M. (2003). An overview of biomineralization processes and the problem of the vital effect. In 'Biomineralization', Vol. 54. (Eds P. M. Dove, J. J. DeYoreo and S. Weiner.) pp. 1–29. (Mineralogical Society of America: Washington, DC.)

Wilt, F. H. (1999). Matrix and mineral in the sea urchin larval skeleton. *Journal of Structural Biology* **126**, 216–226. doi:10.1006/JSBI.1999.4105

Woodcock, S. H., Grieshaber, C. A., and Walther, B. D. (2013). Dietary transfer of enriched stable isotopes to mark otoliths, fin rays, and scales. *Canadian Journal of Fisheries and Aquatic Sciences* **70**, 1–4. doi:10.1139/CJFAS-2012-0389

Woodhead, J. D., Hellstrom, J., Hergt, J. M., Greig, A., and Maas, R. (2007). Isotopic and elemental imaging of geological materials by laser ablation inductively coupled plasma–mass spectrometry. *Geostandards and Geoanalytical Research* **31**, 331–343. doi:10.1111/J.1751-908X.2007.00104.X

Yoshimura, T., Tamenori, Y., Suzuki, A., Nakashima, R., Iwasaki, N., Hasegawa, H., and Kawahata, H. (2013). Element profile and chemical environment of sulfur in a giant clam shell: insights from μ-XRF and X-ray absorption near-edge structure. *Chemical Geology* **352**, 170–175. doi:10.1016/J.CHEMGEO.2013.05.035

Zimmerman, C. E., and Nielsen, R. L. (2003). Effect of analytical conditions in wavelength dispersive electron microprobe analysis on the measurement of strontium-to-calcium (Sr/Ca) ratios in otoliths of anadromous salmonids. *Fishery Bulletin* **101**, 712–718.